
# 8th DELTA
## User- meeting

**Dortmund**
**28. November 2012**

Edited by C.Sternemann, R. Wagner,
D. Lützenkirchen-Hecht (2012)

November 2012

Preface

Dear reader, dear colleague,

again a year of successful work at DELTA has almost finished, and the obtained results are compiled in this annual report. A large number of users from different institutions have utilized synchrotron radiation from the DELTA facility for their research activities in physics, chemistry, biology, materials and accelerator science, using the entire spectrum of synchrotron radiation from the infrared to hard X-rays, and the diverse experimental techniques. The „NRW Forschungsschule – Forschung mit Synchrotronstrahlung in den Nano- und Biowissenschaften" became really successful with several finished thesis projects up to now. Furthermore, new beamlines and experimental set-ups have come into operation, especially the initiatives of Prof. Khans group to generate short pulses by coherent harmonic generation are impressive. From the user`s point of view it is also important that BL2 and BL10 became operational in the past year, so that an increasing number of user experiments can be scheduled in the next proposal rounds.

As you may have noticed, this annual report was not compiled by Alex von Bohlen, who has made this effort during the last seven years. Let us explicitly thank Alex for all the work he did and all the time he has spent, not only in compiling the user reports, but also in the excellent organization of the DELTA users meetings over years! And let us also thank Monika Voits-Besli for her work – without her, it would hardly be possible to organize an event like this.

Many thanks to all the staff members of DELTA. They did an excellent job to deliver an intense and stable beam and thus they have contributed in many ways to the success of each individual project, and they are therefore also responsible for the success of the research conducted.

Finally, we have to acknowledge the financial support of DELTA by the different funding agencies, the local government, the TU Dortmund, FZ Jülich and the involved universities, who all supported our activities.

Dirk Lützenkirchen-Hecht, Christian Sternemann, Ralph Wagner

## Contents:

In situ Investigation of structure and electrical performance of poly (3-hexylthiophene) droplets during solidification of thin film OFET Devices
L. Grodd, E. Mikayelyan, U. Pietsch, S. Grigorian

Nanopowders for X-ray cross-correlation analysis
C. Gutt, M. A. Schroer, B. Fischer, M. Paulus

Determination of melting temperatures of strained shape memory natural rubber
B. Heuwers, D. Quitmann, R. Hoeher, F.M. Reinders, S. Tiemeyer, C. Sternemann, M. Tolan, F. Katzenberg, J.C. Tiller

Decarburization in HVOF-sprayed WC-CO and WC-FeCrAl coatings
B. Hussong

Enhancement of field effect mobility due to structural ordering in (Poly3-hexylthiophene) films transistors by dip-coating technique
S. Kamran, U.Pietsch and S.Grigorian

Phase transitions of polymers under confinement in the silicate-based, intercalated polymer nanocomposites
A. Kiersnowski, M. Mezger, M. Gazińska, B. Hou, C. Sternemann, M. Paulus

Temperature treatment of protein layers at the solid-liquid interface in two different environments
I. Kiesel, M. Paulus, J. Nase, S. Tiemeyer, C. Sternemann, M. Tolan

Fast x-ray reflectivities
J. Nase, M. Paulus, C. Sternemann, S. Tiemeyer, F. Wirkert, M. Tolan

The interface between a solid and supercritical $CO_2$
J. Nase, M. Paulus, S. Holz, S. Tiemeyer, F. Wirkert, T. Brenner, M. Tolan

Investigation of Q&P steels
K. Rüster, A. Steffen, M. Paulus, C. Sternemann, M. Tolan, N. Große-Heilmann, C. Kronholz, A. Peters

Structural investigations on ternary and quaternary inter alkali metal acetylides by means of synchrotron powder diffraction / Valence changes in dicarbide solid solutions induced by structural changes
S. Liebig, S. Busch and U. Ruschewitz

In situ XRD of $CO_2$ loaded flexible metal-organic frameworks
A. Schneemann, S. Henke, C. Sternemann, M. Paulus, F. Wieland, R.A. Fischer

Influence of alkyl side chain length and cast temperature on the in-plane stacking of P3AT crystallites and their OFET performance
T.S. Shabi, S. Grigorian, M. Brinkmann, U. Pietsch, N. Koenen, N. Kayunkid, U. Scherf, M. Fakhri, T. Riedl

Influence of Cr fraction on the graphite content in diamond tools
A. Steffen, M. Ferreira, M. Paulus, W. Tillmann, M. Tolan

In situ X-ray diffraction studies of diamond tool binder phase feedstock materials
A. Steffen, M. Ferreira, M. Paulus, K. Rüster, W. Tillmann, M. Tolan

Diamond-metal interactions in vacuum sintered and hot-pressed diamond grinding tools
M. Ferreira, W. Tillmann, S. Thutewohl

Lattice expansion in optically excited InAs/GaAs quantum dots
S. Tiemeyer, M. Bombeck, M. Paulus, C. Sternemann, J. Nase, F.J. Wirkert, M. Bayer, M. Tolan

Forming of intermetallic phases at the interface of steel –aluminium compounds
M. Windmann, A. Röttger, W. Theisen

Structure and ice content of clathrate hydrates
F.J. Wirkert, H. Nelson, C. Sternemann, M. Paulus, K. Mende, J. Möller, J. Nase, R. Böhmer, M. Tolan

In-situ monitoring the phase transitions and formations in Li-air batteries
S. Ganapathy, R. Wagner, D. Lützenkirchen-Hecht, B. Adams, L. Nazar, M. Wagemaker

## Hard X-ray spectroscopy

Structural characterization of characterization of polygermane networks
I. Brinkmann, C. Sternemann, M. Paulus, P. Degen, K. Mende, A. Nyrow, S. Balk, H. Rehage, M. Tolan

EXAFS investigation on the temperature dependent structural properties of gold nanoparticles
K. Blech, U. Simon, D. Lützenkirchen-Hecht, R. Wagner, R. Frahm

Extended X-ray absorption fine structure (EXAFS) investigation of iron incorporation during $Kr^+$ ion beam sputtering on Si(100)
B. Khanbabaee, M. Engler , R. Wagner, D. Lützenkirchen-Hecht, U. Pietsch

XAS analysis of ultrasmall gold nanoparticles
C. Helmbrecht, W. Frank, D. Lützenkirchen-Hecht, R. Wagner, R. Frahm

Local atomic and electronic structure of Ag clusters deposited in a silica aerogel matrix
S. Hoffmann, D. Engemann, S. Duffe, C. Sternemann, Stefan Balk, R. Wagner, H. Hövel

Investigation of polydisperse Ni/Ti nanoparticles using X-ray Standing Waves
M. Brücher, A. von Bohlen, M.Chakif, E.Gurevich, R. Hergenröder

XANES investigation of $TiO_2$-$ZrO_2$ composite materials
S. Pfleiderer, D. Lützenkirchen-Hecht, R. Frahm

5 years of Education with Synchrotron Radiation at DELTA – a short review of past activities and a look into the future
D. Lützenkirchen-Hecht, R. Frahm

# Beamline BL1: Production of micro- and nanopores in polymer foils by deep x-ray lithography

Thorsten Brenner*, Michael Paulus, Metin Tolan
*Fakultät Physik/DELTA, Technische Universität Dortmund, 44227 Dortmund, Germany.*
Andreas Neyer
*Fakultät für Elektrotechnik und Informationstechnik, Arbeitsgebiet Mikrostrukturtechnik (AG MST), Technische Universität Dortmund, 44227 Dortmund, Germany.*

*email: thorsten.brenner@tu-dortmund.de

Beamline BL1 is dedicated to deep x-ray lithography (DXRL). DXRL is a method to produce various microstructures with a height up to several millimeters. Microstructures are applied in optics, micro mechanics, fluidic, or medical devices. It is possible to reach a high aspect ratio of about 100 and a lateral resolution up to 2 µm for microstructures using DXRL [1]. One application of x-ray lithography is the production of micro- and nanopores in polymer foils. These foils can be used for cooling of photovoltaic systems. The higher the temperature of the solar cells (e. g. under solar radiation), the lower is the resulting current. The principle of the proposed cooling is lent by nature: In trees there is a combined way of water transport by capillary forces and transpiration pull. Here, the transpiration pull is caused by evaporation of water at the tree's surfaces (e. g. its leaves). This causes both low pressure in the underlying pores (water transport) and a negative enthalpy of vaporization (cooling effect).

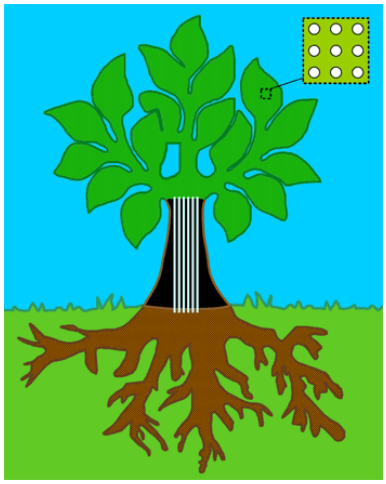

**Figure 1**: Capillary structures and pores at the tree's surfaces are used for water transport.

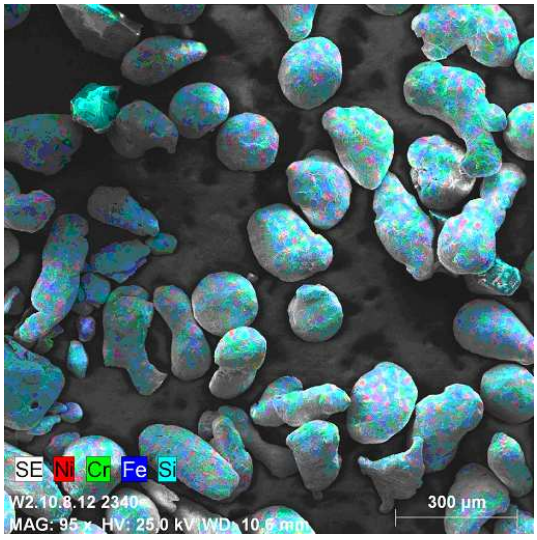


**Figure 2**: SEM image of microparticles used as x-ray absorber to generate pore structures, material analysis included.

For this reason the production of micropores in polymer structures is applied. For a proof of principle experiment the negative resist SU-8 is used. The thickness of resist is 550 µm captured on a silicon wafer with chromium/gold starting layer. Momentary, a commercial x-ray mask has not been available. So, an alternative way has been proven: Metallic microparticles (mixture of iron, nickel, chromium, and silicon, particle size 0.05 to 0.2 mm), which are commercially available (Microbeads AG, Brugg, Switzerland) and used for (sand) blasting application, are mashed up with two-component glue to make a thin homogeneous layer on kapton foil. Three different areas with rising density of coverage have been prepared. This mask has been used for exposure. Post exposure bake has been performed by heating every wafer 10 minutes at 55° C and 35 minutes at 70° C. The chemical development is done by micro resist technology, Berlin, Germany.

The results for two wafers will be discussed as follows: Sample No. 419 and No. 422, latter is exposed with a doubled dose compared to No. 419. The analysis is done by optical microscopy (not shown) and Scanning Electron Microscopy (SEM). The optical microscopy shows cracks in the resist's surface centering the holes. This might indicate too high temperature on the sample due to the exposure process. The SEM images of both samples are shown in figures 3 and 4. First, the sample 419 is discussed: Due

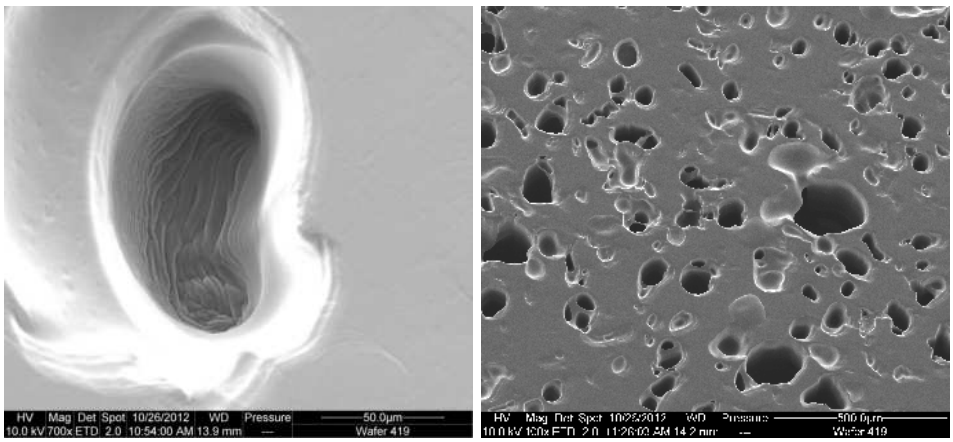

**Figure 3:** SEM images of sample 419.

to the lower dose a majority of holes is not developed completely (figure 3, left). A general observation is the fading edge of the holes. This corresponds to the fact, that the particles possess a round shape. That means, if one compares the radiation way between centre and edge of particles there is a different throughput. Corresponding to the Lambert Beer law $I(d) = I_0 \exp(-\mu(\lambda)d(x))$ (intensity $I$, absorption coefficient $\mu$ as a function of the wavelength $\lambda$, $d$ thickness of sample as a function of the position $x$), there is a different dose deposition depending on the position behind the particle. The high coverage of particles (figure 3, right) leads to a merge of hole structures. This is not the case in the area with the middle coverage (figure 4, left). For the sample 422 the dose is obviously chosen better. Here, the structures are completly developed (figure 4, left).
Consequently, this method of producing micropores works in case of choosing the right coverage of particles and right dose. The fading in the edges of the holes can only be surpressed by using a x-ray mask with cylindric structures.

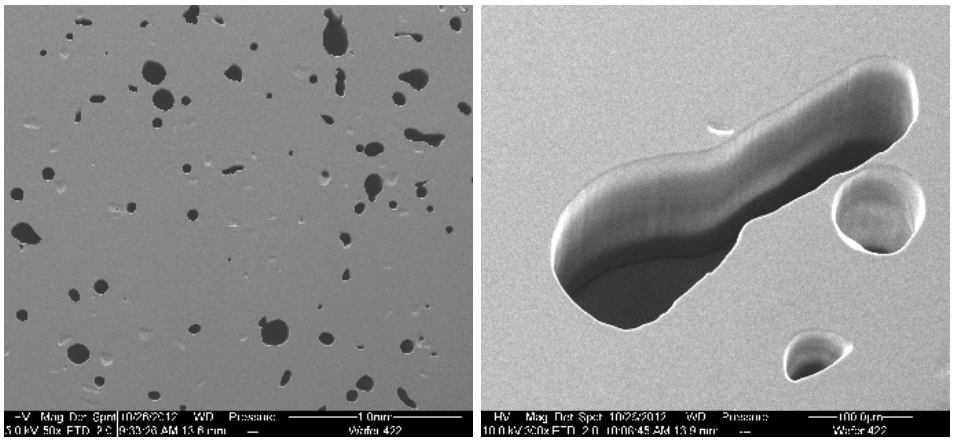

**Figure 4:** SEM images of sample 422.


### Acknowledgement

We would like to thank Dr. Alex von Bohlen (Leibniz-Institut für Analytische Wissenschaften - ISAS - e.V.) for taking the SEM images. We also would like to thank the DELTA machine group for providing synchrotron radiation and for technical support. T. Brenner thanks the NRW Forschungsschule 'Forschung mit Synchrotronstrahlung in den Nano- und Biowissenschaften' for financial support.


## References


[1] V. Saile, U. Wallrabe, O. Tabata, J.G. Korvink, O. Brand, G.K. Fedder, C. Hierold (Eds.), *LIGA and its applications*, Wiley-VCH (2009).

# Upgrade of the ISASline (Beamline 2)

M. Brücher, A. von Bohlen, R. Hergenröder

Leibniz-Institut für Analytische Wissenschaften – ISAS – e.V.

Bunsen-Kirchoff-Str. 11, 44139 Dortmund

The purpose of the activities at the ISASline was the modernization of the beamline in order to provide a technically up-to-date and reliable experimental station for research with X-rays in the low-keV range. To this end, several essential components have been replaced or modified.

**Beamshutter**

The ISAS purchased a new, water cooled beamshutter from FMB (Berlin) in order to replace the previously used prototype. The beamshutter was delivered and tested in February/March. For the installation (done during the summer shutdown in July), the beam pipe was adapted to place the beamshutter close to the radiation protection wall. This way, the optional installation of a beam position monitor is prepared. After the radiation safety test, the new beamshutter was put into operation.

**Fig. 1:** Installation of the new beamshutter.

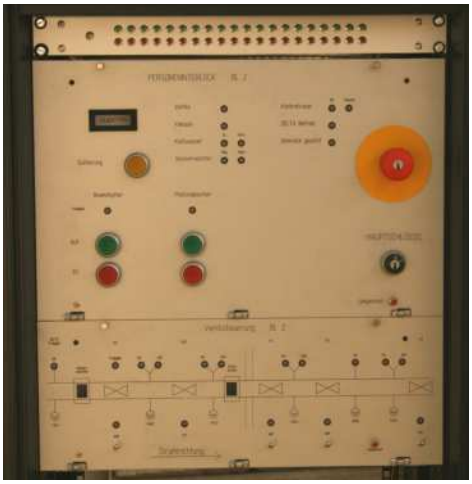

**Fig. 2:** The panel of the SPS interlock and vacuum control system.

**Beryllium window**

Previous test showed that a window is necessary to protect the vacuum of the storage ring and to ensure a stable operation of the beamline. A beryllium window was installed between the last valve and the monochromator and connected to the cooling water circuit of DELTA.

**Interlock control system**

Besides the beamshutter, the interlock and valve control system was replaced. A rack equipped with Siemens S7 elements was assembled with front panels including the devices for the control and status monitoring of valves, vacuum gauges, and the beamshutter and photon absorber and for the communication with the DELTA safety circuits.

**Software**

A Windows program has been developed, including functions controlling the Amptek X123SDD detector, for the storage and plot of the spectra and for the transmission of stepper motor commands to the goniometer and the monochromator. The communication of the software with the electronic equipment of the beamline has successfully been tested; also first fluorescence spectra have been recorded using the synchrotron radiation.

**Characterization of the white beam**

In October, first measurements with the white radiation were performed. Several scattering and fluorescence spectra were recorded in order to estimate the energy range and the possible use of alternative monochromator crystals. The spectra were calibrated using the fluorescent emission of different targets. Fluorescence lines with energies from 0.53 keV (O) up to 22.16 keV (Ag) were recorded with an intensity maximum of scattered radiation between ca. 6 and 12 keV.

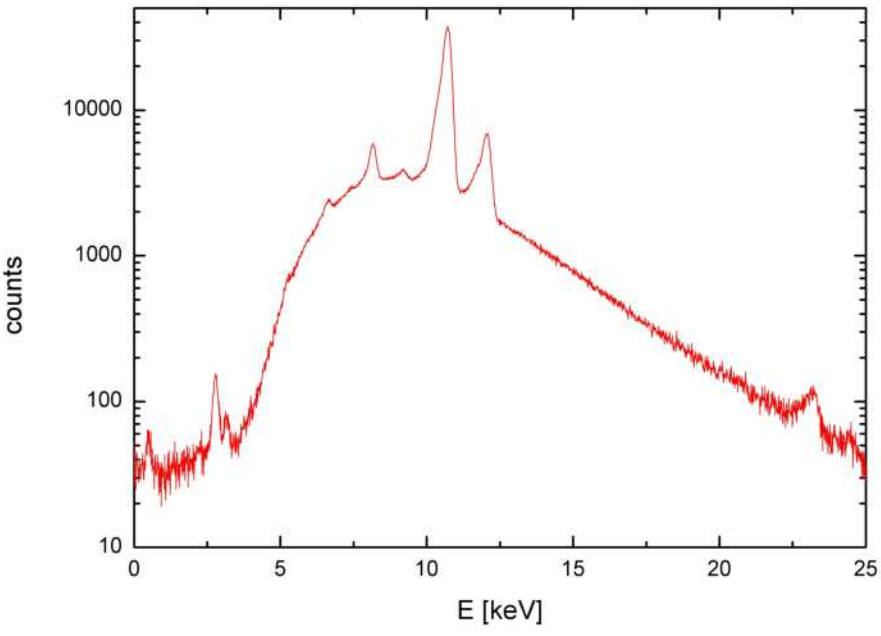


**Fig. 3:** The spectrum of the white beam scattered at a Pb target.

# The New Short-Pulse Facility at DELTA

M. Bakr, M. Höner, H. Huck, S. Khan, R. Molo, A. Nowaczyk, A. Schick, P. Ungelenk, M. Zeinalzadeh
Center for Synchrotron Radiation (DELTA), TU Dortmund University, 44227 Dortmund, Germany

*Coherent Harmonic Generation and Coherent Terahertz Pulses*

A new radiation source is under commissioning at DELTA since 2011 [1,2]. Based on the so-called Coherent Harmonic Generation principle (CHG) [3,4], the primary goal is to combine the short wavelengths of synchrotron radiation sources with the ultrashort pulse duration of modern laser systems. In recent years, three storage rings have implemented the CHG principle: ELETTRA in Italy [5] (discontinued due to FERMI@ELETTRA), UVSOR II in Japan [6], where CHG is only possible at a reduced beam energy, and DELTA. Currently, DELTA is the only source capable of producing CHG radiation in standard user operation mode.

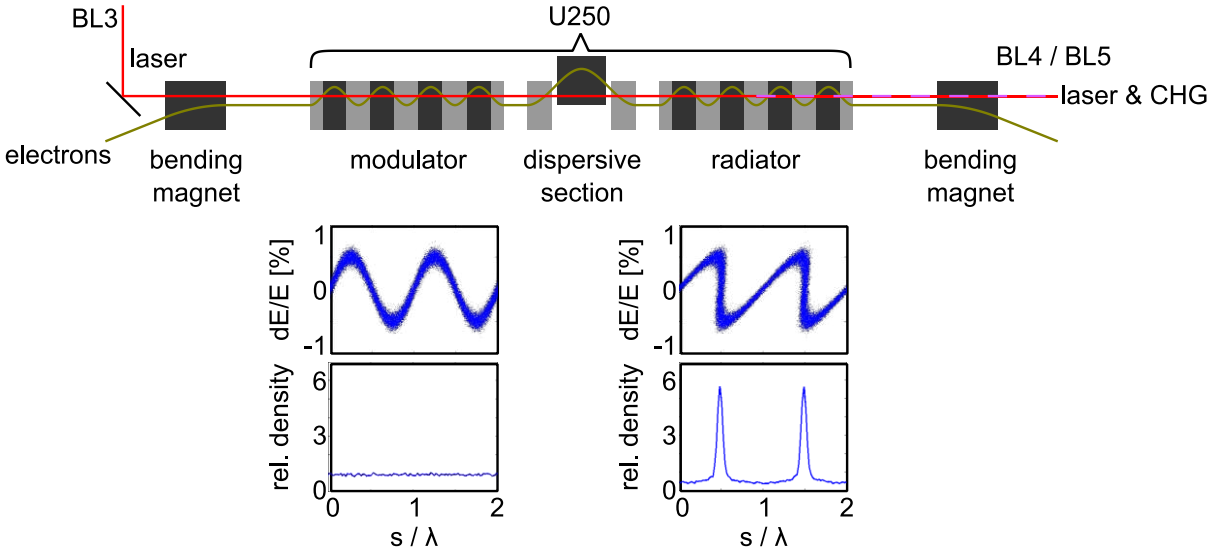


Pulses with a duration of 40 fs from a Ti:sapphire laser (beamline 3) at wavelengths 800 nm, 400 nm or 266 nm copropagate with the electron bunches in the modulator (first part of the undulator U250), which leads to an energy modulation in a short slice of the bunches. A dispersive section (center part of the U250) transforms the energy modulation into a sequence of microbunches, which emit coherent radiation at harmonics of the original laser wavelength in the radiator (last part of the U250). The CHG radiation is extracted by the diagnostics beamline BL4 or the VUV beamline BL5. The goal of this project is to provide CHG pulses with a duration of 50 - 100 fs and a wavelength of 53 nm (5th harmonic of 266 nm, i.e. 23 eV).

Due to path length differences in the following dipole magnets, a sub-picosecond dip in the longitudinal electron density is formed. Based on previous experience at BESSY [7], a THz beamline (BL5a) has been constructed in order to extract and detect coherent THz pulses caused by this density modulation [8].

*First Results*

A first laser-induced THz signal was obtained in June 2011 and first CHG signals were detected soon thereafter. Efforts in 2011 then concentrated on characterizing the CHG and THz radiation and on lowering the CHG wavelength down to the 4$^{th}$ harmonic of 800 nm.

*Recent achievements*

During 2012, the facility has been improved in many ways, including the installation of additional diagnostics, stabilization of the laser beam by completing and evacuating BL3 and covering the laser beam path, and using a reflective telescope instead of lenses. CHG radiation at 200 nm can now be generated with a factor of 50 between coherent UV pulses and the incoherent background. Taking into account the difference in pulse duration (50 fs versus 100 ps) and the Fourier-limited bandwidth of the CHG pulses, the true factor between the peak intensities is about $10^5$.

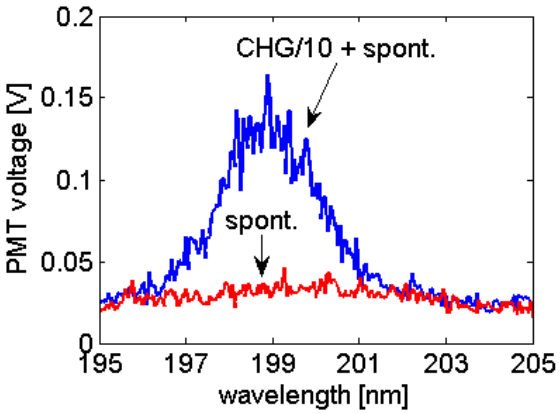


The laser wavelength has been switched to 400 nm using an SHG unit, allowing to produce even shorter CHG wavelengths [9]. By adjustment of the electron orbit and optimization of a hybrid filling pattern, CHG and THz radiation could successfully be generated during user operation. An additional laser beamline has been constructed, which will be used to send a fraction of the laser pulses directly to the end station of BL5, thereby enabling pump-probe experiments with CHG pulses. The THz radiation is used for finding, optimizing and maintaining the laser-electron overlap in the undulator, for electron beam diagnostics [10] as well as for future laser-pump and THz-probe experiments.

*Outlook*

Increasing of the dispersive section at the U250 center by flexible rewiring of the coils will lead to higher CHG intensities. In order to detect CHG radiation with wavelengths shorter than 200 nm, a vacuum tank will be installed at BL4. Eventually, CHG pulses will be detected and used in BL5. At the THz beamline, a new FT-IR spectrometer has been installed and commissioning will begin shortly.

Planning for a follow-up project based on echo-enabled harmonic generation [11] and femtoslicing [12] has begun. Both principles allow for the production of ultrashort pulses with even shorter wavelengths. This project will require additional undulators and a re-design of DELTA's northern straight section.

*Acknowledgement*

The work is supported by BMBF, DFG and the Federal State NRW. It is a pleasure to thank our colleagues at DELTA and the Faculty of Physics for their continuous support. Furthermore, the project has profited from the expertise of our colleagues at BESSY/HZB, MLS/PTB, DESY, ANKA/KIT, and SLS/PSI.

*References*

[1] H. Huck et al., Proc. FEL'11, Shanghai, 5 (2011).
[2] S. Khan et al., Sync. Rad. News 24, No. 5, 18 (2011).
[3] R. Coisson and F. D. Martini, Phys. Quant. Electron. 9, 939 (1982).
[4] R. Prazeres et al., Nucl. Instr. and Meth. A 272, 68 (1988).
[5] G. De Ninno et al., Phys. Rev. Lett. 101, 053902 (2008).
[6] M. Labat et al., Nucl. Instr. and Meth. A 593, 1 (2008).
[7] K. Holldack et al., Phys. Rev. Lett. 96, 054801 (2006).
[8] M. Höner et al., Proc. IPAC'11, San Sebastian, 2939 (2011).
[9] A. Schick et al., Proc. IPAC'12, New Orleans, 1619 (2012).
[10] P. Ungelenk et al., Proc. IPAC'12, New Orleans, 770 (2012).
[11] D. Xiang and G. Stupakov, Phys. Rev. ST AB 12, 030702 (2009).
[12] A. A. Zholents and M. S. Zolotorev, Phys. Rev. Lett. 76, 912 (1996).

# BL10: Universities of Siegen and Wuppertal

*Konstantin Istomin[1], Ralph Wagner[2], Anne Hüsecken[1], Stefan Balk[2], Nail Bulatov[1] and D.Lützenkirchen-Hecht[2]*
*[1]Universität Siegen [2]Universität Wuppertal*

In August 2012 a joint team of researchers from universities of Siegen and Wuppertal finished the commissioning of the new beamline BL10. The beamline is devoted to materials science research with the focus on X-ray diffraction and absorption spectroscopy measurements. The beamline will be also used partly for educational purposes. Future experiments include:

1. Precise single crystal diffraction
2. Charge density studies
3. Fatigue studies in metals
4. Transmission and fluorescence EXAFS measurements
5. Reflection mode EXAFS, making use of the diffractometer

Results of test measurements (EXAFS and powder diffraction with the Pilatus 100K detector and point (NaI) detectors) are shown in Fig. 1.

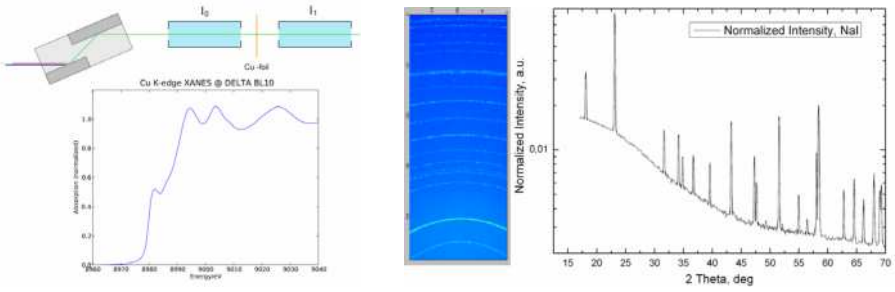


Fig.1 Test measurements EXAFS Cu K-Edge (left); Quartz powder diffraction recorded with Pilatus (centre) and point detector (right) [Poster presented at the 11th international conference on synchrotron radiation instrumentation in Lyon, August 2012].

The measured K-absorption edge of copper is in excellent agreement with reference measurements at other instruments. Both diffraction patterns obtained with the 2D and point detectors show that high-quality powder diffraction measurements can be carried out the beamline.

Two successful experiments have been already performed at the beamline. The first one was a measurement of fatigue in duplex (austenite/ferrite) stainless steel by the group from Siegen. Fig 2 (left) shows a diffraction pattern in reflection geometry of a mechanically pre-fatigued sample after $10^4$ cycles with stress amplitude of 450 MPa recorded with the Pilatus 2D detector. The pattern shows

spots indexed for austenite (A) and ferrite (F) reflections. The penetration depth at 15keV amounts to few µm focussing on the most damaged sample region. Although the sample is illuminated with a beam of 1about x1 mm², individual diffraction spots appear allowing for grain resolved analysis.

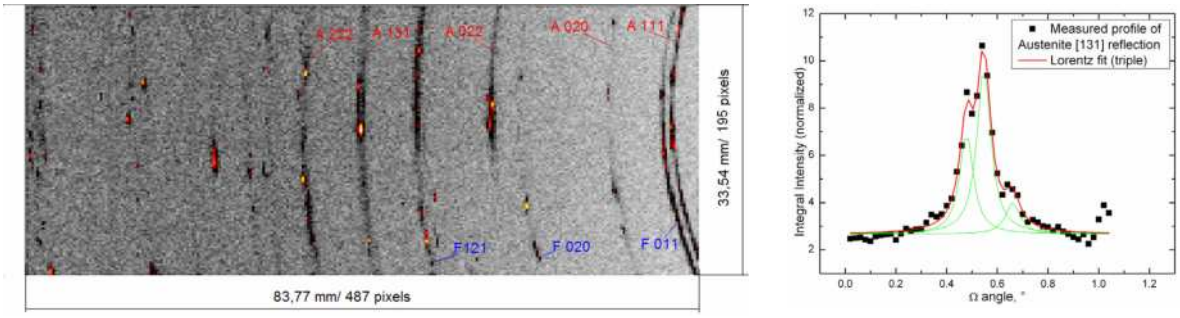


Fig.2 Diffraction pattern of a fatigued duplex stainless steel sample (left). Rocking curve of an Austenite [111] reflection (right).

The peak width of each grain was probed by rocking the sample within an angular interval of ±2° and recording 2D diffraction frames at each angular position. Then the spot intensity was plotted as function of rocking angle, ω. (Fig 2, right). Resulting rocking curves behave differently for ferrite and austenite reflections. Ferrite reflections normally have Lorentzian shape and the FWHM corresponds to the experimental resolution. In contrast to this the peak shape of austenite reflection often is not a single Lorentzian but composed by several sub-peaks separated by few tens of degrees. This splitting behaviour was used as indicator of fatigue. The sample has been probed at various positions along the sample length axis in order to correlate the degree of fatigue damage with the distribution of stress applied during the fatigue treatment. The data evaluation is ongoing.

The other one was in-situ X-Ray diffraction studies on Li-air electrodes by a joint effort of the universities of Delft (NL), Waterloo (CDN) and Wuppertal (see report of S. Ganapathy et al. this annual report). Other proposals for 2012 include measurements of the converse piezoelectric effect (University of Siegen) and studies of ZnO dopants (University of Paderborn).

The existing projects along with further modifications of the beamline will be continued in 2013.

# Development and testing of a SiPM-Camera for XPS using P47/ZnO:Ga-scintillator

K. Schennetten[1,2], S. Hannig[1,2], D. Handschak[1,2], F. Schönbohm[1,2], T. Lühr[1,2], C. Keutner[1,2], U. Berges[1,2], and C. Westphal[1,2]

[1]Experimentelle Physik 1 - Technische Universität Dortmund, Otto-Hahn-Str. 4, D-44221 Dortmund, Germany
[2]DELTA - Technische Universität Dortmund, Maria-Goeppert-Mayer-Str. 2, D-44221 Dortmund, Germany

**14th November 2012**

We report investigations on the applicability of Silicion Photo Multipliers (SiPM) and P47/ ZnO:Ga-scintillators for x-ray photoelectron spectroscopy (XPS) on silicon samples. Conventional XPS setups consist of a channeltron-detector attached to a Concentric Hemispherical Analyzer. The first one multiplicates and detects the electrons energy-separated by the latter. The disadvantage of this technique is the limited lifetime of the multiplier inside the channeltron. Hence we investigated the replacement of the channeltron by two different scintillators attached to a micro channel plate (MCP) and SiPMs (Fig. 1, r.). Those consist of Geiger-Mode Avalanche Photo Diodes capable of single-photon-detection. Here 36 SiPMs are arranged in an array (Fig. 1, l.) in order to detect the flash produced by the scintillator.

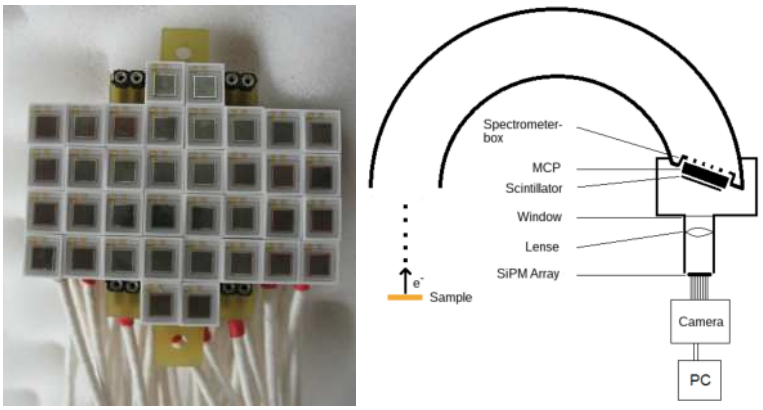


Figure 1: Left: Array of 36 SiPMs. The unused pins allow to rearrange the SiPMs. Right: Investigated setup for XPS-measurements

Fig. 2, l. shows the count rate measured by three different SiPMs as function of the discriminator-threshold set by the detector electronics. Each measurement has been performed for a regular signal ($SiO_2$-peak) and noise, that means closed beamshutter. Since the experimental data show a constant count rate for high thresholds, the noise is avoided by selecting a threshold of 2 V. The high resolution XPS spectrum of (Fig. 2, r.) shows the

$SiO_2$-peak and clearly reveals the separation of the $2p_{1/2}$ and $2p_{3/2}$ orbitals of the Si-peak. In conclusion, the setup works as a proof of principle and further investigations using faster scintillators are required.

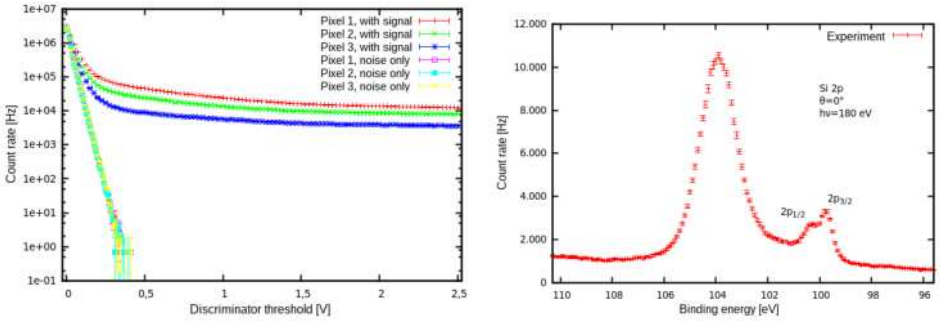


Figure 2: Left: measured count rates for three different pixels of the SiPM-array in dependence of the discriminator threshold. Noise-measurements have been performed with closed beamshutter, that means without photoelectrons. Right: XPS spectrum of the Si 2p orbital on an oxidized silicon surface. The peaks at 104 eV and 100 eV correspond to the $SiO_2$- and Si-peak, respectively. The spectrum reveals the separation of the latter peak into the $2p_{1/2}$ and $2p_{3/2}$ orbital.

## BEAMLINE 5: SPIN POLARIZED PHOTOEMISSION FROM $Bi_2Te_3$ AND $Sb_2Te_3$ TOPOLOGICAL INSULATOR THIN FILMS

**L. Plucinski[1], A. Herdt[1,2], S. Döring[2], G. Bihlmayer[3], G. Mussler[4], D. Grützmacher[4], S. Blügel[3], C.M. Schneider[1,2]**

[1]Peter Grünberg Institute PGI-6, Forschungszentrum Jülich, Jülich, Germany;
[2]Fakultät für Physik, University of Duisburg-Essen, Duisburg, Germany;
[3]Peter Grünberg Institute PGI-1, Forschungszentrum Jülich, Jülich, Germany;
[4]Peter Grünberg Institute PGI-9, Forschungszentrum Jülich, Jülich, Germany.

The surface electronic properties of the important topological insulators (TIs) *$Bi_2Te_3$* and *$Sb_2Te_3$* thin films grown on *Si(111)* [1] are shown to be robust under an extended surface preparation procedure which includes exposure to atmosphere and subsequent cleaning and recrystallization by an optimized *in-situ* procedure under ultra-high vacuum conditions. Clear Dirac-cone features are displayed in high-resolution angle-resolved photoemission spectra from the resulting samples, indicating insensitivity of the topological surface state to cleaning-induced surface roughness and stoichiometry [2].

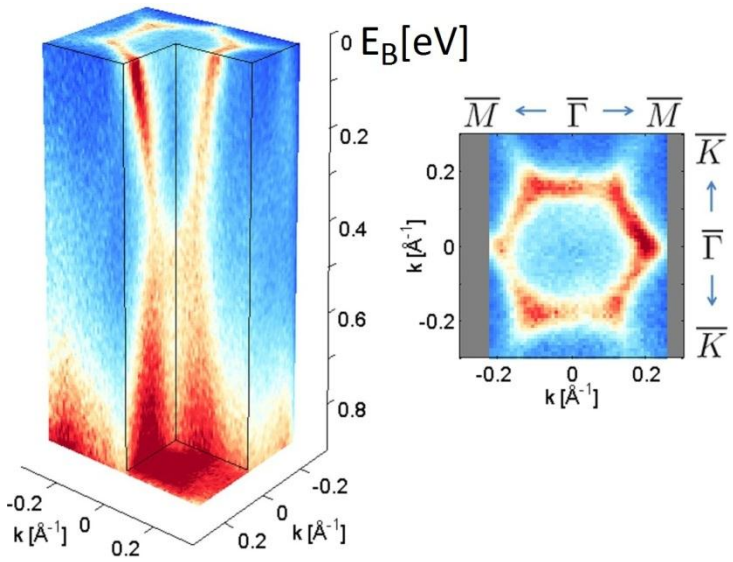


Figure 1: Angle-resolved photoemission results from the *$Bi_2Te_3$* thin film performed using 21.2 eV photons (*HeI* discharge) on the sample kept at 15K [1]. Left panel shows the 3D band structure with the warped Dirac cone and right panel shows the hexagram structure of Fermi surface.

Momentum-resolved spin polarized photoemission (*spin-ARPES*) spectra of the ensemble of the electrons emitted from these surfaces show up to 45% in plane spin polarization in the Dirac cone near the Fermi level [3], which is consistent with our *ab initio* theoretical results and with previous predictions [4] which find spin polarization in the order of 40-50% averaged over the

surface quintuple layer. We also find a non-zero out of plane spin polarization component in $Bi_2Te_3$ hexagram Fermi surface qualitatively consistent with the Dirac cone warping model [5].

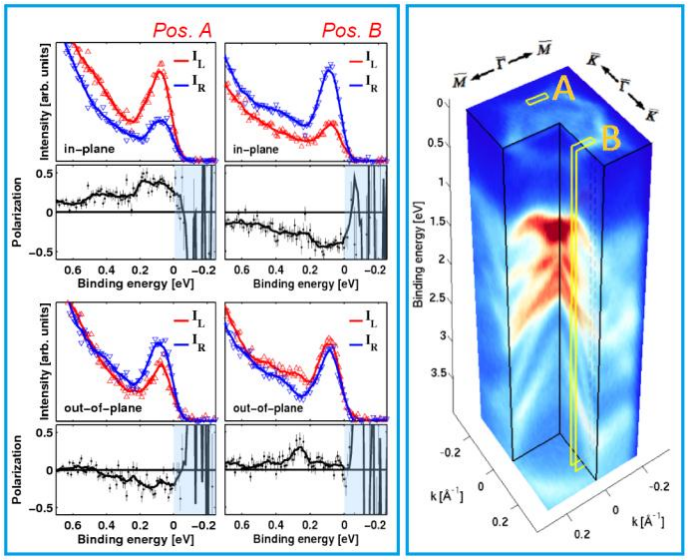


Figure 2: *Left panel* shows spin-polarized data from $Bi_2Te_3$ taken near the Fermi level on selected k-space locations along the $\overline{\Gamma K}$ direction, as indicated in the band structure image in the *right panel*. In the *left panel* the top row indicates the in-plane spin-vector components, whereas the out-of-plane components are plotted in the middle row. The deduced spin-asymmetries $P_x$ and $P_z$ and their respective standard deviations are also plotted in respective subplots.

Our results confirm the robustness of the mechanism of topological protection due to the band character inversion between the bulk and surface, as a result of the spin-orbit coupling and bulk symmetry breaking at the surface. They suggest that in $Bi_2Te_3$ and $Sb_2Te_3$ systems, due to spin-orbit entanglement, this mechanism produces spin polarization of only 50% or lower at the Fermi level, which has important consequences for possible applications of these materials in spintronics. Furthermore additional effects, related to the photoemission process, may influence the spin polarization values measured by *spin-ARPES* [6].


[1] J. Krumrain, G. Mussler, S. Borisova, T. Stoica, L. Plucinski, C.M. Schneider and D. Grützmacher, J. Cryst. Growth 324, 115 (2011).
[2] L. Plucinski, G. Mussler, J. Krumrain, A. Herdt, S. Suga, D. Grützmacher, and C. M. Schneider, Appl. Phys. Lett. 98, 222503 (2011),
[3] A. Herdt, L. Plucinski, G. Bihlmayer, G. Mussler, S. Döring, J. Krumrain, D. Grützmacher, S. Blügel, C. M. Schneider, under review as of Nov 2012 (arXiv:1210.2241).
[4] O. V. Yazyev, J. E. Moore, and S. G. Louie Phys. Rev. Lett. 105, 266806 (2010),
[5] L. Fu, Phys. Rev. Lett. 103, 266801 (2009).
[6] C.-H. Park and S. G. Louie, Phys, Rev. Lett. 109, 097601 (2012).

# Investigation of the MgO absorbate and the MgO/Fe interface by means of XPS and XPD

D. Handschak[1,2], F. Schönbohm[1,2], T. Lühr[1,2], C. Keutner[1,2], U. Berges[1,2], and C. Westphal[1,2]

[1]Experimentelle Physik 1 - Technische Universität Dortmund, Otto-Hahn-Str. 4, D-44221 Dortmund, Germany
[2]DELTA - Technische Universität Dortmund, Maria-Goeppert-Mayer-Str. 2, D-44221 Dortmund, Germany

**7th November 2012**

We report a combined high-resolution photoemission (XPS) and photoelectron diffraction (XPD) investigation of a magnesium oxide adsorbate on an Fe surface. Magnesium oxide is an appliciable insulator in magnetic tunnel junctions (MTJ) based on tunnel magnetoresistance (TMR) [1]. TMR-components are also of interest in the research of magnetoresistive random access memories (MRAM) [2, 3, 4]. In this study we report on the crystalline properties of the MgO adsorbate and the MgO/Fe interface. The results of the diffraction patterns revealed an interface with oxidized iron layers and partially shifted magnesium layers in a halite structure.

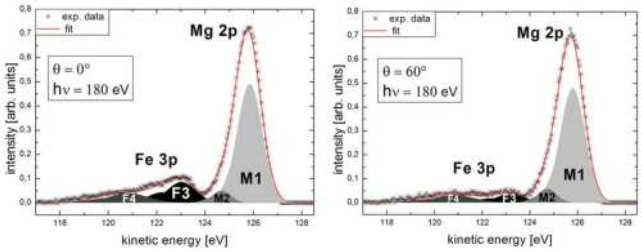


Figure 1: XPS spectra of Mg 2p and Fe 3p signals, which are seperated by a few eV only. The Fe 2p decreased for the surface sensitive detection at polar angle of $\theta = 60°$. The components M1, M2, F3 and F4 correspond to $Mg^{2+}$-state, Mg bulk, Fe bulk, and oxidized Fe-state signals, respectively.

The high resolution XPS core level spectra of the Mg 2p and Fe 3p shown in Fig. 1 prove a successful preparation of the topmost Mg layers. A strong $Mg^{2+}$ state is displayed in the high-resolution spectra of the Mg 2p signal. The Fe 3p spectra reveal components corresponding to iron bulk and oxidized states. Due to the overlap of Mg 2p and Fe 3p the experimental diffraction pattern is truncated either to Mg or Fe. Although the experimental data are truncated the mutual influence is still existing since the components F3 and M1 overlap, because they are Gaussian in energy. The analysis of the XPD patterns shown in Fig. 2 yielded in an interface structure consisting of two iron oxides layers located on an iron bcc elementary cell. The MgO layers are of halite structure with a rotation of 45° with respect

to the Fe bcc surface. The best agreement was achieved for a model where every second Mg layer is shifted slightly with respect to the other ones. This structure model is supported by the superposition of the individual simulated diffraction pattern of Mg 2p and Fe 3p signals, as displayed in Fig. 3.

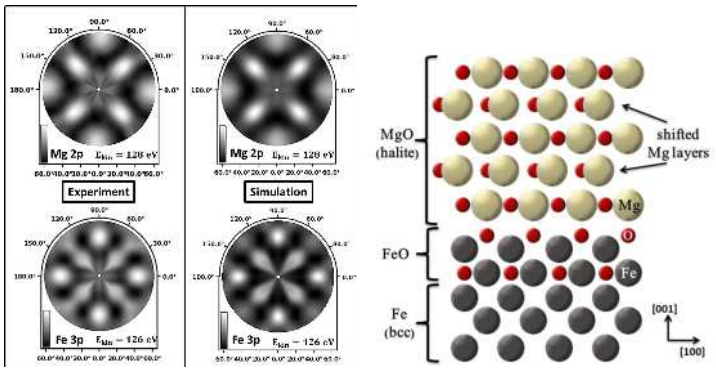


Figure 2: Left: Comparision of the XPD pattern for Mg 2p and Fe 3p signals. Both simulated pattern are in excellent agreement with the experimental data. Right: Schematic structure model of the MgO/FeO/Fe system, all simulations are based on this model.

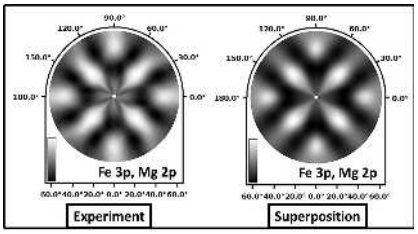


Figure 3: The experimental XPD pattern of MgO/Fe in comparision with the superposition of the best simulated pattern for Mg 2p and Fe 3p displayed in Fig. 2. The superposition is in an excellent agreement with the experimental data.

## References


[1] M. Julliere, Physics Letters A 54, 225 (1975)

[2] M. Xue, W. Li, F. Wang, J. Yao, and J. Lu, Vacuum 85 (2010)

[3] S. Parkin *et al.*, Nature Materials 3 (2004)

[4] S. Tehrani *et al.*, Proceedings of the IEEE 91, 703 (2003)

[5] D. Handschak *et al.*, Phys. Rev. B submitted (2012)

# Structure determination of $HfSi_2$ islands on Si(110)

**F. Schönbohm[1,2,*], T. Lühr[1], D. Handschak[1], S. Döring[2], U. Berges[2], and C. Westphal[1,2]**

[1] Experimentelle Physik 1 - Universität Dortmund, Otto-Hahn-Str. 4, D 44221 Dortmund, Germany
[2] DELTA - Universität Dortmund, Maria-Goeppert-Mayer-Str. 2, D 44227 Dortmund, Germany
[*] corresponding author: frank.schoenbohm@tu-dortmund.de

(November 2012)

In Fig. 1 the thermal dependence of the Hf 4f, Si 2p, and O 1s photoemission signals are presented. The peak intensities for all signals are determined by curve resolutions and normalized to their respective maximum. The Hf 4f remains constant for temperatures up to 730°C. After annealing at 770°C the intensity drops to $I_{Hf} \approx \frac{1}{6}$th of its former value. The O 1s intensity shows a slight increase for temperatures up to 625°C and is dropping after the annealing step at 730°C. After annealing at 770°C the O 1s intensity drops to $I_O \approx \frac{1}{19}$th of the original value. This intensity loss is a clear indication of removing oxygen from the sample surface. The Si 2p intensity remains constant for temperatures below 770°C and increases after annealing at 770°C. The Si 2p peak is the only component that gains intensity after annealing at 770°C. All these effects can be explained due to removal of the oxygen from the sample surface and the formation of $HfSi_2$ islands at the same time.

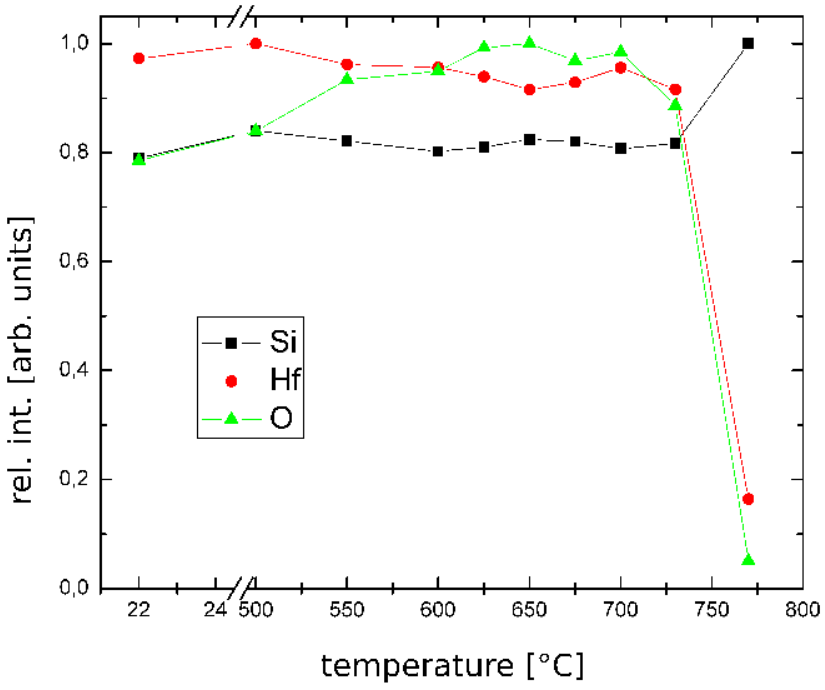


Figure 1: Thermal development of $HfO_2$ on a Si(110) surface upon stepwise annealing.

In order to investigate the atomic structure of the newly formed $HfSi_2$ islands photoelectron diffraction patter were recorded directly after annealing at temperatures of 770°C. In Fig. 2 the experimental and the simulated diffraction patterns are presented. As a numeric measure for comparing the two diffraction patterns the R-Factor is introduced. The codomain of the R-Factor is the interval $0 \leq R \leq 2$. An R-Factor of $\mathrm{R} = 0$ shows perfect agreement between the experimental and the simulated pattern, whereas $\mathrm{R} = 1$ and $\mathrm{R} = 2$ correspond to a random and an inverted pattern, respectively. The R-Factor between the two pattern presented in Fig. 2 has a value of $\mathrm{R} = 0.05$.

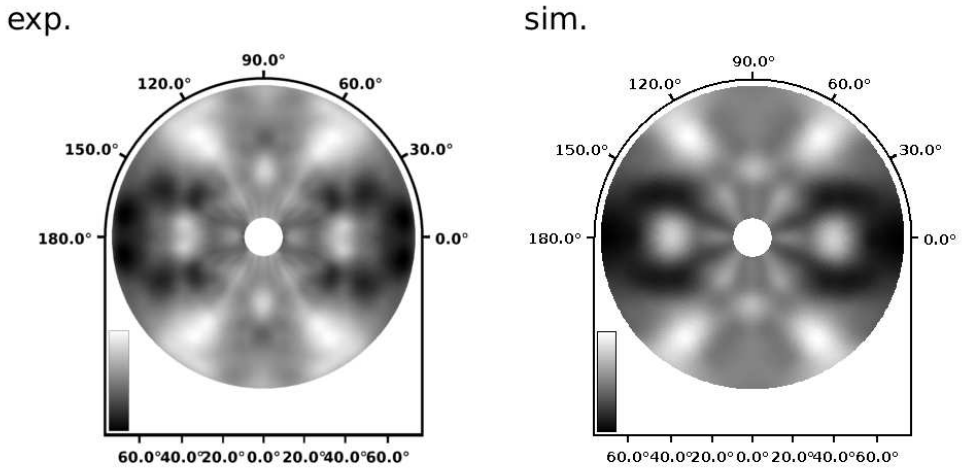


Figure 2: Experimental and simulated XPD pattern of $HfSi_2$ islands on a Si(110) surface.

**Acknowledgments:**
This work was supported by the Land Nordrhein-Westfalen, the NRW Forschungsschule and the Bundesministerium für Bildung and Forschung. Thanks go to the staff of DELTA for continuous support during the beamtimes.

# Antiferromagnetic coupling in Fe/Ru/Ni as function of the Ru-Thickness

M. F. Tesch, M. C. Gilbert, H.-Ch. Mertins, D. E. Bürgler[1] and C. M. Schneider[1,2]

Münster University of Applied Sciences, Stegerwaldstr. 39, D-48565 Steinfurt
1) Forschungszentrum Jülich GmbH, Peter Grünberg Institut (PGI-6), D-52425 Jülich, 2) Fakultät f. Physik & Center for Nanointegration Duisburg-Essen (CeNIDE), Uni Duisburg-Essen, D-47048 Duisburg

Magnetic multilayer systems are essential for sensors or data storage devices [1]. One powerful tool for the development of such devices is the magneto-optical spectroscopy with polarized synchrotron radiation. It allows for magnetic depth profiling and for an element selective characterization of each individual magnetic layer. We investigated 4 samples of the trilayer-system Fe/Ru/Ni with fixed Fe thickness (4 nm), fixed Ni thickness (5 nm) and various Ru thicknesses of $d$ = 0.6, 0.8, 1.0 and 1.2 nm. The experiments were performed at Beamline 12 using our newly built XMAPS polarimeter [2]. The magnetization device TetraMag [3] produces variable magnetic fields in longitudinal, transversal or polar geometry each up to +/- 500 mT which allows for the reversal of even strongly coupled magnetic layers. We exploited T-MOKE spectroscopy in the low energy range near the 3p edges of Fe and Ni with the advantage of providing a 1000 times lager reflectivity compared to the reflectivity at often investigated 2p edges resulting in a better signal to noise ratio.

The magnetic signal and in particular the orientation of the magnetization of the individual layer is detected via the transversal magneto-optical Kerr-effect. The T-MOKE asymmetry $A$ is calculated from the difference of the reflectance $R(B_{T+/-})$ for anti-parallel orientations of the transversal magnetic field $B_{T+/-}$ according to

$$A = \frac{R(B_{T+}) - R(B_{T-})}{R(B_{T+}) + R(B_{T-})}.$$

Figure 1 shows the T-MOKE asymmetry for the Fe/Ru/Ni-trilayer with $d$ = 0.8 nm Ru-thickness. Typical spectra with strong signals of up to 12% at the Fe 3p edge (54.5 eV) and up to $\pm 6\%$ at the Ni 3p edge (66 eV) are observed. The relative sign of the Ni peak at 66eV depends on the parallel / anti-parallel orientation of the magnetic Ni moments with respect to that of Fe. Fig. 1 shows that this magnetic orientation depends on the applied magnetic field strength.

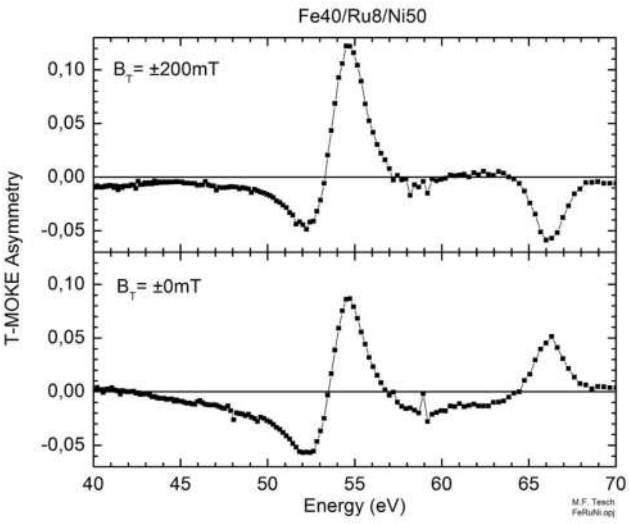


**Fig.1**: T-MOKE asymmetry of Fe/Ru/Ni with 0.8nm Ru with light of 40° grazing incidence. Top: detected at +/-200 mT. Bottom: detected at 0 mT, i.e. reducing the field from +/-200 to 0 mT. Strongest peaks occur at the Fe 3p edge (54.5 eV) and at the Ni 3p edge (66 eV). For details of the switching behaviour see text.

For strong fields $B_T = \pm 200$ mT (Fig. 1 top) the magnetic moments are assumed to be aligned parallel while for small magnetic fields close to $B = \pm 0$ mT the magnetic moments of Ni and Fe are assumed to be aligned anti-parallel. This model is sketched in Fig. 2, centre, and can be verified by monitoring hysteresis curves at the Fe 3p edge (54.5 eV) and at the Ni 3p edge (66 eV), respectively. This is done by measuring the reflected intensity for fixed photon energy while sweeping the external field.

While the Fe layer shows a typical hysteresis curve, switching near ±6 mT (Fig. 2, bottom) the Ni layer shows two hysteresis curves (Fig. 2, top). In addition to the primary hysteresis curve, which follows exactly that of Fe, a second hysteresis curve occurs which ranges from -100 to +100 mT. Beyond these values the signal is constant up to ±500 mT (not shown in Fig. 2). The switching occurs between |B| = 30 mT and |B| = 90 mT with a width of about 32 mT. The coupling is sketched in the centre of Fig. 2. At small fields the Fe and Ni layers are coupled antiferromagnetically. Increasing the external field up to +/-90 mT forces the magnetization of the Fe and the Ni layer in a parallel orientation.

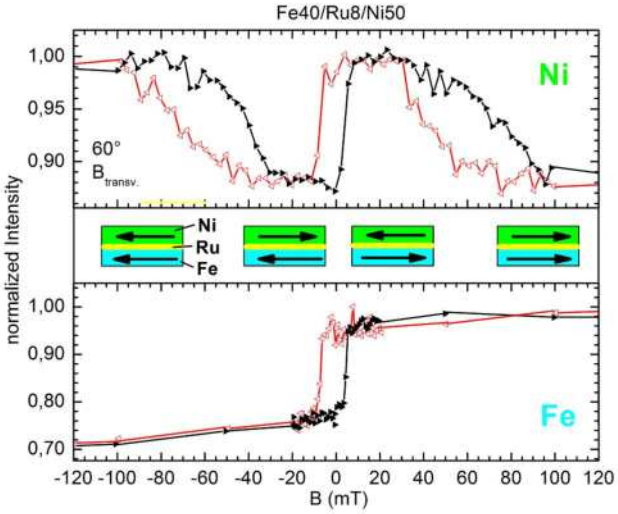


**Fig.2**: Magnetic switching in Fe/Ru/Ni with 0.8 nm Ru. Top: Hysteresis curve of Ni detected at 66 eV. Bottom: Hysteresis curve of Fe detected at 54.5 eV. Centre: alignment of the individual magnetic layers.

The strength of the coupling depends on the thickness of the Ru-layer and is reflected in the saturation field of the hysteresis curves. Figure 3 shows the Ni hysteresis as function of the Ru thickness. The coercivity of the primary hysteresis changes from 15 mT for 0.6 nm Ru, over 6 mT and 10 mT for 0.8 and 1.0 nm Ru, respectively, to 1 mT for 1.2 nm Ru. The magnetic saturation is large for thin Ru layers and smaller for thick Ru layers. It decreases from about 350 mT for 0.6 nm Ru to about 45 mT for 1.2 nm Ru. For all samples the hysteresis of Fe, measured at 54.5 eV, coincides with the primary hysteresis of Ni (see Fig. 2) but it is not shown in Fig. 3.

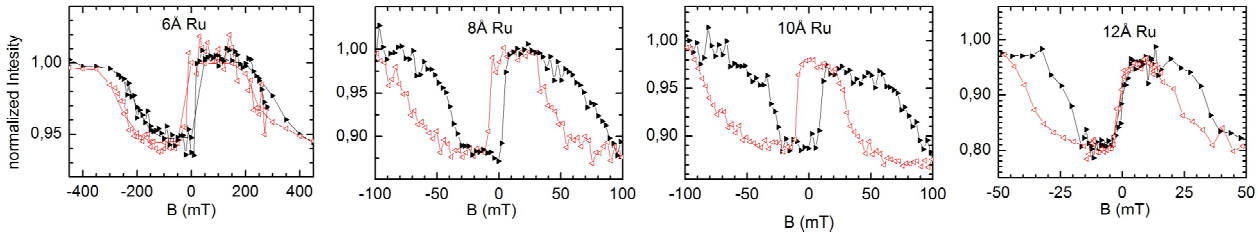


**Fig.3**: Hysteresis of the Ni layer for different Ru layer thickness, measured at 66eV. The saturation field strength and the coercivity depend strongly on the thickness of the intermediate Ru layer.

Our measurements reflect the long range magnetic coupling between magnetic Fe and Ni layers across intermediate paramagnetic Ru-layers. The saturation fields are a measure of the Ru-thickness dependent coupling strength and are expected to show the oscillatory behaviour of the sinusoidal RKKY function. However, for a detailed analysis the investigation of additional Fe/Ru/Ni layers with various Ru thicknesses is necessary and a comparison to experiments of other research groups on similar samples [4] will be helpful.

We acknowledge the help of U. Berges and C. Keutner and the Ministry for Innov. Sci. and Techn. NRW (INST 232/5–1).

[1] J. Stöhr, H.C. Siegmann, *Magnetism*, Springer Series in Solid State Sciences, Berlin (2006)
[2] M. F. Tesch, M. C. Gilbert, H.-Ch. Mertins et al., submitted to Journal of Physics D
[3] M. Gilbert, H-Ch. Mertins, M. Tesch et al., Rev. Sci Instruments **83**, 025109 (2012)
[4] D. Rudolf, C. La-O-Vorikat, M. Battiato et al., Nature Commun. 3:1037 (2012)

# Annual report Delta synchrotron 2012

A. *Bakirov[1], S.N. Chvalun[1],L. Grodd[2], E. Mikayelyan[2], S. Grigorian[2]*
*[1]Institute of Synthetic Polymer Materials, Moscow, Russia*
*[2]Solid-State Physics, University of Siegen, Germany*

Our work on Delta Synchrotron consisted of two parts: investigating structure and morphology of monolayer Langmuir-Blodgett films formed by alkylquinquethiophene derivatives and by alkylcrownbipyridium molecules. These substances are very promising for creation of OFETs and OLEDs according to mobility and fluorescent measurments. An important advantage of these materials that they can be solution processed.

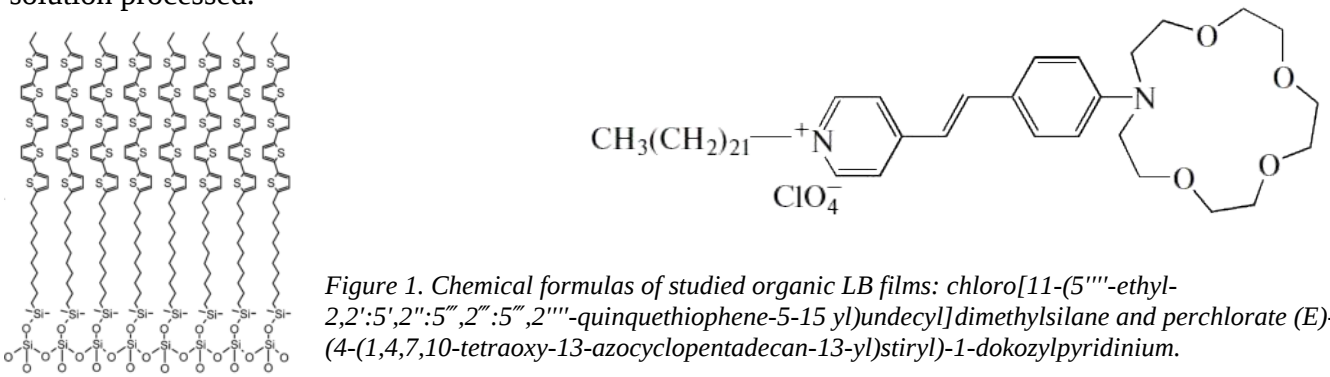

*Figure 1. Chemical formulas of studied organic LB films: chloro[11-(5''''-ethyl-2,2':5',2'':5'',2''':5''',2''''-quinquethiophene-5-15 yl)undecyl]dimethylsilane and perchlorate (E)-4-(4-(1,4,7,10-tetraoxy-13-azocyclopentadecan-13-yl)stiryl)-1-dokozylpyridinium.*

X-ray reflectivity measurments performed at BL9 station at DELTA, Dortmund using 12.38 keV energy revealed interesting results of film morphology: stochastic fits are shown in fig. 2 with a three slabs model in absolute electron density monolayer reconstruction. Films transferred to silicon substrates at different LB pressures show different angles of tiophene groups to the plane normal. So we can conclude that Langmuir−Blodgett technique employed under the optimal conditions is a very promising method for formation of the self-assembled crystalline monolayer films. For the linear organosilicon functionalized quinquethiophene Si-Und-5T-Et with vertical orientation of oligothiophene fragments that should be appropriate for practical application in OFETs. It should be emphasized that the LB technique allows one to prepare Si-Und-5T-Et monolayers significantly faster than the previously used method of self-assembling from solution.

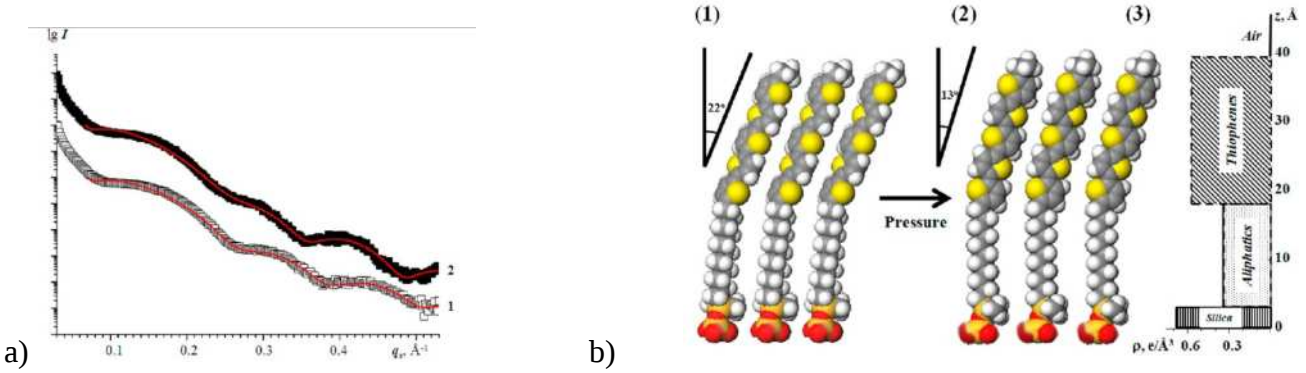


*Figure 2 a) Reflectivity curves for LB films of Si-Und-5T-Et, prepared from 0.33 g/L solutions at pressures of 30 mN/m (1) and 40 mN/m (2). Best stochastic fits are shown by red curves. b) Molecular models of the LB monolayer structure at 30 mN/m (1) and 40 mN/m (2).c) Plot (3) shows distribution of the electron density along the z axis perpendicular to the substrate surface.*

The second part of study was related to the bipyridene derivatives also made a large improvement of understanding of layer structure using XRR method. Experiment showed large differences when changing transfer and adding $Ba^{2+}$ ion. Length of the three parts of molecule with different electronic densities can be derived and compared to molecular model. This is in a good agreement with excimer organization theory which was proposed as a result of in-situ fluorescence studies.

# Adsorption of nanoparticles at the solid - liquid interface

Thorsten Brenner[1], Michael Paulus[1], Martin A. Schroer[1], Sebastian Tiemeyer[1], Christian Sternemann[1], Johannes Möller[1], Metin Tolan[1], Patrick Degen[2], Heinz Rehage[2]

[1] Fakultät Physik/DELTA, Technische Universität Dortmund, Maria-Goeppert-Mayer-Str.2, 44227 Dortmund, Germany

[2] Fakultät Chemie, Technische Universität Dortmund, Otto-Hahn-Str. 6, 44227 Dortmund, Germany

The use of nanoparticles in technology and human life has been established in the last decade. They can be found e.g. in cosmetics, drugs and surface coatings [1-3]. However the interaction between nanoparticles and the human body is widely unknown. Thus, possible risks caused by the use of nanoparticles are part of social discussion, see for example [4,5].

In our study we have investigated the adsorption of differently charged nanoparticles onto negatively charged silica at the solid liquid interface. Maghemite ($\gamma$-$Fe_2O_3$) and gold (Au) nanoparticles are used offering opposite surface charges. In order to analyze the formation of nanometer thick layers at the solid liquid interface x-ray reflectivities were recorded using the 27 keV x-ray reflectivity setup of beamline BL9 at DELTA [6]. The average particle radius of the polydisperse maghemite nanoparticles was determined by small angle x-ray scattering (SAXS) at the beamline BL9 [7].

The maghemite nanoparticle solution was stabilized by the addition of HCl leading to a zeta potential of +50 mV. The zeta potential of the gold nanoparticles was -45 mV. The particle solutions were pre characterized by dynamic light scattering showing polydisperse size distributions with a most probable particles radius of 7.5 nm in the case of maghemite and 2.0 nm for the gold nanoparticles.

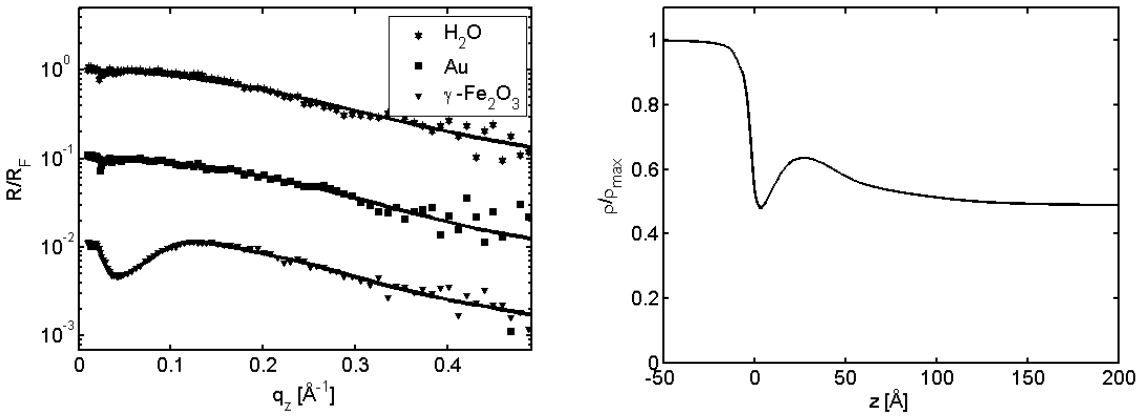


Figure 1: left: X-ray reflectivities of the silica liquid interface using pure water, gold nanoparticles solution and maghemite nanoparticles solution. The reflectivities are normalized by the Fresnel reflectivity. Solid lines represent the refinements of the data. Right: Electron density profile of the silica maghemite nanoparticle solution interface obtained by a fit of the reflectivity. [10]

Figure 1, left shows the reflectivities taken from the liquid solid interface normalized by the Fresnel reflectivity. The reflectivities were analyzed using the Parratt algorithm [8] applying the effective density model [9]. The reflectivity of the silica – gold nanoparticle solution interface shows no adsorption of particles at the interface which can be explained by the electrostatic repulsion between the gold and the silica surface. However, the reflectivity of the silica – maghemite nanoparticle solution shows the formation of a few nanometer thick adsorption layer reflecting the attractive electrostatic interaction between silica and maghemite. In order to get a deeper insight in the layers structure a logarithmic particle size distribution was used to simulate the layers electron density profile. Assuming the formation of a monolayer agreement with experimental data was obtained. Figure 2, left shows the layers electron density profile together with simulation. To achieve comparable data to the SAXS measurements on polydisperse solutions, the particle radius distribution function is weighted by $r^6$ yielding a most probable radius of r = (8.8 ±0.2) nm. The SAXS data of the maghemite bulk solution are shown in figure 2 on the right side. The most probable radius found within the Guiner approximation was determined to (11.2+0.5-2.0) nm, thus shifted to a slightly higher value compared to the adsorbed layer. However within the errorbars the bulk particle size distribution is mainly resembled in the adsorbed layer. For further details see [10].

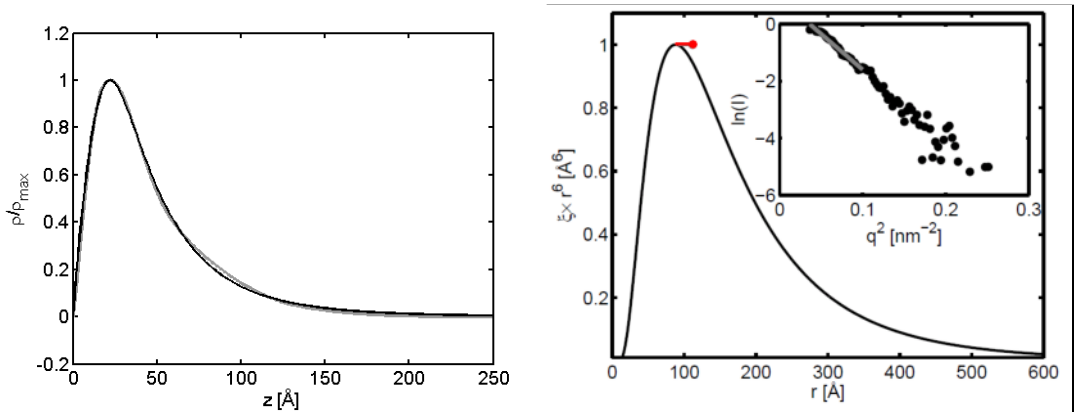


Figure 2: Left: Electron density of the adsorbed maghemite layer (gray line). The black line shows the simulated density profile using a logarithmic particle size distribution function. Right: Logarithmic particle size distribution function (solid line). The red point shows the result of the SAXS analysis. The SAXS data are shown in the inset [10].

[1] A. Shukla, P. Degen, and H. Rehage, J. Am. Chem. Soc. **129** (2007) 8056. [2] A. Wittstock, V. Zielasek, J. Biener, C. M. Friend, M. Bäumer, Science **327** (2010) 319. [3] V. Gewin, Nature **443** (2006) 137-137. [4] http://www.bund.net/nanodatenbank/ (2012). [5] http://www.bmbf.de/pub/nanopartikel_kleine_dinge_grosse_wirkung.pdf (2012). [6] M. Paulus, D. Lietz, C. Sternemann, K. Shokuie, F. Evers, M. Tolan, C. Czeslik and R. Winter, Journal of Synchrotron Radiation **15** (2008), 600. [7] C. Krywka, C. Sternemann, M. Paulus, N. Javid, R. Winter, Ali Al-Sawalmih, Sangbong Yi, D. Raabe, M. Tolan, Journal of Synchrotron Radiation **14**, 244 (2007). [8] L. Parratt, Phys. Rev. **95** (1954), 359369. [9] M. Tolan, X-ray scattering from Soft Matter Thin Films; Springer: Berlin, 1999. [10] T. Brenner, M. Paulus, M. A. Schroer, S. Tiemeyer, C. Sternemann, J. Möller, M. Tolan, P. Degen, H. Rehage, Journal of Colloid And Interface Science **374**, 287–290 (2012).

# Crystallites formation during MBE growth Si-doped of InAs nanowire on GaAs(111)B

A. Davydok[a], T. Rieger[b], A. Biermanns[a], M. Saqib[a], M. Lepsa[b] and U. Pietsch[a]

[a]*Festkörperphysik, Universität Siegen, Walter-Flex-Str. 3,57072, Siegen, Germany*
[b]*Peter Grünberg Institut (PGI-9), Forschungzentrum Jülich, Jülich, Nordrhein Westfalen, 52425, Germany, and cJülich Aachen Research Alliance for Fundamentals of Future Information Technology (JARA-FIT), Germany*

Group III-V semiconductor nanowires (NWs) demonstrate interesting electrical and optical properties and are very promising for the fabrication of future semiconductor devices. Using molecular beam epitaxy (MBE), NWs from almost any semiconductor materials can be combined with nearly any substrate, independent from lattice mismatches [1]. The additional use of a doping material can provide variability in device design and selectivity for future device structures [2]. An important prerequisite for the self-assisted growth of the nanowires is the existence of a good quality oxide layer on the substrate regarding both homogeneity and thickness.

In previous experiments we investigated the self-assisted InAs NW's grown on GaAs (111)B substrates doped by different amount of Si and covered with a thin layer of Hydrogen Silsesquioxan (HSQ). The HSQ is etched in diluted HF to ~ 6nm thickness and SEM images show the HSQ is wavy and in some parts is damaged. We performed statistical analysis to clarify the influence of doping on NWs morphology. We have determined the ratio of parasitic island and nanowire growth, which has been determined from the SEM images (considered surface area of 20 x 10 µm²). The ratio of 0.7 determined for undoped samples indicates that on average a larger number of crystallites are formed compared to the number of NWs (fig. 1). With increasing doping level, this ratio quickly decreases down to a value of 0.25, showing that each nanowire is accompanied by four islands. Also we compared the size of islands, it is larger in highly doped samples compared to the lower or undoped ones. This finding has been confirmed counting the volume ratio of material growing as NWs or islands, respectively. From measured RSM we determined the integrated intensities of the Bragg reflection attributed to NWs and islands. The ratio of these intensities is proportional to the scattering volume of the respective objects and shows the same tendency as obtained from the analysis of the SEM images. Both support the assumption that the majority of material is present in form of crystallites.

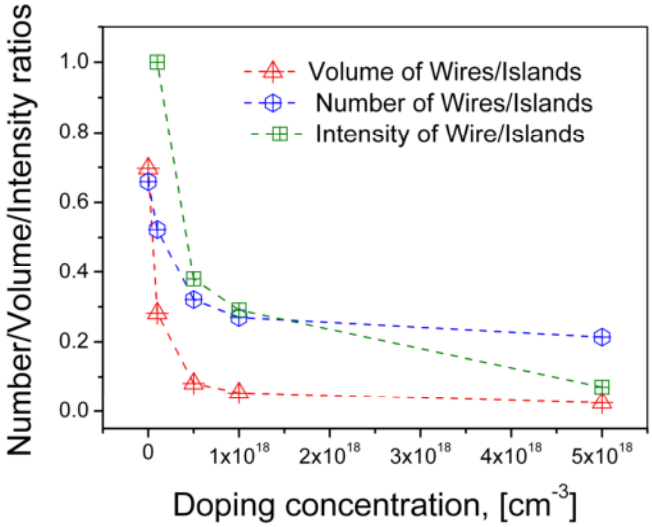


Figure 1. Ratios of NW volume/number/intensity to crystallite volume/number/intensity as function of Si doping concentration.

The observed tendency of enhanced crystallite formation from damage coating layer with increasing silicon concentration can be ascribed to a change in surface diffusion of the group III materials on the oxide covered surface, namely a reduced diffusion length [3]. In a qualitative way, our findings can be explained assuming that the diffusion length of group III atoms on the oxide layer decreases with increasing Si concentration.

In future we are planning to complete statistical analyses with more varieties doping level. Also in-plane component of such nanostructure have not been characterized yet. It is can be done at BL9 with Huber six-circle diffractometer which dedicated to GID.

**References**

[1] Schubert L., Werner P., Zakharov N., Gerth G., Kolb F., Long L., Gösele U., Tan T., Appl. Phys. Lett. 84, 4968, 2004

[2] Li J., Zhang Y., To S., You L., Sun Y., ACS Nano, 8, 6661–6668, 2011

[3] Wirths S., Weis K., Winden A., Sladek K., Volk C., Alagha S., Weirich T., von der Ahe M., Hardtdegen H., Lüth H., Demarina N., Grützmacher D., Schäpers Th., J. Appl. Phys. 110, 053709, 2011

# Analysis of lattice defects in silica zeolites of the structure type MFI

Isabel Großkreuz*
*Faculty of Geosciences, Institute for Geology, Mineralogy and Geosciences, Ruhr-Universität-Bochum 44801 Bochum*
**isabel.grosskreuz@rub.de*

High silica zeolites are very important and widely spread in industrial use. They consist of three-dimensional corner-linked [$TO_4$]-tetrahedra, with mainly silicon as T-atom. However, other tetrahedra-forming atoms like aluminium or titanium are possible as well. The microporous framework structure is characterized by framework densities below 21 tetrahedrally coordinated atoms within 1000 $Å^3$ of material. These structures exhibit internal cages and pores resulting in internal surfaces. During synthesis pores and cages are filled with water or molecules. After removal of the water, these large pores allow the industrial use of zeolites as molecular sieves, catalysts, carrier for functional molecules, adsorbates and ion exchangers.

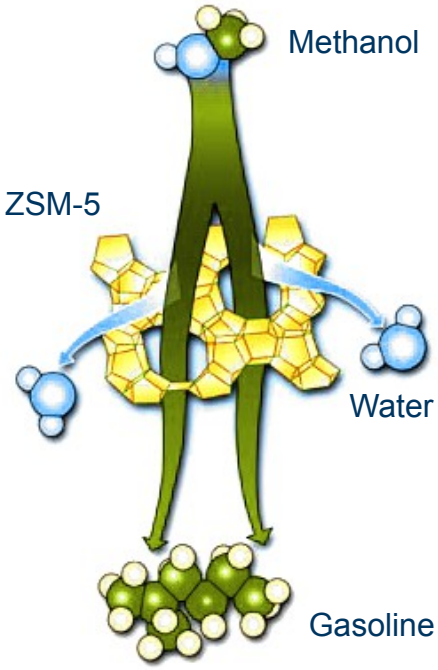


figure 1: catalysis reaction by exxon mobil: http://www.exxonmobil.com/Apps/RefiningTechnologies/files/sellsheet_09_mtg_brochure.pdf

The structure type MFI is realized in the high silica ZSM-5-zeolite, which catalizes the reaction from e.g. methanol to gasoline, which is presented in **figure 1**. Both figures highlight the very large channel system with diameters up to 5.6 Å allowing the diffusion of large molecules such as methanol and water. Other applications are acid-catalyzed reactions such as the isomeration of meta-xylene to para-xylene.
The material is of very high importance for the petrochemical industry. Due to the simplicity and low costs of synthesis the material proofs very promising for practical uses. The ZSM-5 also exhibits properties of high stability and resistance against acidity.

However, during synthesis, the structure does not grow perfectly and exhibits defects of various kinds typical for zeolitic materials. Weare interested in structural defects consisting of interrupted Si-O-Si bonds in the silicate framework. These defects do not show in conventional XRD-analysis but only in expensive and complex NMR- or IR-analysis. Examples of these kinds of defects are shown in **figure 2**. We are able to differentiate between vacancies, so called hydroxyl-nests (encircled), where one silicon-atom is missing and replaced by four hydrogen-atoms and simple non-bridging defects (in box). Non-bridging defects exhibit a broken off bond between two silicon-atoms with an excess of one oxygen and two hydrogen-atoms.
Depending on the synthesis procedure, the as-made zeolite may be perfect or full of defects. These defects may heal during calcination at 540°C where the organic molecule (TPA) and the water within the pores evaporate or they persist even after thermal annealing.

We assume that hydroxyl-nests are less likely to heal than non-bridging defects. The excess oxygen and hydrogen-atoms occupying the non-bridging defects may simply form water-molecules during calcination and heal. Removing the hydrogen-atoms occupying the hydroxyl-nest via calcination leaves behind a vacancy, which cannot be filled, since a silicon-atom is missing.

Two types of MFI-structured zeolites were synthesized. One series of synthesis dealt with a high-silica product using tetramethyl orthosilicate as a silicon-oxide source as well as tetrapropylammoniumhydroxide as a structure directing agent. Another series was performed using the same materials but also ammonium fluoride as a fluorine source.

Analysis of both materials using X-ray powder diffraction on a Siemens D5000 copper radiation Debye-Scherrer geometry diffractometer showed no significant difference whatsoever. Sample powder were stored in a silica-glass capillary with a diameter of 0.1 mm. Best possible stepsize proved to be 0.007861 °2θ with shutter speeds of 7 seconds per step. We were able to scan a range from 5 °2θ up to 95 °2θ to ensure a full pattern Rietveld structure-determination up to high angles. Time of measurement extended up to 71 hours for each sample. The full width half maximum parameter proved to be around 0.13 for selected peaks.

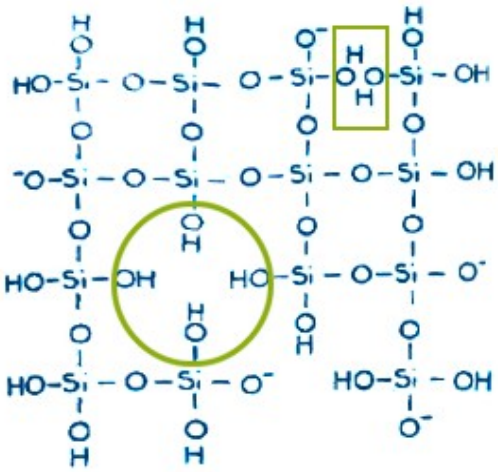

figure 2: local defects in siliceus zeolitic framework; from:J.M. Chezeau, L. Delmotte, J.L. Guth: "Influence of synthesis conditions and postsynthesis treatments on the nature and quantity of structural defects in highly siliceous MFI zeolites: A high-resolution solid state $^{29}Si$ n.m.r. study.", Zeolites, 1991, Vol. 11, 599.

The experiment at the BL09 at the DELTA facility in Dortmund included the X-Ray diffraction experiment using synchrotron-radiation.
We analized the high-silica as-made material as well as the fluorine bearing material using energies around 12,380 eV and subsequently a wavelength of 1.0015 Å. The chosen wavelength ensured easy comparability with previous XRD measurements using molybdenum as well as copper radiation sources. Additionally a wavelength close to 1 Å guarantees ideal premises for structure-determination since interatomic distances vary around 1 Å as well.

The scanning range includes angles between 4.5 °2θ up to 20 °2θ with a step size of 0.005 °2θ. Angular resolution proved to be around 0.01 and 0.02 °2θ and therefore exceedingly suited for subsequent Rietveld analysis. We obtained full width half maximum parameter around 0.02 for selected peaks and thus a factor of 10 better than the conventional X-ray powder diffraction experiment. The sample stage was mounted using rotating silica-glass capillaries with diameters between 0.1 to 0.7 mm whereas the resolution and intensity proved best by using 0.1 mm capillaries regarding the beam-size. Considering the short length of beam time (4 shifts á 8 hours) both samples were measured twice with shutter speeds of 5 seconds per step. Every measurement took up between 6 and 7 hours each.

The resulting highly resolved powder diagrams shown in detail in **figure 3** were analized applying a full pattern Rietveld structure analysis using the FullProf Suite (Rodriguez-Carvajal, *J. Physica B.* (1993), 192, 55). The two samples exhibited a well-defined variation in intensity as well as reversed intensity distribution in certain peaks. Some of the peaks of the fluorine-bearing material display shifts to higher °2θ values, which indicate smaller d-values, whereas the rest of the peaks occupy exactly the same °2θ position as the high-silica material. Applied Rietveld structure analysis resulted in an increase in agreement between experiment and simulation by a factor of at least 0.5.

In previously conducted conventional XRD determined single peaks showed distinct splitting due to the high resolution of the synchrotron radiation.

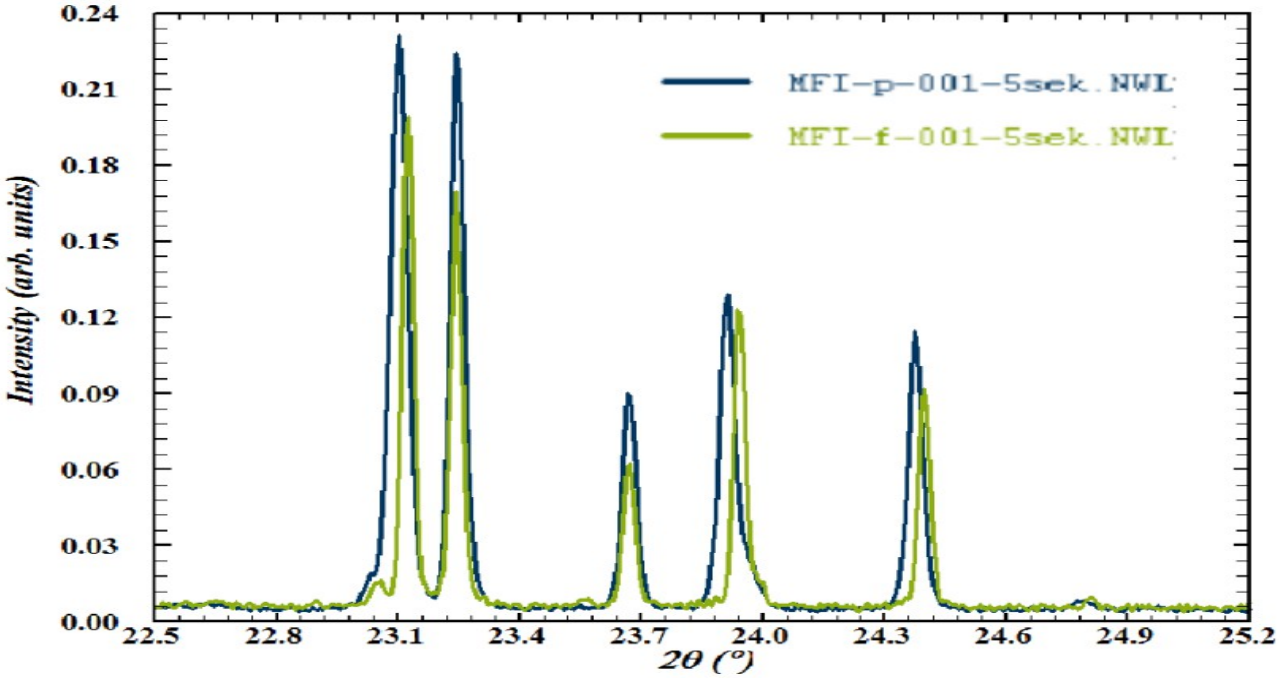


figure 3: detail synchrotron powder pattern of polycrystalline (blue) & fluorine (green) MFI converted to copper radiation; Graphics generated using WinPLOTR: a Windows tool for powder diffraction patterns analysis Materials Science Forum, Proceedings of the Seventh European Powder Diffraction Conference (EPDIC 7), 2000, p.118-123, Ed. R. Delhez and E.J. Mittenmeijer, Authors:T. Roisnel, J. Rodriguez-Carvajal.

Compared to conventional X-Ray powder diffraction plus single crystal diffraction NMR as well as IR spectroscopy the difference between both samples becomes apparent. In contrast to the fluorine-bearing material, which exhibited no defects whatsoever after synthesis, the high-silica product showed defects before and even after calcination in the form of three-coordinated silicon – if less so. Additionally the fluorine-bearing product even demonstrated five-coordinated silicon, which proves to be a defect not anticipated whatsoever. The five-coordinated silicon might explain the observed shift to lower d-values in the synchrotron powder diffraction diagram observed in **figure 3**.

The fluorine source during synthesis appears to act a structure directing agent preventing non healable hydroxyl-nests and non-bridging defects from forming.

Using a combination of techniques such as NMR and IR with PXRD, it is possible to distinguish perfect and defect as-synthesised material using data collected via synchrotron-radiation. The difference between both products becomes easily evident in the synchrotron powder pattern, which will be a useful tool in structure analysis and differentiation of perfect and defect material. The subtle fluctuations within the two sample structures become apparent using synchrotron radiation powder diffraction due to the very high angular resolution, the shorter measurement time as well as the possibility to wipe out any background noise, which ensures better comparability between different samples due to the detector installation.

# Influence of Crowding, Temperature and Pressure on Protein-Protein Interactions and Protein Stability

Sebastian Grobelny [1], Mirko Erlkamp [1], Johannes Möller [2], Christopher Rosin [1], Metin Tolan [2], and Roland Winter [1]

[1] Physical Chemistry I – Biophysical Chemistry, TU Dortmund University, Otto-Hahn-Str. 6, D-44227 Dortmund, Germany

[2] Experimental Physics I, TU Dortmund University, Otto-Hahn-Str. 4, D-44227 Dortmund, Germany

Concentration-, temperature- and pressure-dependent small-angle X-ray scattering experiments were carried out to analyze the structure and intermolecular interactions of highly crowded protein solutions. As model protein we used lysozyme over a wide range of concentrations (up to 500 mg $mL^{-1}$). For the highest protein concentrations, samples were prepared using dialysis bags (Slyde-A-Lyzer®, MWCO = 2 kDa, Thermo Scientific) applying osmotic pressure methodology. Polyethyleneglycol (PEG) with a molar mass of 35 kDa was used as main component of the dialysis buffer. The initial protein concentration amounted to $w$ = 15 %. Higher concentrations were achieved as a function of the dialysis time.

SAXS experiments were carried out at the beamline BL9 at DELTA. The X-ray energy was 10 keV, which corresponds to a wavelength $\lambda$ of 0.124 nm. The scattering curves were recorded with a CCD-detector (MAR345) with a sample to detector distance of 1 m, covering a range of momentum transfer $q$ from 0.38 to 5 $nm^{-1}$. The exposure time was 20 min. The measurements were carried out in a home-built high-pressure X-ray cell, which is equipped with two flat diamond windows of 1 mm thickness (type IIa quality, Drukker, Cuijk, The Netherlands). Further technical details are described by Woenckhaus *et al.*[1] High hydrostatic pressures up to 3 kbar - with an accuracy of 0.5 % - at steps of 250 bar were applied at a temperature of 25 °C using water as pressurising medium. Temperature control (with an accuracy of ± 0.2 °C) was achieved by a water circulation system from a thermostat through the temperature controlled jacket of the pressure cell. The time for thermal equilibration before each measurement was set to 15 min. For the SAXS measurements, a total of 25 µL of the sample was filled into the pressure cell. The scattering curves were corrected for background using the pure solvent and taking into account the different absorption factors.

Synchrotron SAXS data of two different lysozyme solutions are depicted in Figure 1. The SAXS intensity is plotted against the magnitude of the scattering vector $q$ ($q = (4\pi/\lambda)\sin\theta$, with $2\theta$ being the scattering angle). Experimental scattering curves at different concentrations are plotted together with fits that were based on the DLVO (Derjaguin-Landau-Verwey-Overbeck) potential and the mean spherical approximation (MSA) (details are described in [2] and [3]). This liquid-state method was used to extract the intermolecular protein-protein interaction potential $V(r)$ - in particular the strength $J$ of the attractive part of $V(r)$ - from the calculated intermolecular structure factors, $S(q)$. The upper curve in Figure 1 shows the scattering intensity of a lysozyme solution at a concentration of $w$ = 15 %, corresponding to the starting condition of the dialysis. In the lower part of Figure 1, the scattering curve of the lysozyme solution after 20 h of dialysis is shown. The main correlation peak, which occurs due to the presence of a structure factor reflecting protein-protein interactions, shifts to smaller $q$ values with increasing concentration. Usually, the correlation peak of dense lysozyme solutions is expected to

shift with increasing concentration to larger $q$ values, i.e. smaller distances.[4] The unusual behavior observed here can be explained by the occurrence of a second correlation peak at larger $q$ values. The attractive part of $V(r)$, $J$, increases from 2.5 to 5.9 $k_B T$ for the highly concentrated solution.

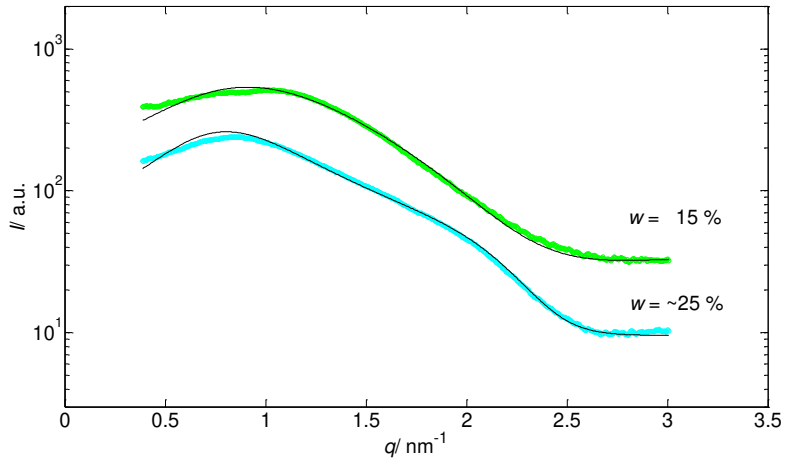


Figure 1: Experimental SAXS data $I(q)$ of lysozyme solutions (top: $w$ = 15 % starting conditions for dialysis; bottom: after 20 h dialysis ($w$ ~ 25 %) at $T$ = 25 °C and $p$ = 1 bar with corresponding fitting curves using the DLVO potential and the MSA approximation (black lines).

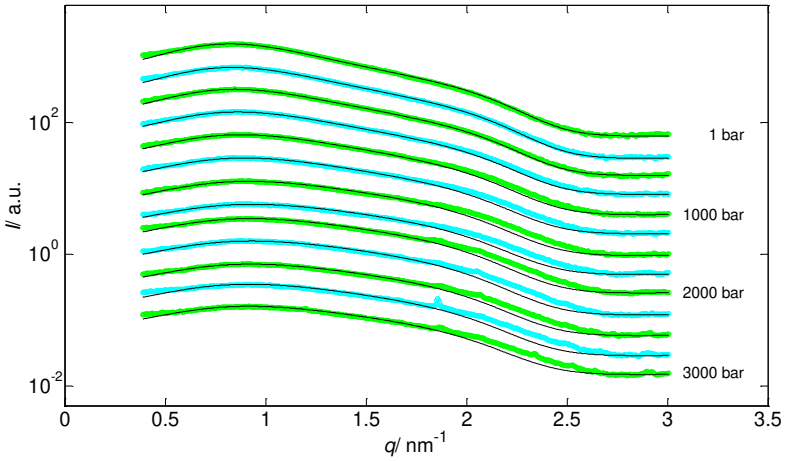


Figure 2: Experimental SAXS data $I(q)$ of lysozyme solution (20 h dialysis; $w$ ~ 25 % at $T$ = 25 °C for different pressures (250 bar steps) with corresponding fitting curves (black lines) using the DLVO potential and MSA superimposed on the experimental data.

The two broad peaks in the scattering curves at the highest lysozyme concentrations are indicative of the transition zone to crystallization. With time, formation of lysozyme crystals of a tetragonal unit cell with anisotropic compression along the $a = b$ and $c$ axis is observed. Application of high hydrostatic pressure retards protein crystallization.[3] Owing to the phase separation phenomena observed at the highest protein concentrations, the liquid state model to extract $V(r)$ cannot be used anymore.

[1] J. Woenckhaus, R. Kohling, R. Winter, P. Thiyagarajan and S. Finet, *Rev. Sci. Instrum.*, 2000, **71,** 3895-3899. [2] M.A. Schroer, J. Markgraf, D.C.F. Wieland, C.J. Sahle, J. Möller, M. Paulus, M. Tolan and R. Winter, *Phys. Rev. Lett.*, 2011, **106**, 178102. [3] J. Möller, M.A. Schroer, M. Erlkamp, S. Grobelny, M. Paulus, A. Steffen, S. Tiemeyer, F.J. Wirkert, M. Tolan and R. Winter, *Biophys. J.*, 2012, **102**, 2641–2648. [4] N. Javid, K. Vogtt, C. Krywka, M. Tolan and R. Winter, *Chem. Phys. Chem.*, 2007, **8**, 679-689.

# In situ Investigation of Structure and Electrical Performance of Poly(3-hexylthiophene) Droplets During Solidification of Thin Film OFET Devices

*L. Grodd, E. Mikayelyan, U. Pietsch, S. Grigorian*
*Solid-State Physics, University of Siegen, Germany*

**Date of experiment:** 25.06.2012 – 29.06.2012
**Beamline:** BL 9, DELTA
**Beamline scientists:** Christian Sternemann, Michael Paulus

During the past decades organic electronics has become a field of great interest. Various applications include organic solar cells, light emitting diodes and field effect transistors [1]. The desire for tailored polymers with optimized electrical properties requires thorough understanding of the underlying transport processes. Therefore, in the current in situ studies of poly(3-hexylthiophene) thin film OFET devices we investigate structural and electrical characteristics during the drop casting and drying process by grazing incidence X-ray diffraction (GIXD) and simultaneous current measurements (see also [2]).

In-situ experiments have been performed at beamline BL9 at DELTA in Dortmund using the photon energy of 12.38 keV. Thermally oxidized silicon substrates were covered with source/drain gold contacts and the sample contact area was exposed by droplets of P3HT/chloroform solution. After droplet exposure the evolution of the (100) structural peak was monitored under GIXD conditions by a fast counting Pilatus detector and an exposure time of 1 s per image. Simultaneously, the source/drain current was recorded.

Due to weak scattering of the polymer material and the short exposure time, the diffraction pattern even of the final dry state (Figure 1, top left) provide a low intense diffraction spot with very low counting statistics which makes the (100) peak hardly visible. In contrast, the sum of several of such 1 s shots clearly displays the peak (Figure 1, bottom left). In order to preserve time resolution, radial line profiles were extracted for each 1 s shot by azimuthal integration of in vicinity of the Bragg peak area (Figure 1, right).

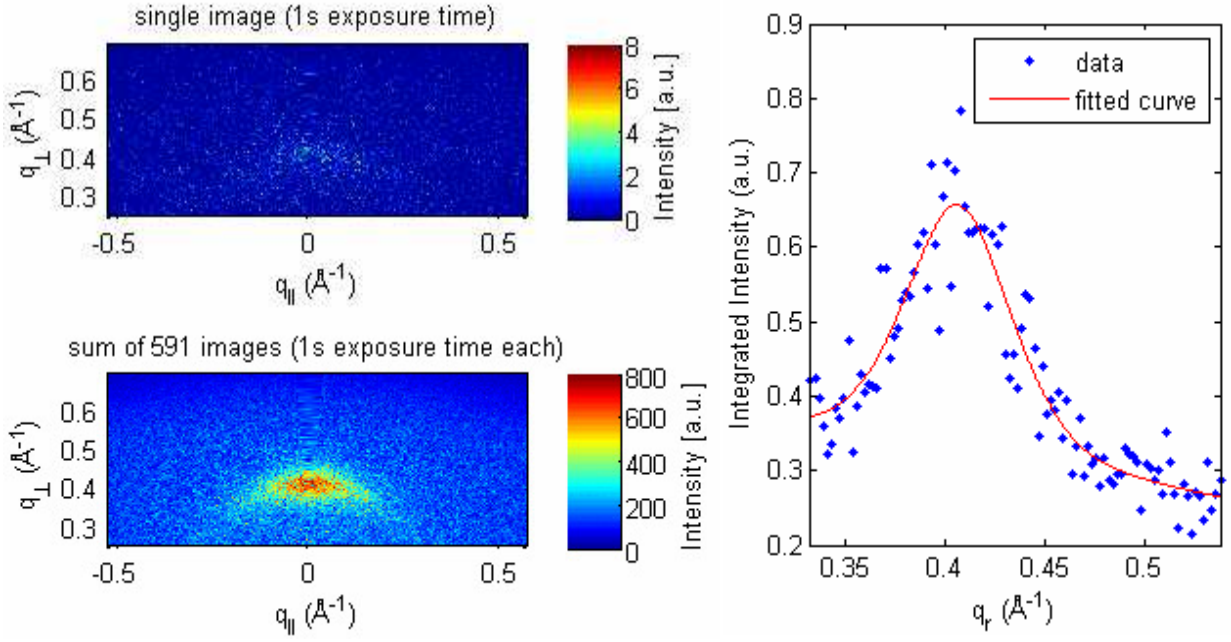


**Figure 1: 2D diffraction pattern of (100) Bragg peak for a single shot of 1s exposure (top left) and sum of 591 images (bottom left) and radial line profile for single shot extracted from azimuthal integration of Bragg peak area (right).**

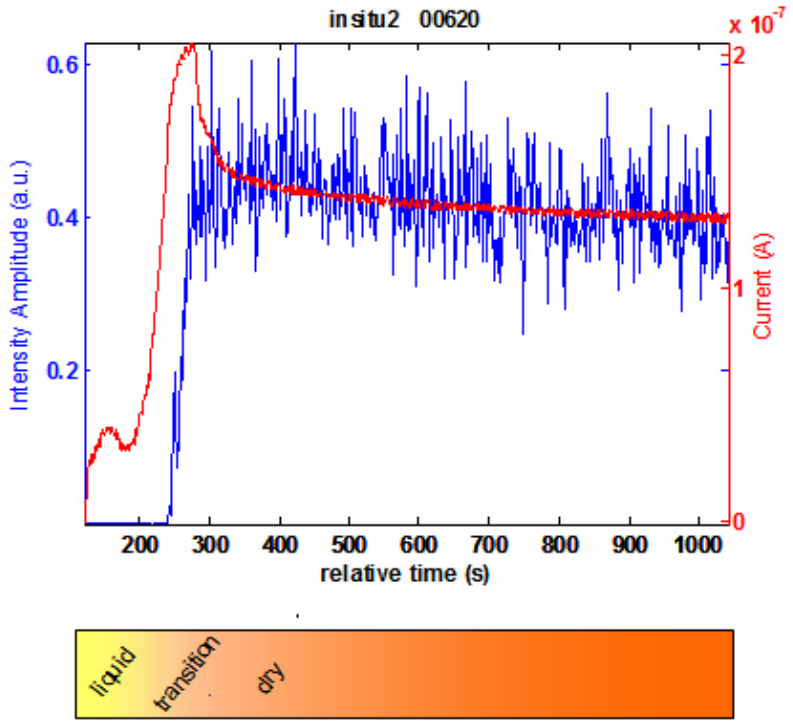


**Figure 2: Time-dependence of (100) Bragg peak amplitude (blue) and source-drain current (red) during liquid to solid transtition**

The respective peak amplitudes (Figure 2, blue dots) were determined by fitting a Pseudo-Voigt curve to the data and plotted together with the simultaneously measured source/drain current (Figure 2, red curve). Typically, the time dependence of the current features a small pre-peak in the liquid regime showing no scattering x-ray intensity (blue curve) followed by a main peak just before the dry state (rising point of x-ray intensity).

A second part of the experiment was devoted to the investigation of the structural modifications of P3HT thin films drop cast under external electric field. The aim of these investigations is to understand a role of the external electric field for enhancement of structural properties during film fabrication. In order to probe orientation effects X-ray scattering patterns under GIXD conditions were measured along and perpendicular to the direction of the applied external field.

Lateral electric field was applied during solidification with the strength of 3kV/cm by placing the substrates between capacitor plates and depositing the P3HT/chloroform solution under nitrogen atmosphere. Either DC or AC electric field were applied to align P3HT polymer chains. The ongoing research is devoted to find the optimized parameters (frequency, electric field strength) which will maximize the crystallinity with preferred orientated crystallites and will optimize the overall device performance.

**References**

**[1] H. Sirringhaus, Advanced Materials 2005, 17, 2411-2425**

**[2] L. Grodd et al., Macromolecular Rapid Communications 2012, 33, 20, 1765-1769**

# Nanopowders for X-ray cross-correlation analysis

C. Gutt[1], M. A. Schroer[1], B. Fischer[1], M. Paulus[2]
[1] Deutsches Elektronen Synchrotron DESY, Notkestr. 85, D-22607, Hamburg, Germany;
[2]DELTA/Fakultät Physik, TU Dortmund, D-44227, Dortmund, Germany

Diffraction experiments are a powerful tool for crystal structure determination. However, a complete structural analysis relies on the existence of single crystals. Otherwise, one is left with powder-averaged scattering pattern washing out the angular structure of reciprocal space. In order to overcome the powder average, the use of recent X-ray cross-correlation analysis schemes is promising. Herein, scattering intensities are correlated on azimuthal rings of constant *q* values [1-3]. With this approach the scattering pattern of a single particle or nanocrystal can be restored from the powder scattering pattern.

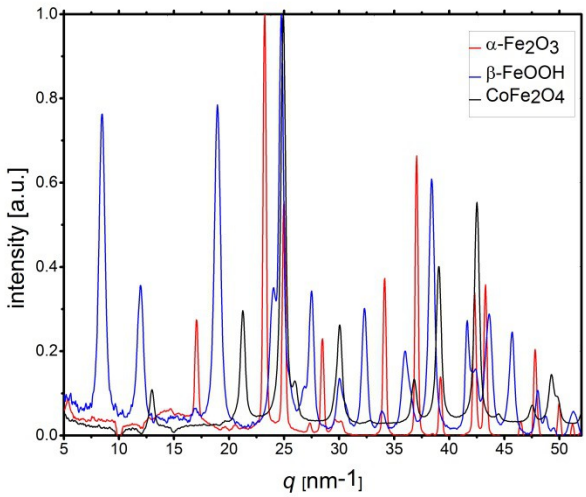


The aim of the experiment was thus to explore the possibility of reconstructing single crystal X-ray properties from the scattering intensities of ensembles of many disordered copies of it (i.e. a powder of nano-particles). Up to now XCCA has been applied to colloidal systems only, yielding spatial information on length-scales of 20-50 nm.
We therefore performed X-ray diffraction (XRD) measurements on several nanopowder samples on beamline BL9 using a photon energy $E$ = 22.5 keV. The scattering pattern were recorded using a two-dimensional MAR345 image plate. For each sample several hundred scattering patterns were taken. The azimuthally averaged scattering patterns of three samples are shown in the figure. Using iron-based nanocrystals results in sufficient scattering intensity needed for the XCCA.

The analysis of the data is still in progress. If this XCCA approach proofs to be successful, the technique is a promising tool for future X-ray free-electron laser (FEL) experiments.

References:

[1] P. Wochner, C. Gutt, T. Autenrieth, T. Demmer, V. Bugaev, A. Diaz Ortiz, A. Duri, F. Zontone, G. Grübel, H. Dosch. *Proc. Natl. Acad. Sci. USA* (2009) 106, 11511-11514.
[2] D. Saldin, H. C. Poon, M. J. Bogan, S. Marchesini, D. A. Shapiro, R. A. Kirian, U. Weierstall, J. C. H. Spence. *Phys. Rev. Lett.* (2011) 106, 115501.
[3] G. Chen, M. A. Modestino, B. K. Poon, A. Schirotzek, R. A. Segalman, A. Hexemer, P. H. Zwart. *J. Synchrotron Rad.* (2012), 19, 695-700

# Determination of melting temperatures of strained shape memory natural rubber

Benjamin Heuwers[1]*, Dominik Quitmann[1], Robin Hoeher[1], Frauke M. Reinders[1], Sebastian Tiemeyer[2], Christian Sternemann[2], Metin Tolan[2], Frank Katzenberg[1], and Joerg C. Tiller[1]

[1]*Biomaterials & Polymer Science, Department of Biochemical and Chemical Engineering, TU Dortmund, Emil-Figge-Str. 66, D-44221 Dortmund, Germany*

[2]*Fakultät Physik/DELTA, TU Dortmund, Otto-Hahn-Str 4, D-44227 Dortmund, Germany*

*email: benjamin.heuwers@udo.edu

The ability of materials, especially polymers, to change one or more properties significantly in a controlled manner upon an external stimulus is of high technological and scientific relevance. Shape memory polymers (SMPs) are attributed to a huge innovation potential for different applications such as medical devices (e.g. stents or sutures for wound closure), sensors or artificial muscles.[1-3] They can be deformed and fixed in a temporary shape (referred to as programming) until a suitable external trigger induces the recovery process and the original, permanent shape is reformed (referred to as recovery).[4-7] Recent research on SMPs covers for instance the biodegradability[8, 9], the physical adjustment of trigger temperature during programming of glass-forming[10-15] as well as crystalline-based[16, 17] polymers and the storage of very large strains[17, 18]. Furthermore various triggers have been established such as infrared light[19], UV-light[20], compression[21], alternating magnetic fields[22, 23] and electric fields[24]. A new concept in this field of research is the use of non-covalent interactions to generate a shape memory[25]. A good overview about recent advances in polymer shape memory is given by Xie[26].

Recently, we reported on lightly cross-linked natural rubber that is in contrast to common natural rubber materials capable to store large strains above room temperature based upon strain-induced crystallization[17]. Besides the great shape memory properties (stored strains up to 1000 %) the trigger temperature of one and the same network is physically tunable in a broad range (up to 70 K) during as well as after the programming procedure by variation of strain, strain rate, stretching temperature and external transverse stress[27]. We found that the application of extrinsic stress transverse to prior programming direction leads to a linear decrease of the trigger temperature. Whenever the trigger temperature is decreased below ambient temperature the crystals melt without the need of additional heat (stress-induced melting – SIM) and the permanent shape is recovered. This is the first example of tailoring physically the trigger temperature of a SMP after programming. Although the achieved range of stress-tunable trigger temperatures of natural rubber is quite impressive (40 K), there are applications that require higher trigger temperatures. Applying stress parallel to the stretching direction during programming results in an increase of $T_{trig}$ in a range of about 16 K.[28] Since the trigger temperature is directly proportional to the melting temperature of the strain-induced crystals in shape memory natural rubber (SMNR) an increase in trigger temperature is caused by a stabilization of these crystals. Therefore we explored in this study the influence of strain on the melting temperature of SMNR under constrained conditions.

**Materials.** For our experiments, specimens of lightly cross-linked natural rubber were prepared according to the two following general procedures.

Method 1: Latex-based natural rubber Neotex FA (Weber & Schaer GmbH) was mixed with 0.2 parts per hundred rubber (pphr) sulfur, 0.4 pphr zinc di-n-butyldithiocarbamat and 0.25 pphr zinc oxide and heating for 5 h at 50 °C. Subsequently, the natural rubber latex was cast into rectangular shaped molds (100 x 50 x 1.5 mm³) and dried at room temperature over silica gel for 7 days. The degree of cross-linking was determined by mechanical measurements to be 0.2 %.

Method 2: Vulcanizates of solid natural rubber were achieved by mastication of Standard Malaysian Rubber 10 (SMR 10) of 25 g for 15 minutes using a heated double-roller (Bühler & Co, Spezialwalze B5/135, speed: 15 rpm) operated at 100 °C while the gap width was continuously decreased from 3.5 mm to 0.25 mm. Subsequently the masticated NR was mixed with 0.15 pphr sulfur, 1 pphr N-Cyclohexyl-2-benzothiazolesulfenamide (CBS), 0.2 pphr zinc oxide and 1.4 pphr stearic acid for further 15 minutes and vulcanized in a heating press at 140 °C for 35 minutes. Samples exhibiting the dimensions 100 x 50 mm² with various thicknesses (1 – 2 mm) were cut. The degree of cross-linking was determined by mechanical measurements to be 0.1 %.

**Synchrotron measurements.** As previously proposed[17], we suggest that the mechanical stress has a direct influence on the stability on the crystals and thus on the trigger temperature. In order to explore this we decided to monitor the melting temperature of these crystals under constrained condition. For this purpose, differently stretched samples of both networks were fixed and heated while exposed to synchrotron radiation. at beamline BL9 at the synchrotron radiation source DELTA (TU Dortmund).[29, 30] Two-dimensional XRD patterns were recorded with a Pilatus 100 k detector and a sample-to-detector distance of 760 mm using a wavelength of 0.0816 nm and exposure times of 30 s. Differently elongated samples of vulcanized NR were placed in a custom made aluminum furnace and exposed to synchrotron radiation while the temperature was raised (accuracy ± 0.5 °C). The XRD patterns exhibit well oriented crystalline (120)- and (200)-reflections with parameters of the monoclinic unit-cell ($a$ = 1.246 nm, $b$ = 0.889 nm, $c$ = 0.81 nm, and $\beta$ = 92 °) reported by Bunn[31]. The intensities of Bragg reflections were obtained by numerical integration after background subtraction. Exemplarily, a plot of intensity of the (120)- and (200)-reflections of poly-isoprene crystals versus temperature of the latex-based NR sample strained to 760 % can be seen in Figure 1a. The measurements started at 35 °C which was the lowest adjustable temperature due to technical restrictions. As it can be seen the intensity decreases strongly in a range of 35 to 48 °C. This is the temperature range where we found typical trigger temperatures of SMNR.[17, 27, 28] Obviously, the melting of these crystals starts even at lower temperatures, which we were not able to address in this experiment. At 48 °C still a significant amount of crystals exists, but the curve shows a change of tendency. After that the crystals melt in a much broader temperature range and finally completely disappear at temperatures above 100 °C. We propose that the first crystals are the network-stabilizing crystals of SMNR which are responsible for the thermal trigger of the latter. The higher melting crystals, however, might be the directly strain-induced crystals. The temperature where both reflections disappear is considered as melting temperature of the most stable crystals under certain constrained conditions $T_{m,end}$.

Figure 1b (and Table 1) shows values for $T_{m,\,end}$ as function of strain for both SMNR networks. In this graph the melting temperature increases with greater strain. Both curves show asymptotical progressions against a network-specific maximal melting temperature $T_{m,end,max}$. This temperature is increasing with decreasing degree of cross-linking (DC), being $T_{m,end,max,Neotex}$ = 107.4 °C for DC = 0.2 % and $T_{m,end,max,SMR10}$ = 126.5 °C for DC = 0.1 %. The latter is the highest melting temperature of crystals in cross-linked natural rubber ever measured. So far the results reported by *Gent and Zhang*[32], who used a higher cross-linked NR (SMR 10 cross-linked with 1 % dicumyl peroxide, strained to 250 %) and found a $T_{m,\,end}$ of 55 °C, are in good agreement to these data.

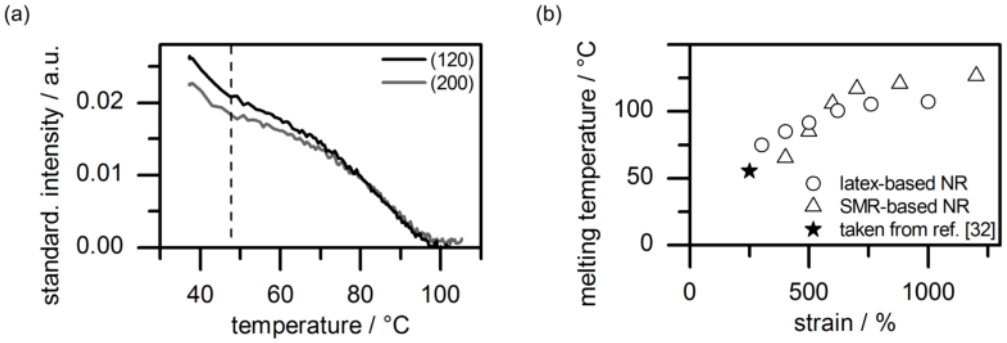


**Figure 1:** a) Plot of intensity for (120)- and (200)-reflections versus temperature of latex-based NR strained 760 %. The intensity of the (200)-reflection was multiplied by 3 to get a better comparison. b) Melting temperatures of SMR- and latex-based NR samples depending on different strains.

**Table 2:**. Obtained values of melting temperatures according different strains of vulcanized latex-based and SMR-based natural rubbers.

| latex–based NR | | SMR-based NR | |
|---|---|---|---|
| $\varepsilon$ / % | $T_{m,\,end}$ / °C | $\varepsilon$ / % | $T_{m,\,end}$ / °C |
| 300 | 74.8 | 400 | 65 |
| 400 | 84.7 | 500 | 84.7 |
| 500 | 91.4 | 600 | 106.1 |
| 620 | 100.5 | 700 | 116.7 |
| 760 | 105.3 | 880 | 120.8 |
| 1000 | 107.4 | 1200 | 126.5 |

The two different melting regimes of the polymer crystals might be explained with the model of *Fukahori*[33] which proposes a partially continuous cross-linked phase and a continuous uncross-linked phase in vulcanized natural rubber. According to this model we propose that strain-induced crystallization appears mainly in the cross-linked phase followed by thermal crystallization in the uncross-linked phase. The crystals formed in the cross-linked phase should be more sensitive to parallel stress then the crystals formed in the uncross-linked phase. This should then result in the two melting regimes

## Acknowledgement

The authors acknowledge the DELTA staff for providing synchrotron radiation. Moreover, we thank Continental Reifen Deutschland GmbH, in particular Dr. Fred Waldner and Dr. Tobias Ruckert, for supplying Standard Malaysian Rubber 10 as well as Weber & Schaer GmbH & Co. KG, especially Dr. Andreas Schuch, for providing non-vulcanized natural rubber latex. The research leading to these results has received funding from the Ministry of Innovation, Science and Research of North Rhine-Westphalia in the frame of CLIB-Graduate Cluster Industrial Biotechnology.

## References

[1] M. Behl, A. Lendlein, Materials Today 2007, 10, 20.
[2] J. Kunzelmann, T. Chung, P. T. Mather, C. Weder, Journal of Materials Chemistry 2008, 18, 1082.
[3] T Ikeda, J. Mamiya, Y. L. Yu, Angew. Chem. Intern. Ed. 2007, 46, 506.
[4] C. Liu, H. Qin, P. T. Mather, Journal of Materials Chemistry 2007, 17, 1543.
[5] K. Otsuka, C. M. Wayman, Shape Memory Materials, Cambridge University Press, New York, 1998.
[6] A. Lendlein, S. Kelch, Angew. Chem. Intern. Ed. 2002, 41, 2034.
[7] P. T. Mather, X. Luo, I. A. Rousseau, Annual Review of Material Research 2009, 39, 445.
[8] A. Alteheld, Y. Feng, S. Kelch, A. Lendlein, Angew. Chem. Int. Ed. 2005, 44, 1188.
[9] A. Lendlein, R. Langer, Science 2002, 296, 1673.
[10] P. Miaudet, A. Derre, M. Maugey, C. Zakri, P. M. Piccione, R. Inoubli, P. Poulin, Science 2007, 318, 1294.
[11] J. Li, T. Xie, Macromolecules 2011, 44, 175.
[12] T. Xie, Nature 2010, 464, 267.
[13] J. Cui, K. Kratz, A. Lendlein, Smart Mater. Struct. 2010, 19, 65019.
[14] J. Cui, K. Kratz, M. Heuchel, B. Hiebl, A. Lendlein, Polym. Adv. Technol. 2011, 22, 180.
[15] T. Xie, K. A. Page, S. A. Eastman, Adv. Funct. Mater. 2011, 21, 2057.
[16] K. Kratz, S. A. Madbouly, W. Wagermaier, A. Lendlein, Adv. Mater. 2011, 23, 4058.
[17] F. Katzenberg, B. Heuwers, J.C. Tiller, Adv. Mater. 2011, 23, 1909.
[18] W. Voit, T. Ware, R. R. Dasari; P. Smith, L. Danz, D. Simon, S. Barlow, S. R. Marder, K. Gall, Adv. Funct. Mater. 2010, 20, 162.
[19] D. J. Maitland, M. F. Metzger, D. Schumann, A. Lee, T. S. Wilson, Lasers Surg. Med. 2002, 30, 1.
[20] A. Lendlein, H. Y. Jiang, O. Junger, R. Langer, Nature 2005, 434, 879.
[21] C. M. Yakacki, T. D. Nguyen, R. Likos, R. Lamell, D. Guigou, K. Gall, Polymer 2011, 52, 4947.
[22] R. Mohr, K. Kratz, T. Weigel, M. Lucka-Gabor, M. Moneke, A. Lendlein, Proc. Natl. Acad. Sci. USA 2006, 103, 3540.
[23] Z. He, N. Satarkar, T. Xie, Y.-T. Cheng, J. Z. Hilt, Adv. Mater. 2011, 23, 3192.
[24] J. W. Cho, J. W. Kim, Y. C. Jung, N. S. Goo, Macrom. Rapid Commun. 2005, 26, 412.
[25] J. Li, J. A. Viveros, M. H. Wrue, M. Anthamatten, Adv. Mater. 2007, 19, 2851.
[26] T. Xie, Polymer 2011, 52, 4985.
[27] B. Heuwers, D. Quitmann, F. Katzenberg, J. C. Tiller, Macromolecular Rapid Communications 2012, 33, 1517.
[28] B. Heuwers, D. Quitmann, R. Hoeher, F. M. Reinders, S. Tiemeyer, C. Sternemann, M. Tolan, F. Katzenberg, J. C. Tiller, Marcom. Rapid Commun. 2012, DOI: 10.1002/marc.201200594.
[29] C. Krywka, M. Paulus, C. Sternemann, M. Volmer, A. Remhof, G. Nowak, A. Nefedov, B. Pöter, M. Spiegel, M. Tolan, Journal of Synchrotron Radiation 2006, 13, 8.
[30] C. Krywka, C. Sternemann, M. Paulus, N. Javid, R. Winter, A. Al-Sawalmih, S. B. Yi, D. Raabe, M. Tolan, Jounral of Synchrotron Radiation 2007, 14, 244.
[31] C. W. Bunn, Proc. R. Soc. A 1942, 180, 40.
[32] A. N. Gent, L.-Q. Zhang, Rubber Chemistry and Technology 2002, 75, 923.
[33] Y. Fukahori, Polymer 2010, 51, 1621.

# Decarburization in HVOF-sprayed WC-Co and WC-FeCrAl coatings

***B. Hussong***
*Institute of Materials Engineering, Dortmund, Germany*
**E-mail: birger.hussong@udo.edu*

## Introduction

Decarburization of WC based wear resistant coatings is one of the mayor problems during thermal spraying of these materials. Most scientists concentrate on mechanical properties and wear experiments to evaluate the quality of thermal spray coatings [1-3] but for understanding the reasons for differences in wear performance it is also necessary to investigate phase transformations and decarburization. When decarburization inside of Cermets occurs, it usually goes along with dissolution of the WC into the metallic matrix, which is usually Co or other ductile material. This effect is caused by particle overheating, which can result from increased energy input to the process by high combustion gas flow or a long dwell time of the particles inside the flame at large stand-off distances or long acceleration barrels. The conversion of WC into $W_2C$ as well as the dissolution of W into the metal matrix results into increased brittleness of the coatings, which can lead to spallation or delamination.
There are several ways to deduce decarburization from the coating result. The easiest one is by investigating the matrix and carbides in the SEM in the backscatter electron mode. Materials containing atoms with high mass appear light in this SEM mode, whereas materials of atoms with less atomic mass appear darker. Therefore the dissolution of W into the metal matrix can be observed due to the increased brightness of the matrix. Another indicator is the sharpness of the carbide edges. The initial state of the carbides is an angular sharply edged morphology. When dissolution of carbides takes place these edges are usually the first places for the WC to dissolve and diffuse into the matrix.
Another way to detect the loss of carbon in the carbides or the increasing of W in the matrix is the EDX analysis [4], which can detect and quantify the characteristic X-ray emission of atoms when exposed to an electron beam. The disadvantage of this method is, that lighter atoms like Carbon are close to detection capability of such systems and thus the quantification is not very precise. Also the lateral resolution of this method is not small enough, because the carbides are smaller than the area of X-ray response. Additionally the information which is provided is only about the appearing elements. There is no information about the phases in the material.
However, these methods are very indirect and do not directly give proof on the distinct phases which develop during the process.
Another and much more precise way to control decarburization and WC dissolution is the XRD analysis [5]. This analysis gives proof on the different phases, which occur inside the sample material, and thus gives reliable information about phase transformations caused by the spraying process.
This method works with X-ray diffraction on crystal plains. Thus it has some difficulties in detecting amorphous phases. Unfortunately during thermal spraying the metal matrix of the powders usually solidifies in an amorphous state due to the extremely high cooling rate.
Anyway, in this work XRD analysis has been performed on a set of 30 samples, sprayed with different parameters on an HVOF spraying system. The aim of the investigation was a quantification of influence of the parameters on the phase transformations in the process. As powder material a new Iron-based matrix material was tested (Fig. 1). The chemical composition of this powder is given in table 1.

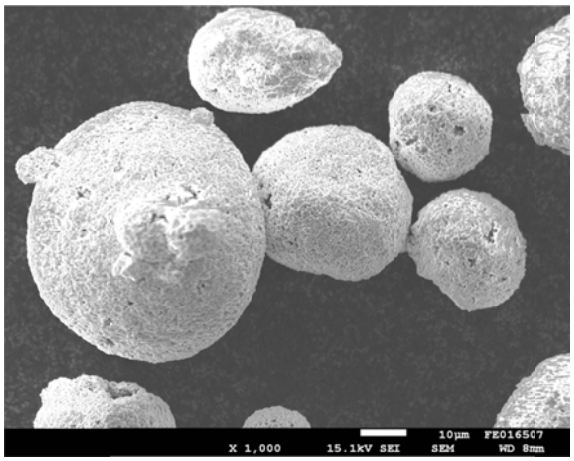


*Figure 1: SEM-image of utilized WC-FeCrAl powder from H.C.Starck*

*Table 1: Powder chemical composition [wt.-%]*

| W | C | Fe | Cr | Al |
|---|---|---|---|---|
| 79.58 | 5.48 | 11.07 | 2.94 | 0,93 |

## Results and Discussion

The XRD graphs of the feedstock material and the sprayed coatings already reveal a remarkable change in the material composition (Fig. 2). While the feedstock powder contains a significant amount of Cr, Fe and AlFe in crystalline form, the sprayed material does not show any clear peaks of Cr, Fe or AlFe. Instead it has a wide amorphous background around the angles, where these peaks were before spraying. This indicates

a change from crystalline to amorphous structure during thermal spray process. The graphs of the coatings also show small peaks around 40° and at 53°, 62° and 70°. These could be identified as mostly crystalline $W_2C$ and delta-$Fe_2O_3$. These phases have not been found in the powder before and thus can only result from heat in the spraying process.

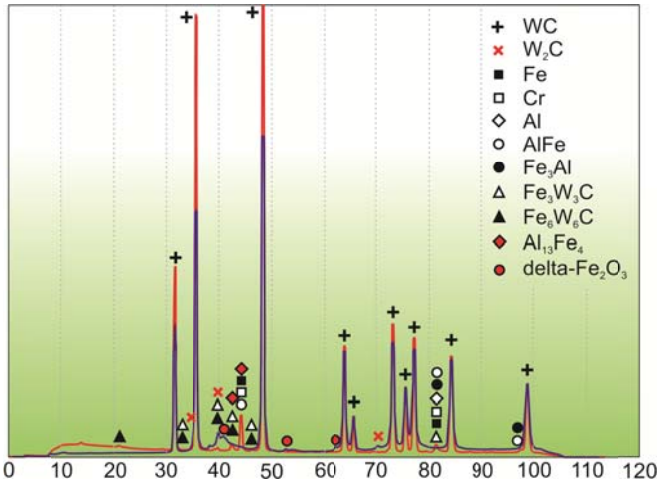


*Figure 2: X-ray diffractograms of feedstock powder (red) and as sprayed coatings (blue)*

Other phases like $Fe_3W_3C$, $Fe_6W_6C$ and $Al_{13}Fe_4$, which could be observed in the feedstock material, also disappear in the graph after thermal spraying. Due to the position of the corresponding peaks it cannot clearly be said, if these phases have been dissolved into other combinations, or if the peaks have become more amorphous and thus might be adumbrated by the peaks of the delta-$Fe_2O_3$ and $W_2C$.

Assuming that these phase transformations have taken place, there must be some carbide dissolution visible in the metal matrix material. To test this, a set of single splat deposition experiments were conducted, to see, whether this carbide dissolution was detectable or not.

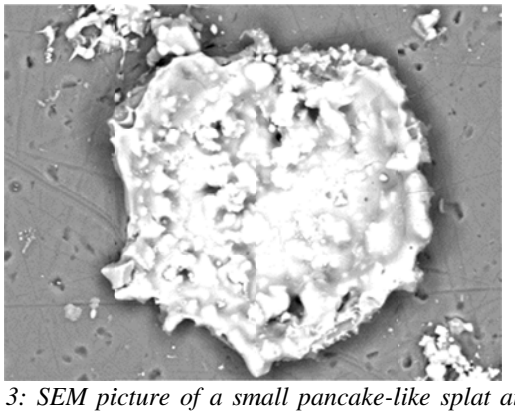

*Figure 3: SEM picture of a small pancake-like splat at back scattering electron mode. The carbides show a high grade of dissolution of W into the matrix material.*

Fig. 3 shows a backscatter electron SEM-picture of one single splat deposited with a set of spray parameters equal to those in the coating depositions. It can be seen that there has been severe W diffusion into the metal matrix. The bright backscatter signals from the matrix do not even allow to distinguish between carbides and matrix material. This confirms the result of the XRD analysis, which proposes significant decarburization and reduction of the pure WC content.

## Summary

Summarizing the findings of this investigation it can be said that thermal spraying of WC-FeCrAl Cermets causes significant phase transformations in the matrix material as well as in the WC itself. All crystalline phases like Fe, Al, Cr, AlCr, $Fe_3Al$ and $Al_{13}$ $Fe_4$ have changed to amorphous phases. Complex phases of $Fe_3W_3C$ or $Fe_6W_6C$, which could be detected in the feedstock powder have either been dissolved or changed into amorphous state, too. A small grade of oxidization after spraying is revealed due to the detection of crystalline delta-$Fe_2O_3$.

## Acknowledgement

The authors gratefully acknowledge the financial support of the DFG (German Science Foundation) within the collaborative research center SFB 823 B1 for the powder materials and funding of the spraying experiments. Special thanks to the DELTA-team at TU-Dortmund, who enabled us to use the Beamline 9 at DELTA for XRD measurements.

## References

1. T. Sahraoui, S. Guessasma, M. Jeridane, et al., HVOF sprayed WC-Co coatings: Microstructure, mechanical properties and friction moment prediction, *Materials & Design*, 2010, **31**(3), p 1431-1437

2. D.A. Stewart, P.H. Shipway, and D.G. McCartney, Abrasive wear behavior of conventional and nanocomposite HVOF-sprayed WC-Co coatings, *Wear,* 1999, **225-229**(2), p 789-798

3. J. He, and J.M. Schoenung, A review on nanostructured WC-Co coatings, *Surface & Coatings Technol.,* 2002, **157**, p 72-79

4. I.T. Baumann, Hochverschleißfeste und konturnahe Werkzeugoberflächen durch Hochgeschwindigkeits-flammspritzverfahren, *dissertation*, Dortmund 2012

5. W. Tillmann, E. Vogli, I. Baumann, G. Matthäus, Influence oft he HVOF gas composition on the thermal spraying of WC-Co submicron powders (-8+1) to produce superfine structured cermet coatings, *DVS publisher (Hg.): Proc. ITSC 2008, Maastricht, Netherlands*

**Institute of Physics, University of Siegen**,

***S. Kamran* ,*U.Pietsch and S.Grigorian***

# Enhancement of Field Effect Mobility due to Structural ordering in (Poly3-hexylthiophene) Films Transistors by Dip-coating Technique

The Poly (3-hexlythiophene) (P3HT) is one of the most successfully studied conducting polymers. Due to anisotropy of initial molecular structure, and proceeding conditions crystallinity and orientation of the molecules in thin films can strongly affect the performances of organic field effect transistors (OFETs). One of the greatest challenges is to achieve the ultimate control over film morphology and the degree of crystallinity. The current goal is to understand conditions when P3HT thin films are aligned in particular direction to improve performance in field effect mobility [1].

The (RR-P3HT) thin films were deposited on glass substrate by dip-coating technique with 0.008mm/s withdrawal speeds using 1 mg/ml solution concentration. MAR Image plate detectors with 0.0001° resolution was used to detect scattering using grazing incidence X-ray diffraction (GIXD) setup. Experiment was performed under 15 Kev and at the grazing angle($\alpha_i = 0.11°$). Alignment of the sample and the reflectivity measurement were done by point detector. To understand a role of the thermal treatment x-ray patterns were measured under different fixed annealing temperatures 100,180 and 220°C by Anton Parr (DHS900) heating stage.

The influence of the dip-coating speeds on the P3HT films is a following as the withdrawals speeds decreases the crystallinity and the chain orientation is improved. This fact can be explained that a number of edge-on oriented crystallites increases by decreasing of the withdrawal speeds. In order to investigate the annealing effect on P3HT thin film, fabricated the thin films were in-situ annealed at 100,180 and 220°C for 45min and cooled down to room temperature. The thermally annealed films exhibit higher degree of crystallinity and the chain ordering [2, 3, 4]. Afterwards the structural properties were investigated parallel and perpendicular to the dipping directions. The 2D patterns of the dip-coated films with withdrawal speed of 0.008 mm/s (annealed at 180°C) measured in the perpendicular and parallel to the dipping direction are shown in Fig 1.

These relatively sharp and intense (h00) spots along Q (out-of-plane direction) are referring to the domination of edge-on oriented crystallites fig 1 (top). In contrast, 2D pattern in the parallel to the dipping direction shown in Fig.1 (bottom) reveals numerous but less intense (h00) reflections

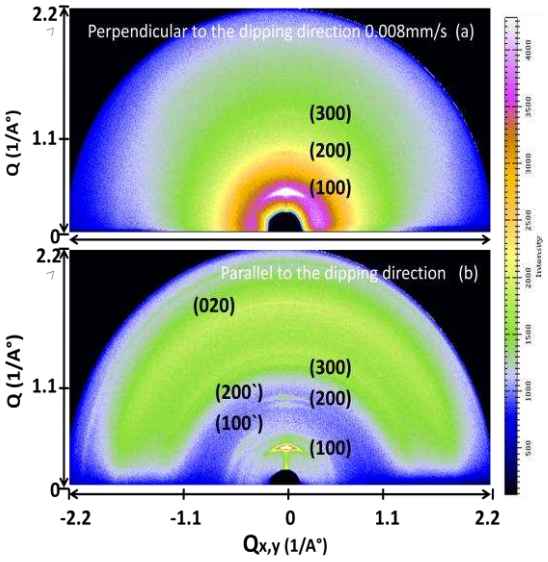


Figure 1: GIXD 2D patterns in the perpendicular (a) and parallel (b) to the dipping direction

## Conclusion:-

The fabricated dip-coated transistor shows direct correlation with the structural properties. In the device characterization the OFETs that were dipped perpendicular (with respect to conducting channel) and annealed reflects better performance in the field effect mobility compare to parallel to dip-direction. In-addition, the mobility is also increased as the withdrawal speeds decreases.


1. Muccini, M., A bright future for organic field-effect transistors. Nature materials, 2006. **5**(8): p. 605-613
2. Joshi, S., et al., Bimodal temperature behavior of structure and mobility in high molecular weight P3HT thin films. Macromolecules, 2009. **42**(13): p.4651-4660.
3. Salammal Shabi, T., et al., Enhancement in crystallinity of poly (3-hexylthiophene) films prepared by low-temperature drop casting. Journal of Applied Polymer Science.
4. Sirringhaus, H., et al., Two dimensional charges transport in self organized high-mobility conjugated polymers. Nature, 1999. **401**(6754).

# Phase transitions of polymers under confinement in the silicate-based, intercalated polymer nanocomposites

Adam Kiersnowski[1,2*], Markus Mezger[1*], Małgorzata Gazińska[2], Binyang Hou[2,3], Christian Sternemann[4], Michael Paulus[4]

[1] Max Planck Institute for Polymer Research, Ackermannweg 10, 55128 Mainz, Germany; [2] Polymer Engineering and Technology Division, Wroclaw University of Technology, Wybrzeze Wyspianskiego 27, 50-370 Wroclaw, Poland; [3] European Synchrotron Radiation Facility, 6 Rue Jules Horowitz, BP 220 38043 Grenoble Cedex 9, France; [4] Institute of Physics, University of Dortmund, 44221 Dortmund, Germany

[*]correspondence: adam.kiersnowski@mpip-mainz.mpg.de; mezger@mpip-mainz.mpg.de

The aim of this project was to analyze thermally induced variation in the basal spacing of the layered silicates intercalated with polymer macromolecules. To achieve the goal the organoclays based on the synthetic fluoromica (SOMASIF ME100) ion-exchanged with dodecyltrimethylammonium (1C12w), hexadecyltrimethylammonium (1C16w) and octadecyltrimethylammonium (1C18w) bromides were analyzed. The ion-exchange processes leading to formation of the organoclays were described elsewhere [1]. The organoclays were then used as the precursors for the polymer nanocomposites based on poly(ε-caprolactone) (PCL), isotactic polypropylene (i-PP) and poly(vinylidene fluoride) (PVDF). PCL nanocomposites were synthesized by *in-situ* intercalative polymerization [2] while i-PP and PVDF-based systems were obtained by a melt-blending in the twin-screw extruder [3]. The time-resolved SAXS measurements were carried out at the BL9 beamline at DELTA synchrotron facility (TU Dortmund). The combination of the beam energy (E=10 keV;. λ=1.2398 Å) and the beamline setup (MAR345 detector at the distance of 108 cm from the sample position) enabled recording scattered intensity within the q-vector range of 0.024 to 0.524 $Å^{-1}$ ($q=\lambda^{-1}4\pi sin\theta$). The temperature (T) of samples changed within 30-120°C and the ramping (heating/cooling: 5K/min) were controlled by the LakeShore 340 controller connected to a custom-build (MPIP-Mainz) air-cooled stage. The optimal exposure time for the chosen conditions was found 10s for a single frame.

In order to obtain a full structural picture of the analyzed materials we first performed measurements of the organoclays alone. Recorded sets of SAXS patterns that were converted to intensity maps in the way as shown in Fig. 1 a. These maps were then analyzed along the logged temperature profiles. The temperature program included heating from 30°C to 120°C, annealing at 120°C for 10 min, cooling down to 30°C followed by thermal equilibration at 30°C and finally reheating to 120°C.

A common feature of the ana-

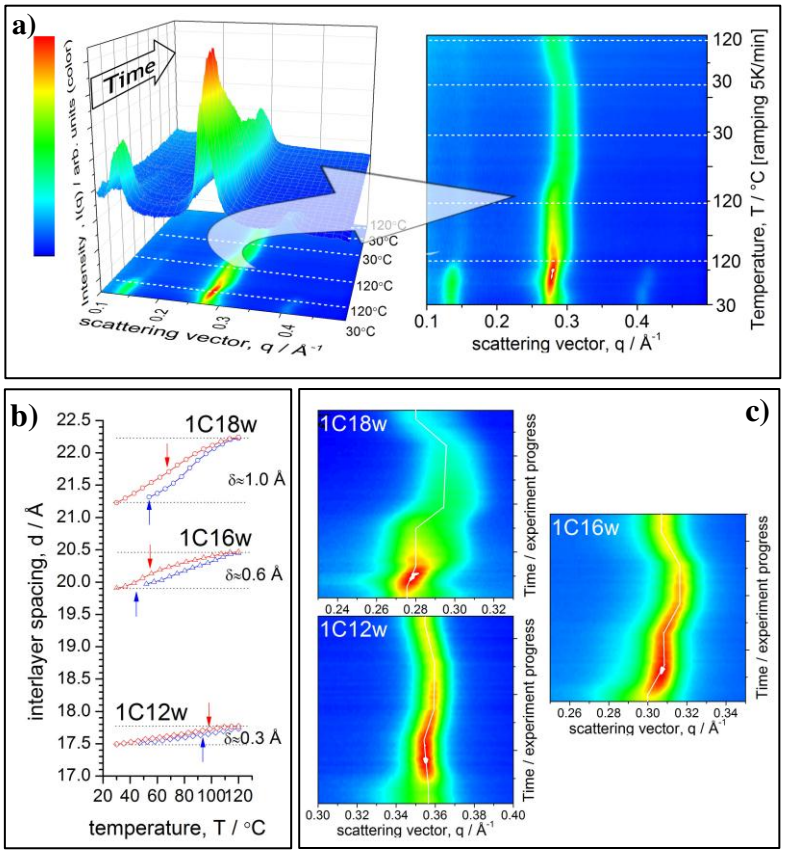


**Figure 1.** (a) Exemplary experimental data recorded for M1C18w system and the way to derive intensity maps out of the set of time-resolved SAXS patterns (a). Variation in the interlayer distance upon heating (red) and cooling (blue) of the different alkylammonium-intercalated fluoromica complexes (b) as calcu-lated from the main peak position in the intensity maps of the complexes (c). Arrows in Fig b indicated inflection points recorded by DSC.

lyzed organoclays is the irreversible decrease in the basal spacing observed during the first heating cycle and the subsequent annealing at 120°C. In the case of 1C18 and 1C12 this change approximates 0.5 Å while for 1C12 it is much smaller, though measurable. This shift in the d-spacing is accompanied by an increase in the intensity of the corresponding peak (Fig. 1c). A comparison of these results with findings from FTIR measurements leads to the conclusion that these changes stem from the release of water molecules entrapped both in the galleries of the silicate as well as adsorbed at the outer surfaces the organoclays' stacks. Rearrangement of surfactant molecules accompanying water release from the galleries causes a transient increase in the electron contrast between organic and inorganic layers thus leading to strengthening the diffraction peaks coupled with the basal spacing of the silicate. Further cycles of heating and cooling are followed by fully thermally reversible changes in the interlayer spacing (Fig. 1b). Their magnitudes averaged over the whole temperature range were found to be 0.3, 0.6 and 1.0 Å for 1C12w, 1C16w and 1C18w respectively. This means that under the experimental conditions taken here the average linear expansion coefficient of the organoclays in the direction normal to layers ranges from $2\times10^{-4}$ to $5\times10^{-4}$ $K^{-1}$. Depending on ammonium molecules intercalated in the organoclay, the changes in d-spacing of organoclays reveal certain nonlinearity on heating (1C16w) or cooling (1C18w) (Fig. 1 b, c). Similarly as the authors of previous scientific reports [4,5] we clarified this issue by additional DSC, FTIR and NMR experiments. By combining results from these techniques with our SAXS data we were able to correlate the changes observed in the second cycle with so called γ-gauche effect and to provide a better model for the changes in the d-spacing of organoclays in comparison to the usual scheme of solid- to liquid like transitions [4,5].

Similarly, SAXS measurements were performed also for the intercalated nanocomposites. Generally, in the case of nanocomposites the changes in the interlayer distance were dominated by effects induced by the intercalated polymer chains. For PCL/1C16, i-PP/1C18 and PVDF/1C18 nanocomposites it was found that upon heating around melting points of the polymers the d-spacing of the organoclays rapidly increases by approx. 1.5 Å. This observation coupled with kinks in DSC traces allows associating the humps in d-spacing plots with ordering resembling the crystallization of polymer chains within the galleries of the silicates. Interestingly, the behavior of PCL/1C18 system is significantly different from all the described above (Fig. 2). After erasing the thermal history, cooling the system first causes a significant increase in the interlayer spacing of the 1C18 organoclay followed by a sharp decrease at 55°C (m.p.$_{PCL}\approx$ 60°C). It is worth noticing here that no hysteresis typical for crystallization and melting of semicrystalline polymers was observed for processes occurring in the galleries of the silicate (Fig. 2b). Analysis of the SAXS data as well as DSC and preliminary spectroscopic results has lead us to the conclusion that these phenomena are caused by not only ordering and disordering of macromolecules inside the galleries. Rapid changes at higher temperatures seem to be a result of mixing and demixing processes between PCL and hydrocarbon chains of the C18 compound.

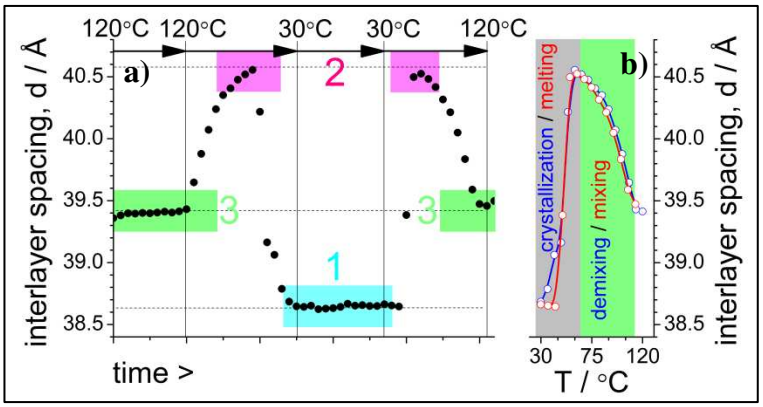


**Figure 2.** (a) Variation in the d-spacing of the organoclay particles recorded for PCL/1C18 system with progress of the measurement and temperature. Colored boxes and numbers indicate different physical states of the intercalated compounds: 1 (lt blue) phase-separated system of ordered PCL macromolecules and aliphatic chains of C18 molecules in the solid-like state; 2 (pink) phase-separated liquid-liquid system of PCL and the amphiphilic compound; 3 miscible, two-component system. (b) The themperature-induced changes in the d-spacing recorded on heating (red symbols) and cooling (blue symbols)

**Acknowledgement:** The access to the BL9 beamline granted by a scientific council of DELTA synchrotron facility is gratefully acknowledged. Adam Kiersnowski acknowledges the financial support from the Marie Curie Intra European Fellowship (PIEF-GA-2009-253521) granted within the 7th EU Framework Program. The authors thank to Peter Reichert and Michael Bach from Max Planck Institute for Polymer Research for their help in solving technical problems.

**References:** [1] A. Kiersnowski, M. Trelińska-Wlaźlak, M. Gazińska, J. Pigłowski; *Polimery* 56, **2011**, 671 [2] A. Kiersnowski, J.S. Gutmann, J. Pigłowski; *J. Polym. Sci. B – Polymer Physics* 45, **2007**, 2350; [3] S.S. Ray, M. Okamoto *Prog. Polym. Sci.* 28, **2003**, 1539; [4] R.A. Vaia, R.K. Teukolsky, E.P. Giannelis *Chem. Mater.* 6, **1994**, 1017; [5] H. Heinz, R.A. Vaia, B.L. Farmer *Langmuir* 24, **2008**, 3727

# Temperature treatment of protein layers at the solid-liquid interface in two different environments

Irena Kiesel, Michael Paulus, Julia Nase, Sebastian Tiemeyer, Christian Sternemann, Metin Tolan

Fakultät Physik/DELTA, Technische Universität Dortmund, 44227 Dortmund, Germany

Proteins at solid/liquid interfaces play a key role in technical, biomedical, and food processing applications [1–10]. The interaction of bacteria and cells with surfaces is influenced by adsorbed proteins. They are crucial for e.g. the acceptance of implants and the functionality of biosensors and can lose their functionality when denatured by e.g. heat treatment.

In our experiment we have investigated the denaturation process induced by increasing temperature in two different environments. Until now, most denaturation experiments were performed using protein solutions. However, a solution, which represents a protein reservoir, enables further protein adsorption during the denaturation process. Therefore, we have placed hydrophilised silicon wafers with a natural oxide layer in a protein buffer solution until a protein layer was accrued. The used model proteins are lysozyme, ribonuclease A (RNase A), and bovine serum albumin (BSA). In-situ x-ray reflectivity measurements were performed on these protein coated silicon wafers in pure phosphate buffer solution and in protein buffer solution. X-ray reflectivities at different temperatures up to 90°C were recorded using the 27 keV x-ray reflectivity setup of beamline BL9 at the synchrotron source DELTA [11].

The denaturation process was investigated by analyzing the (layer) electron density profiles perpendicular to the surface, obtained from the reflectivities. Information on structural changes of the protein film induced by temperature was analysed (Fig. 1 and 2). Figure 1 shows electron density profiles of samples in pure buffer solution. For lysozyme (a) and RNase A (b), a decreasing electron density for increasing temperature was observed, indicating desorption of proteins. For BSA (c), the electron density did not decrease continuously. Between 30°C and 40°C, a jump of the electron density to lower value is observed.

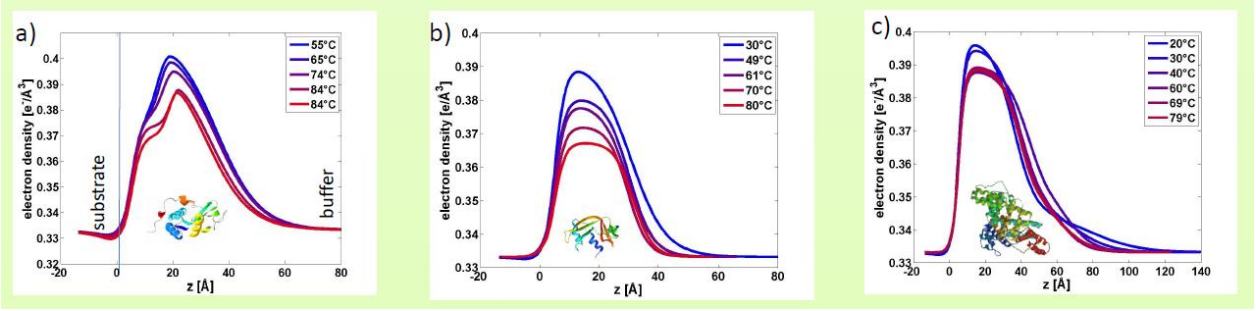


Fig. 1: Electron density profiles of a) lysozyme b) RNase A and c) BSA layer in pure buffer solution during heat treatment. The electron density profile of the substrate is subtracted.

The electron density profiles of the protein layers in protein solution are shown in figure 2. The lysozyme layer (a) grows with increasing temperature. Moreover, the film continues to grow with time at 80°C. RNase A (b) and BSA (c) show also increasing layer thicknesses with increasing temperature, but, especially for BSA, the growth is much smaller than for lysozyme. The film growth indicates further protein adsorption from solution.

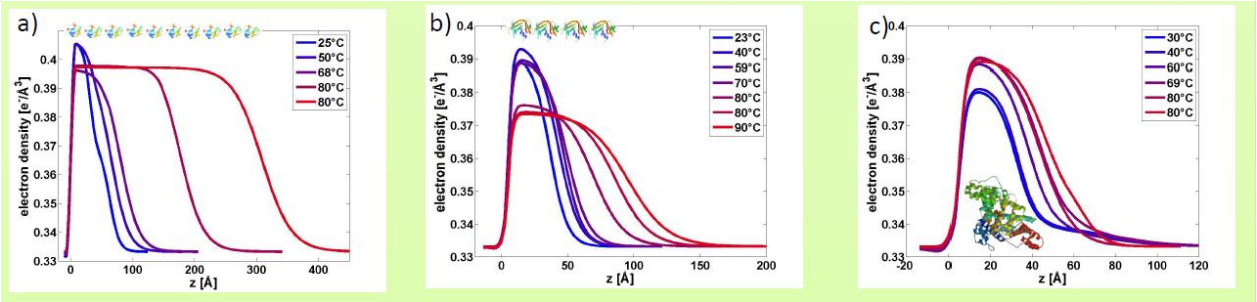


Fig. 2: Electron density profiles of a) lysozyme b) RNaseA and c) BSA layer protein solution (1mg/mL) during heat treatment. The electron density profile of the substrate is subtracted.

In summary, we have observed that in pure buffer solution, the proteins desorb with increasing temperature, whereas temperature treatment of protein layers in protein solution results in thicker protein layers and can be explained by additional protein adsorption. These trends are similar for lysozyme and RNase A and weaker for BSA. This result might be caused by the different size, charge, or conformational stability of the proteins. Furthermore, we observed a time dependent layer growth of the heated samples in protein solution. Thus, further protein adsorption with ongoing time is supposed. On the time scale of our experiment we did not see saturation of this adsorption process.


[1] A. Baszkin and W. Norde (1999); Phys. Chem. of Biol. Interf.; CRC Press; 1 ed.; ISBN 0824775813
[2] J. L. Brash, T.A. Horbett (1987); Prot. at interf., 343: pp. 1-33
[3] F. Evers et al. (2008); Langmuir: Surf. and Coll.; 24 (18): pp. 10.216_10.221; doi:10.1021/la801642s
[4] W. Norde, J. Lyklema ; J. Biomat. Sci. Polym. (1991), 2(3): pp. 183-202
[5] G. Jackler et al. (2002); Langmuir; 18 (17): pp. 6565_6570; doi:10.1021/la025605i
[6] J. Lu et al. (1998); J. of Coll. and Int. Sci.; 206 (1): pp. 212_223; ISSN 0021-9797; doi: 10.1006/jcis.1998.5680
[7] P. Déjardin, (2006); Prot. at Sol.-Liq. Interf.; Springer Berlin Heidelberg; ISBN 978-3-540-32657-1
[9] B. Kasemo (2002); Surf. Sci.; 500 (1-3): pp. 656-677, doi: 10.1016/S0039-6028(01)01809-X
[10] M. Tirrell et al. (2002); Surf. Sci.; 500 (1-3): pp. 61-83; doi: 10.1016/S0039-6028(01)01548-5
[11] M. Paulus et al. (2008); J. Synch. Rad.; 15 (6): pp. 600-605; doi: 10.1107/S0909049508026745



Acknowledgement:
We would like to thank the DELTA machine group for providing synchrotron radiation and technical support.
I. Kiesel acknowledges the BMBF (project 05K10 PEC) and S. Tiemeyer thanks the NRW Forschungsschule 'Forschung mit Synchrotronstrahlung in der Nano- und Biowissenschaften' for financial support.

# Fast x-ray reflectivities

J. Nase, M. Paulus, C. Sternemann, S. Tiemeyer, F. Wirkert, M. Tolan
Fakultät Physik/DELTA, Technische Universität Dortmund, Maria-Goeppert-Mayer-Str.2, 44227 Dortmund, Germany

The x-ray reflectivity technique is a powerful tool to investigate the structure of extremly thin films. Especially the use of high energy photons gives the opportunity to analyze formation processes at buried interfaces such as solid – liquid or liquid - liquid interfaces [1-3]. Using the well-known Parratt algorithm [4] for data analysis, one obtains the laterally averaged vertical electron density profile of the sample including interfacial roughnesses, electron densities and layer thicknesses.

In an x-ray reflectivity experiment, the intensity of a reflected x-ray beam is measured as a function of the wave vector transfer $q_z=4\pi/\lambda \sin(\vartheta)$ perpendicular to the samples surface, where λ is the wavelength of the radiation and $\vartheta$ the scattering angle with respect to the sample surface. In standard set-up, the data collection time for a single reflectivity scan can take a few minutes up to several hours, depending on the photon flux and the speed of motor movement. During a reflectivity scan, the sample system must be stable, since dynamical processes, which are not taken into account in the data treatment, cause artifacts in the resulting electron density profile. For example, figure 1 shows the reflectivity of a simple one layer system, where only the layer density is growing with time (see inset of figure 1). This changing electron density causes a very complex shape of the reflectivity curve. Applying a static electron density profile for data analysis leads to a complete misinterpretation of the experiment.

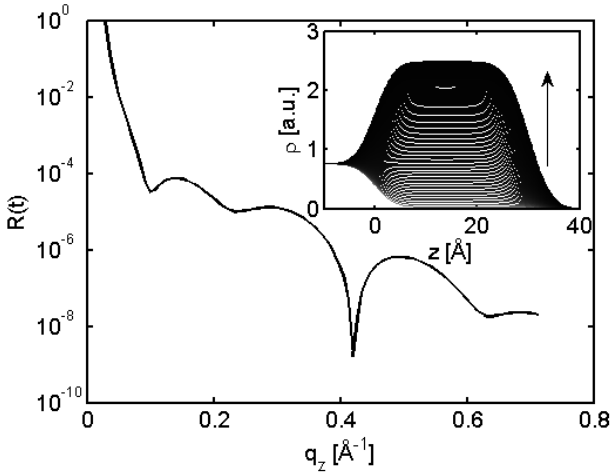


**Figure 1: Time dependent x-ray reflectivity of a one layer system with increasing electron density. The inset shows the development of the layer with time. The arrow indicates the growth direction.**

In order to avoid the misinterpretation of the data, one needs to reduce the measuring time such that the system appears quasi static. However, due to sufficient data statistics, this is not applicable for every system. An alternative is the use of a time dependent electron density profile for data analysis, which provides a time dependent layer thickness, roughness and electron density for every data point within a reflectivity scan. At beamline BL9, a proof of

principle experiment analyzing the time dependent adsorption of proteins (lysozyme) at the solid – liquid interface was performed. While the adsorption process of the proteins takes between 5 and 10 minutes, the fast x-ray reflectivity set up we report on allows recording one reflectivity within one minute. Figure 2, left shows the resulting reflectivity curves. Small changes in the region around $q_z$=0.1 Å$^{-1}$ are visible. On the right side of figure 2, simulated x-ray reflectivities are shown. Each reflectivity was calculated using a time dependent electron density of the adsorbed protein layer, according to the time evolution shown in the inset of figure 2, right. A good qualitative agreement between experiment and simulation was obtained. However, the data analysis is still in progress.

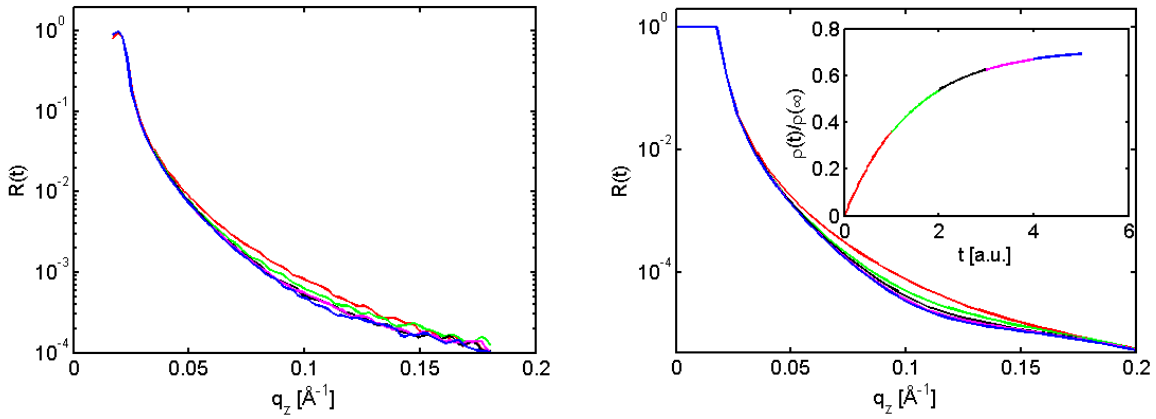


**Figure 2: Left: Time dependent x-ray reflectivities of the silicon – liquid interface during the adsorption of proteins at the interface. Right: Simulation of a set of time dependent reflectivities using a layer electron density evolution as plotted in the inset.**

We would like to thank the DELTA machine group for providing synchrotron radiation and for technical support.

[1] M. Mezger, F. Sedlmeier, D. Horinek, H. Reichert, D. Pontoni, H. Dosch, Journal of the American Chemical Society (JACS) 132, 6735-5741 (2010). [2] L. Boewer, J. Nase, M. Paulus, F. Lehmkühler, S. Tiemeyer, S. Holz, D. Pontoni, and M. Tolan, The Journal of Physical Chemistry **116** (15), 8548–8553 (2012). [3] M. Paulus, D. Lietz, C. Sternemann, K. Shokuie, M. Tolan, C. Czeslik, and R. Winter, Journal of Synchrotron Radiation **15**, 600-605, (2008). [4] L. G. Parratt Phys. Rev. 95, 359 (1954).

# The interface between a solid and supercritical $CO_2$

J. Nase*, M. Paulus, S. Holz**, S. Tiemeyer, F. Wirkert, T. Brenner, M. Tolan

Fakultät Physik/DELTA, TU Dortmund, Maria-Goeppert-Mayer-Str. 2, 44227 Dortmund.
** current address: ISF, TU Dortmund, Baroper Straße 301, 44227 Dortmund.

*email: julia.nase@tu-dortmund.de

## *Introduction*

Adsorption at interfaces is critical for many processes in nature, e. g. for the formation of gas hydrates, catalysis, enzymatic reactions, or industrial applications like filtering or water purification. The formation of an adsorption layer enhances the gas offer significantly and is thus of importance for transport and exchange processes at membranes and interfaces in nature. More than 100 models have been established to describe the various types of adsorption isotherms. Supercritical adsorption, however, is far less understood, though this phenomenon has been known for some time now [1]. It has tremendous importance in industrial applications like high pressure gas storage systems, Supercritical Fluid Chromatography (SFC), and polymer processing. However, the solid-fluid interface with a possible restructuration of the supercritical molecules has never been directly measured.

## *Setup*

Experiments were performed at beamline BL9 of DELTA at a photon energy of 27 keV. The setup consisted in a high pressure cell that can sustain gas pressures up to 80 bar and that was described in detail before [2]. The temperature was controlled via a water cooling circuit and a heating foil. Pressure and temperature in the cell were monitored during the experiments. The cell was connected to a bottle with liquid $CO_2$ of high purity.

## *Adsorption theory*

Many models have been established to describe adsorption. The adsorption of gas molecules on liquid or solid surfaces was shown to follow a Frenkel-Halsey-Hill isotherm [3]. It is obtained from a minimization of the free energy and describes the thickness *d* of the adsorption layer as a function of the pressure. *d* diverges when the condensation pressure at the corresponding temperature is reached. Adsorption in the supercritical regime has mainly been measured by gravimetric and volumetric methods. The amount of adsorbed molecules, in general in the order of a monolayer, can be described by several equations, one example being the Langmuir-Freundlich isotherm [1]. In literature, the near-critical region with a temperature range between $T_C$ and $T_C$ + 10 K is distinguished from the supercritical region, which begins from $T_C$ + 10 K.

## *Sample system and experiments*

We investigated the adsorption of $CO_2$ on a silicon substrate with dimensions of 19 x 19 $mm^2$. $CO_2$ has a critical temperature of 31 °C and a critical pressure of 73 bar. Below that temperature, the gas condenses if the pressure is increased above a certain value, visible from a jump in the density. Above $T_C$, the gas does not condense, and the density increases as a monotonous function, see Figure 1 (Data from [4]). Gaseous and liquid states are not defined, the fluid is supercritical.

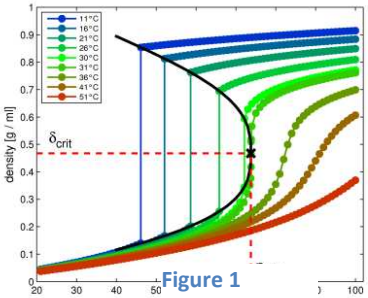

Figure 1

Experiments were performed in the following way. The temperature was set

to a certain value below $T_C$. When equilibrium was reached, a certain amount of gas was allowed to flow into the cell until a certain pressure was reached and the corresponding amount of $CO_2$ molecules condensed at the surface. Reflectivity scans were measured at different temperatures and pressures.

## Data treatment

Reflectivity curves were fitted with a modified Parratt algorithm [5]. The substrate electron density was subtracted from the resulting density profiles. The layer thickness was determined from the width at half maximum.

## Results – isotherms $CO_2$

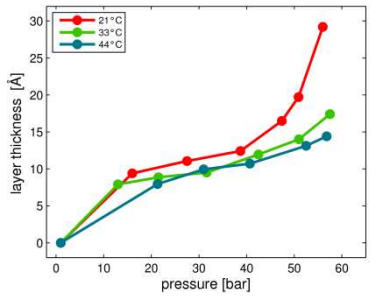


Isotherms for the adsorption of $CO_2$ were recorded at three different temperatures, see Figure 2. Below $T_C$ at 21 °C, the curve resembles the typical adsorption isotherm with divergence of the thickness at the condensation pressure. The near-critical measurement (T = 33 °C) and supercritical measurement (T = 44 °C) look similar, but the pressure dependence is clearly weaker.

**Figure 2**

## Results – supercritical region

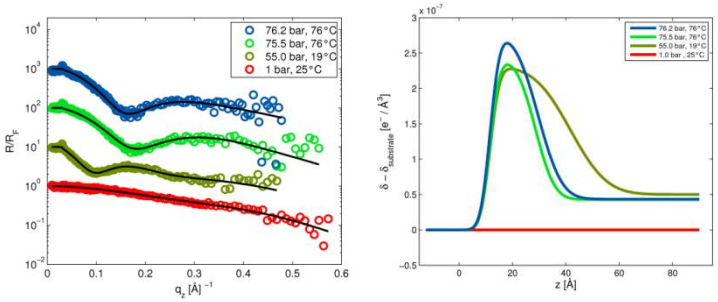


**Figure 3 XRR and dispersion profiles in the supercritical region.**

To access the supercritical regime, the temperature was set to 19 °C and the pressure to 55 bar. Then, the temperature was increased above the critical temperature to 76 °C = $T_C$ + 45 °C. In that way, a pressure of 76 bar was reached. Figure 3 shows the reflectivity curves of these measurements, and the corresponding dispersion profiles of the layer. The reflectivity curves are shifted for a better visibility. It is observed that the layer reaches a thickness of about 40 Å at 19 °C and 55 bar. This layer does not disappear when reaching the supercritical region. This means that the formation of an adsorption layer is observed in the supercritical region, where the gas cannot condense to a liquid phase. The layer thickness of about 20 Å is much higher than expected for a monolayer.

## Acknowledgement

We acknowledge the DELTA machine group for providing synchrotron radiation and. S. T. and F. W. the NRW Forschungsschule „Forschung mit Synchrotronstrahlung in den Nano- und Biowissenschaften“ for financial support.

## References

[1] J. Toth. Adsorption: Theory, Modeling and Analysis. Marcel Dekker, (2002)
[2] S. Holz, Adsorption von superkritischen Fluiden auf Festkörperoberflächen, Diplomarbeit TU Dortmund (2011)
[3] M. Paulus, C. Gutt, and M. Tolan. Phys Rev E 72, 061601 (2005)
[4] Data from http://webbook.nist.gov/chemistry/
[5] L. G. Parratt. Phys. Rev. 95, 359 (1954)

# Investigation of Q&P steels

K. Rüster, A. Steffen, M. Paulus, C. Sternemann and M. Tolan
Fakultät Physik / DELTA, Technische Universität Dortmund, D-44221 Dortmund, Germany
N. Große-Heilmann, C. Kronholz and A. Peters
Benteler Tube Management GmbH, D-33104 Paderborn, Germany

The Steel and its macroscopic characteristics (e.g. hardness, tensile properties) are affected by the crystalline structure, i.e. the proportion of austenite and martensite phase, which is changed during heat treatment (e.g. forging). To improve the material's characteristics the structure of different steel samples is analysed. For phase analysis x-ray diffraction (XRD) experiments have been carried out ex situ for pre-treated samples and in situ during the process of heating and cooling.

The Quenching and Partitioning (Q&P) process was originally proposed in 2003 by Speer, Matlock and Cooman [1]. At high temperatures steel is fully austenised and then quenched to a temperature between the martensite start and martensite finish point (see figure 1). Due to the suppressed cementite precipitation caused by the high silicon or aluminium content, the carbon diffuses from supersaturated martensite $M_1$ to austenite during the subsequent partitioning phase. Because of the austenite stabilising effect of carbon, the martensite finish temperature of the carbon enriched austenite is decreased below room temperature. Hence, after final quenching to room temperature, high carbon martensite $M_2$ is formed and metastable carbonenriched austenite γ remains. As a result superior mechanical properties are achievable.

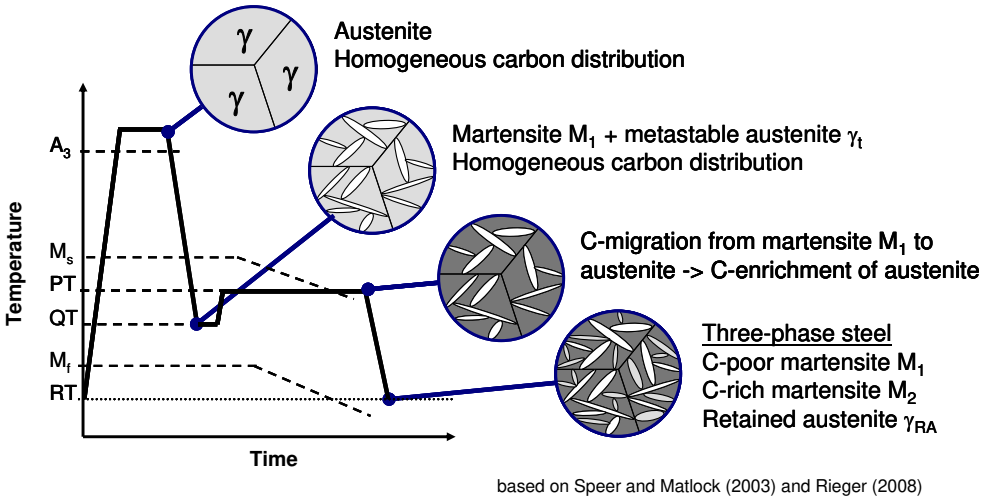


**Figure 1: The Quenching and Partitioning Process [2]; $A_3$: Upper critical temperature, $T<A_3$ ferrite starts to form; $M_s$: Martensite start temperature, $M_F$: Martensite finish temperature, $M_s>T>M_F$, formation of Martensite possible; PT: Partitioning temperature, holding temperature $T_2$; QT: Quenching temperature. Here QP=PT; RT: Room temperature.**

For ex situ experiments pre heat-treated samples were analysed. Four different steels were used: 30CrMo4, 20SiMnCrMo, 42SiCr, 20SiMnTiB. The samples were heated at 10°C /s and austenised at 950°C for 300s, quenched at 40°C /s to 300°C and 250°C, partitioned for 10s, 100s, 1000s, 2000s and 4000s and afterwards quenched at 40°C /s to room temperature. The heat treatment was done on a high speed dilatometer. The sample is 3 mm in diameter and 10 mm in length. The samples were cut into disks of 0.4 mm thickness for transmission XRD experiments at DELTA beamline BL9. The Image Plate detector mar345 was used at 27 keV photon energy and at 340 mm sample to detector distance. Thus seven Bragg reflections could be detected in order to analyse the fractions of face centered cubic austenite and body

centered cubic ferrite. First results of ex situ experiments were presented in the Delta-User-Report 2011 [3].

For in situ experiments a high temperature sample cell was used. The sample could be heated with two BORALECTRIC® heating elements and cooled with nitrogen. The measurements were carried out with the mar345 and the PILATUS100K detector.

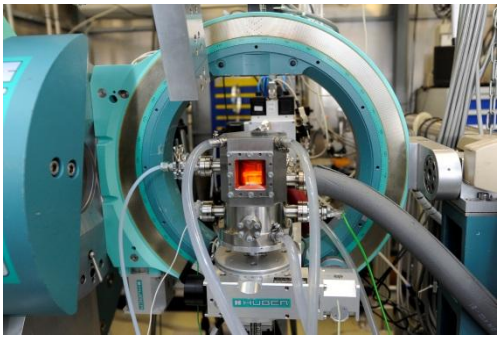

**Figure 2: High-temperature sample cell [Foto: J. Huhn]**

**Figure 3: Heating elements and sample holder with sample [4]**

The volume fractions of austenite during the in situ experiments are shown in figures 3 and 4. After annealing at high temperature the steel is nearly fully austenised. While the steel is annealed at the holding temperature $T_2$=300°C (see figure 4), carbon diffuses from supersaturated ferrite to austenite. The austenite is stabilized by carbon. After final cooling to room temperature the volumefraction of austenite remains stable at 9,4%. In comparison the sample in figure 5 is annealed at lower holding temperature $T_2$=200°C. No carbon diffusion takes place. Therefore the austenite is not stabilised by carbon. After cooling to room temperature the volumefraction of austenite drops from 25,6% to 10,3%. The higher austenite volumefraction of the sample shown in figure 5 can be explained by a higher cooling rate during quenching.

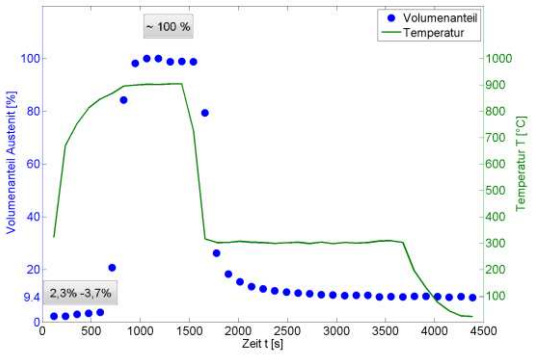


**Figure 4: Volumefraction of austenite for heat-treatment with the holding temperature $T_2$=300°C [4]**

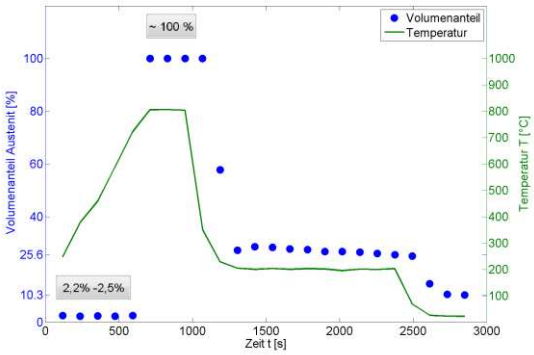


**Figure 5: Volumefraction of austenite for heat-treatment with the holding temperature $T_2$=200°C [4]**

## References


[1] Speer, J.; Matlock, D. K.; Cooman, B. D. and Schroth, J, Acta Materialia 51(9), 2611-2622, (2003).
[2] Matlock, D.; Bräutigam, V. and Speer, J., Trans Tech Publications Ltd, pp. 1089-1094, (2003).
[3] Große-Heilmann, N., Delta-User-Report 2011.
[4] Rüster, K., 'Einfluss des Quenching & Partitioning-Prozesses auf den Austenitgehalt von Stählen', Diplomthesis (2012).

# Structural investigations on ternary and quaternary inter alkali metal acetylides by means of synchrotron powder diffraction / Valence changes in dicarbide solid solutions induced by structural changes

S. Liebig, S. Busch and U. Ruschewitz*

*Department für Chemie, Universität zu Köln, 50939 Köln, Germany*

**email: uwe.ruschewitz@uni-koeln.de*

The structures of three inter alkali metal acetylides $CsNaC_2$ (**1**), $CsKC_2$ (**2**), and $CsRbC_2$ (**3**) as well as their high temperature structural behavior was investigated by means of synchrotron powder diffraction at BL9. Due to their high sensitivity to moisture the samples were prepared in glass capillaries. For technical reasons rotation of these capillaries is necessary during the diffraction experiments to avoid texture effects of single crystallites on the image plate detector. To overcome these difficulties the furnace G670.3 (Huber, Figure 1) was installed at BL9 with the help of the DELTA staff (C. Sternemann). Due to known temperature differences between the thermocouple (Pt-10%Rh-Pt) and the real temperature at the sample a Si standard was used for temperature calibration (Figure 2).

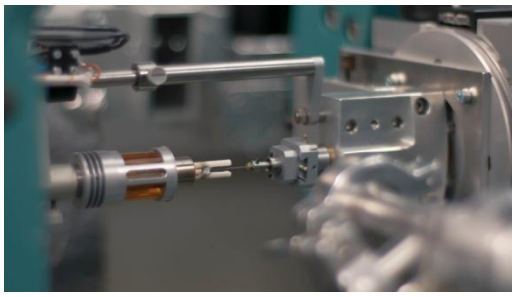

*Figure 1: Sample environment at BL9, DELTA.*

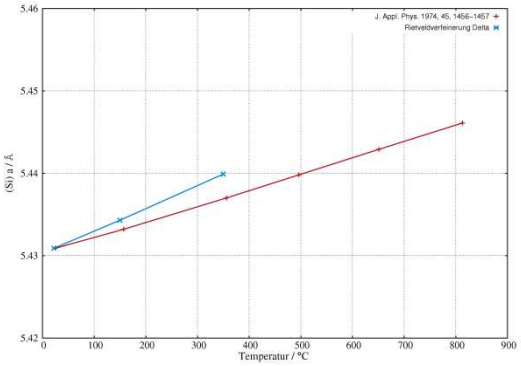


*Figure 2: Calibration measurements for Si.*

Structural investigations at room temperature revealed crystal structures related to the *anti*-$PbCl_2$ type structure for **2** and **3**, while **1** showed a slightly different structure type. After data reduction (FIT2D) all diffraction patterns were indexed with orthorhombic unit cells and structure solution was carried out using the charge flipping algorithm implemented in JANA2006[1]. Accurate allocation of the resulting electron density maps led to reasonable structural models, which were approved by comparison with the known crystal structure of $KNaC_2$. Final Rietveld refinements (GSAS[2]) confirmed these models as shown for $CsNaC_2$ in Figure 3. For **1** and **2** the temperature dependent measurements showed reversible phase transitions (first order) leading to different high temperature modifications of these compounds. The structure of HT-$CsKC_2$ (**2**) is closely related to the structure at room temperature (*anti*-$PbCl_2$ type) with a change of the orientation of the $C_2^{2-}$ dumbbells. This process can be described as an isosymmetric phase transition. HT-$CsNaC_2$ (**1**) crystallizes in a tetragonal unit cell (Figure 4), which is also found for HT-$NaRbC_2$[3]. But the diffraction pattern gave evidence for an unusual disorder of the $C_2^{2-}$ dumbbells at higher temperatures, as the c-axis, along which the dumbells are orientated, shortens. In Figure 5 the electron density map is shown in red together with one possible orientation of the acetylide anion. These

results were confirmed by accurate Rietveld refinements comparing different models for selected temperatures.

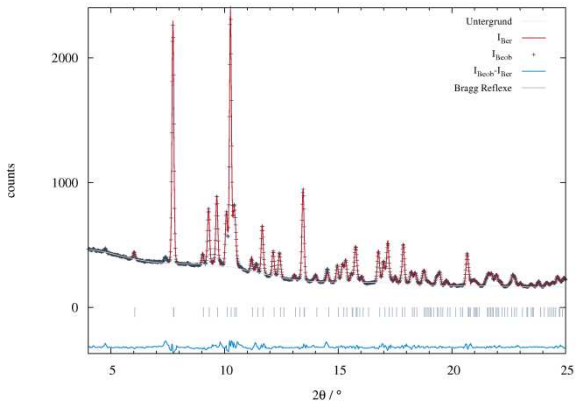


*Figure 3: Rietveld refinement of $CsNaC_2$ at room temperature.*

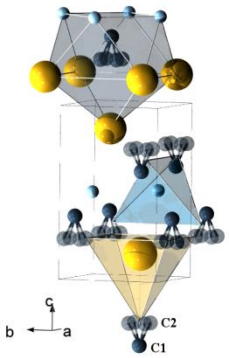


*Figure 4: Unit cell of HT-$CsNaC_2$ (Cs: yellow, Na: blue, C: dark blue).*

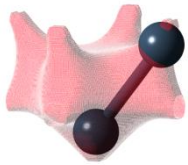

*Figure 5: Electron density map as calculated with the charge flipping algorithm for the $C_2^{2-}$ dumbbell in $CsNaC_2$.*

Previous investigations have shown that the solid solution $Eu_xSr_{1-x}C_2$[4] is a perfect example of a strain free system following Vegard's law, as both cations ($Eu^{2+}$, $Sr^{2+}$) have similar radii. $Eu_xCa_{1-x}C_2$ with different radii of the divalent ions ($r(Eu^{2+}) > r(Ca^{2+})$) seems to be a promising solid solution for possible valence changes of Eu, as found for Yb in $Yb_xCa_{1-x}C_2$[5]. Due to the larger difference of the respective radii a higher strain is expected, which might lead to a valence effect of Eu. $Eu_xCa_{1-x}C_2$ crystallizes in different modifications depending on x as shown in Figure 6.

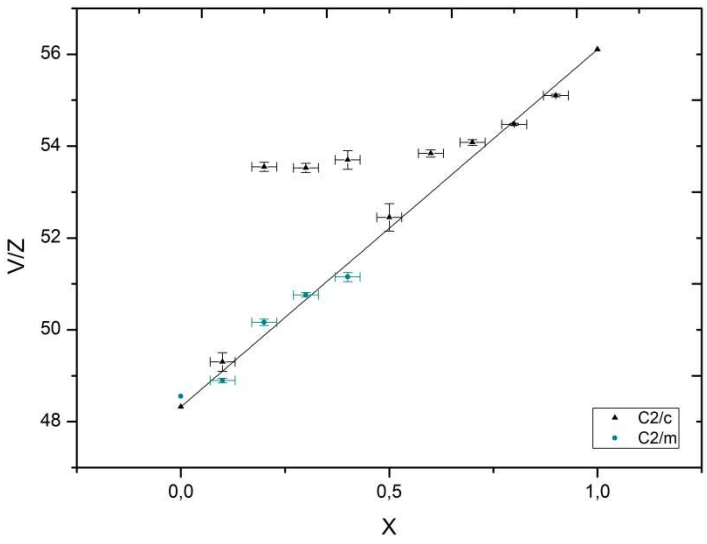


*Figure 6: Unit cell volumes per formula unit of $Eu_xCa_{1-x}C_2$ as a function of x. The structure of the compounds was elucidated by synchrotron powder diffraction with an energy of 22.5 keV.*

Based on synchrotron powder diffraction data at room temperature two different modifications were found in $Eu_xCa_{1-x}C_2$ depending on x: for high x ($0.5 < x < 0.9$) the $ThC_2$ type structure (C2/c) is realized, whereas for $0.1 < x < 0.4$ the $CaC_2$-III type structure (C2/m) is observed. Their unit cell volumes follow Vegard's law (Figure 6). In addition a second phase was observed for $0.1 < x < 0.4$, which was, in a first attempt, assigned to the $ThC_2$ type structure. Figure 7 shows the Rietveld refinement (GSAS[2]) of $Eu_{0.3}Ca_{0.7}C_2$ only including the $CaC_2$-III type structure, whereas in Figure 8 also the $ThC_2$ type structure was included in the refinement. The resulting R factors are given in Table 1. The improvement of the refinement is obvious.

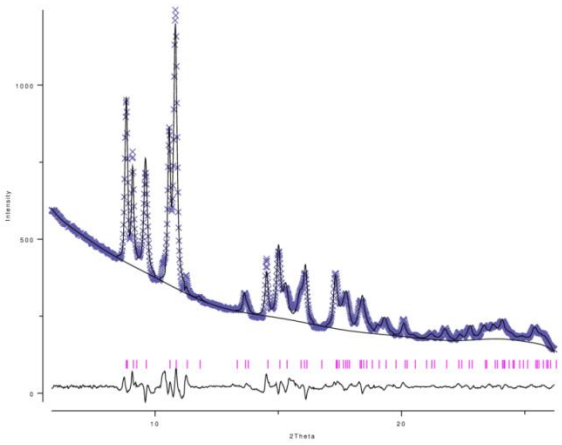

*Figure 7: Rietveld refinement of $Eu_{0.3}Ca_{0.7}C_2$ only including the $CaC_2$-III type structure.*

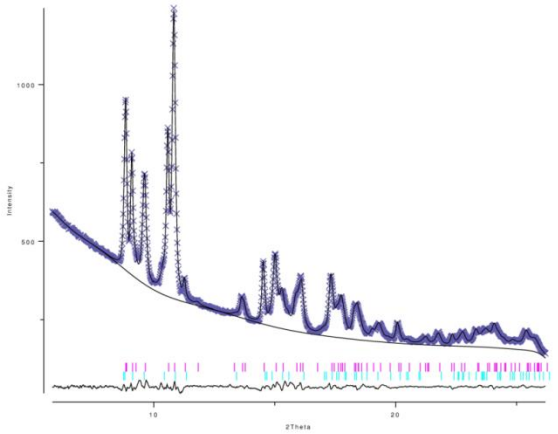

*Figure 8: Rietveld refinement of $Eu_{0.3}Ca_{0.7}C_2$ including the $CaC_2$-III and the $ThC_2$ type structures.*

*Table 1: R factors of the Rietveld refinements shown in Figure 7 and 8.*

| RG | C2/m | | RG | C2/m | C2/c |
|---|---|---|---|---|---|
| $R_{Bragg}$ | 0.0357 | | $R_{Bragg}$ | 0.0089 | 0.0163 |
| $wR_p$ fitted | 0.0290 | | $wR_p$ fitted | 0.0142 | |
| $R_p$ fitted | 0.0192 | | $R_p$ fitted | 0.0101 | |

High resolution synchrotron powder diffraction data and additional XANES spectroscopic investigations (for the latter beamtime has already been allocated at DELTA for 10/2012) are needed to investigate the structural properties of this solid solution in more detail, i.e. to clarify, whether for $0.1 < x < 0.4$ indeed two phases are coexisting, and to confirm possible Eu valence changes.

## References


[1] a) L. Palatinus, *J. Appl. Crystallorgr.* **2007**, *40*, 786-790. b) V. Petricek, M. Dusek, L. Palatinus, *Jana 2006. The crystallographic computing system. Institute of physics, Praha, czech republic*, **2006**.

[2] A. Larson, R. von Dreele, *General Structure Analysis System (GSAS, Los Alamos National Laboratory Report LAUR*, **2000**.

[3] H. Billetter, doctoral thesis, Köln, **2010**.

[4] P. Link et al., *Z. Anorg. Allg. Chem*. **2010**, *636*, 2276.

[5] P. Link et al., manuscript in preparation.

# In situ XRD of $CO_2$ loaded flexible metal-organic frameworks

**Andreas Schneemann[a], Sebastian Henke[a], Christian Sternemann[b], Michael Paulus[b], Florian Wieland[b], and Roland A. Fischer[a]**

[a]Lehrstuhl für Anorganische Chemie II – Organometallics and Materials, Ruhr Universität Bochum; [b]Fakultät Physik/DELTA, Technische Universität Dortmund

Metal-organic frameworks (MOFs) are porous materials consisting of metal clusters bridged by organic linkers. Among their outstanding properties are very high surface areas and pore volumes, making them interesting materials for gas adsorption or separation. One of the most unique features of these materials which is not found for other porous materials like zeolithes, mesoporous silicas or active charcoals is a so called 'flexibility' characterized by a structural change upon exposure to an outer stimulus.[1, 2] Such a stimulus can for example be generated by the sorption of a guest molecule from the liquid or gaseous phase (figure 1).

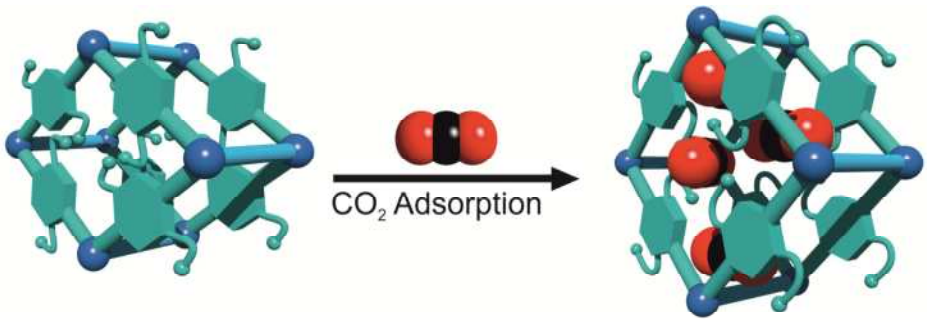


**Figure 1:** Schematic illustration of the $CO_2$ induced breathing effect in metal-organic frameworks of the type $[M_2(BME\text{-}bdc)_2(dabco)]_n$

In previous works we analyzed the functionalized metal-organic framework $[Zn_2(BME\text{-}bdc)_2(dabco)]_n$ (**4**), which undergoes a phase transition from a narrow pored (**np**) form to a large pored (**lp**) form upon exposure to polar guest molecules.[3, 4] This is for example evidenced when the material is dried after solvothermal synthesis and the solvent molecules occupying the pore space are removed (figure 2 right). Furthermore $CO_2$-sorption isotherms also indicate a phase transition, when a certain gate opening pressure is applied (figure 2 left). When now in a flow cell a certain $CO_2$ pressure is applied we can measure the 2D-X-ray diffraction patterns and thus can *in-situ* observe the transition from **np** to **lp** form. From this studies we can gain a closer look on the mechanism of the phase transition. Recently we synthesized analogous materials of the composition $[Co_2(BME\text{-}bdc)_2(dabco)]_n$ (**1**), $[Ni_2(BME\text{-}bdc)_2(dabco)]_n$ (**2**) and $[Cu_2(BME\text{-}bdc)_2(dabco)]_n$ (**3**) and the CO2 sorption isotherms showed that depending on the choice of the metal-centre in the MOF a different phase transition pressure are observed.[5]

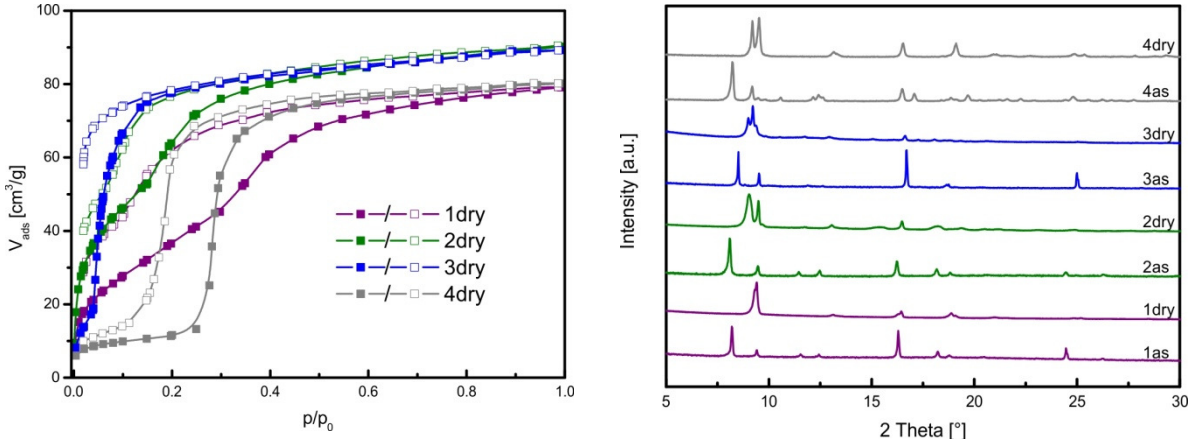


**Figure 2:Left:** CO2 isotherms of pillared layer MOFs of the type $[M_2(BME\text{-}bdc)_2(dabco)]_n$ (M = Co, Ni, Cu, Zn). **Right:** Diffraction patterns of dry and as-synthesized materials of the materials **1-4**.

As suggested by the $CO_2$ sorption isotherms we observe very different behaviors during the loading process with $CO_2$ at 195 K (figure 3). For material **3** we observe the phase transition in the narrowest pressure regime and the material is already completely in the **lp** form when a pressure of 500 mbar is applied. On the desorption branch, material **3** stays in the **lp** form until 100mbar are reached and remains in an intermediate state when the $CO_2$ pressure is at 0 mbar. The cobalt containing material **1** is staying in the **np** form until a relatively high pressure is applied and the increase of $CO_2$ uptake evidenced by the sorption isotherms is the slowest. First, a small amount of $CO_2$ is adsorbed by the framework without any effect on the structure until a certain gate opening pressure is reached (300-400 mbar). At this point we see an increase in the slope of the isotherm as well as a shift in the XRD pattern at 400 mbar which is indicating the formation of an intermediate phase. At 1000 mbar the material is completely present in the **lp** form. The shift back to the intermediate phase is observed at 500 mbar and at 15 mbar the material is present in its **np** form. Material **2** contains Ni as the metal centre, it is observed that the diffraction pattern is already shifting when 100 mbar of $CO_2$ are applied, however the **lp** phase is not fully reached before a pressure of 1000 mbar is applied. On the desorption branch we see the formation of reflexes representative for the intermediate phase at 250 mbar, and at 0 mbar the reflections indicative for the **np** form are present, but still a big fraction of the material stays in the intermediate form.

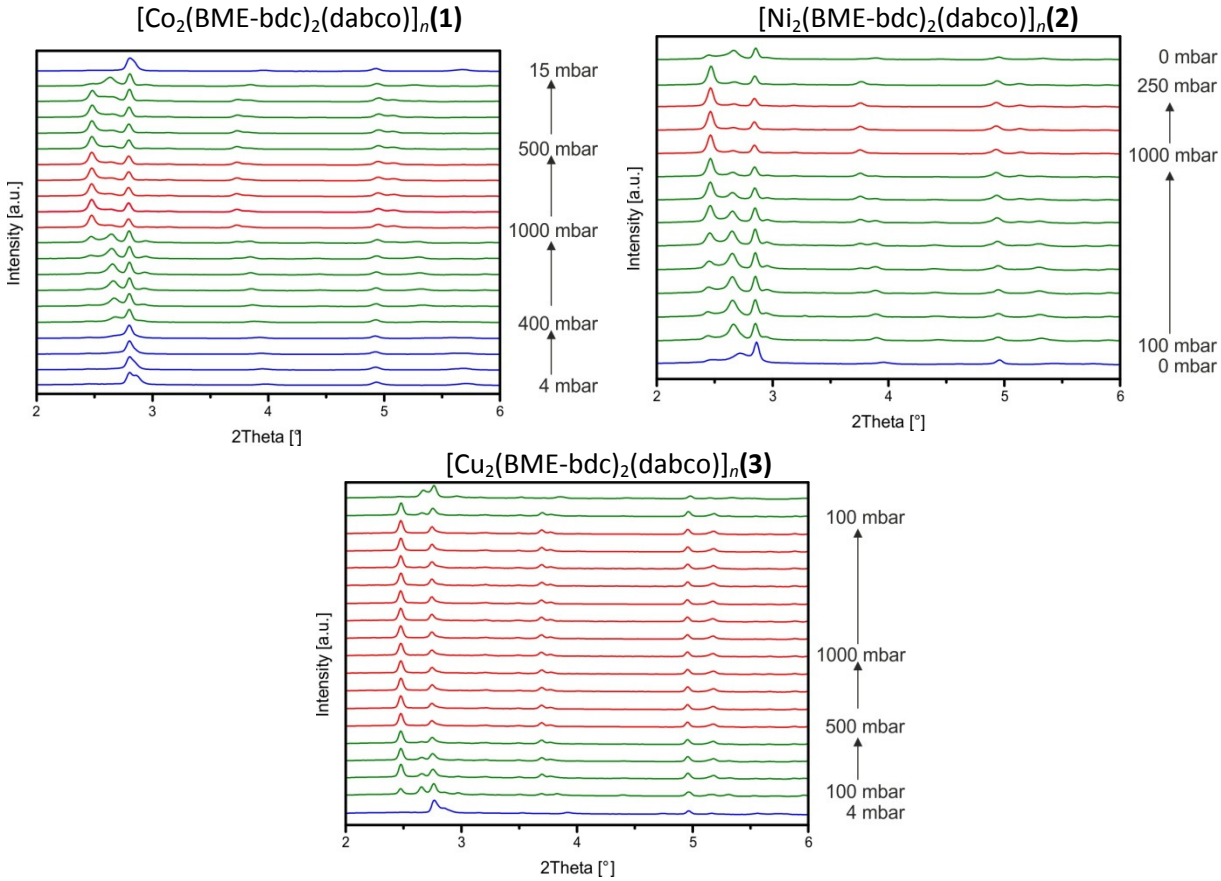


**Figure 3:** *In Situ* PXRDs during CO2 loading of **1**,**2** and **3**. Blue patterns represent the np form, green an intermediate form and red the lp form.

## References


[1] S. Horike, S. Shimomura, S. Kitagawa, *Nat. Chem.* 2009, *1*, 695.
[2] G. Ferey, C. Serre, *Chem. Soc. Rev.* 2009, *38*, 1380.
[3] S. Henke, R. Schmid, J.-D. Grunwaldt, R. A. Fischer, *Chem.--Eur. J.* 2010, *16*, 14296.
[4] S. Henke, F. Wieland, M. Meilikhov, M. Paulus, C. Sternemann, K. Yusenko, R. A. Fischer, *CrystEngComm* 2011.
[5] A. Schneemann, S. Henke, F. Wieland, C. Sternemann, M. Paulus, R. A. Fischer, *manuscript in preparation* 2012.

# Influence of Alkyl Side Chain Length and Cast Temperature on the In-plane Stacking of P3AT Crystallites and their OFET performance

*T.S. Shabi[1], S. Grigorian[1], M. Brinkmann[2], U. Pietsch[1], N.Koenen[3], N. Kayunkid[2], U. Scherf[3], M. Fakhri[4], T.Riedl[4]*

[1.] *Solid State Physics, University of Siegen, Germany*
[2.] *Institute Charles Sadron, CNRS-University of Strasbourg, France*
[3.] *Macromolecular Chemistry, University of Wuppertal, Germany*
[4.] *Electronic Components, University of Wuppertal, Germany*

The solution processable conjugated conducting polymers are becoming an active material for the fabrication of flexible, cheap, and less weight electronic devices. Among the conjugated polymers, poly(3-alkylthiophene)s (P3ATs) have placed a vital role due to their satisfying environmental stability and remarkable electrical and optical properties. Mainly, P3AT polymers are self-organizing into two orientations called as face- and edge-on ones. The face- and edge-on oriented crystallites can be distinguished by the direction of π-π stacking along perpendicular and parallel to the substrate plane, respectively. Among the two orientations, edge-on has been found to be the favorable for the fabrication of P3AT organic field effect transistor (OFET). According to the best of our knowledge still there is no unique technique for to preparation of polymer films with exclusively edge-on orientation. We have shown that the reduction in cast temperature can increase dramatically the amount of edge-on oriented P3AT crystallites on the substrate.

The crystallinity and orientation of P3ATs were enhanced by reducing the cast temperature of the film down to -30°C. The reduction in cast temperature increases the edge-on oriented crystallites and results an (h00) elliptical spot on the 2D detector (Figure 1e to 1h). In contrary, the RT cast films are showing (h00) powder-like rings (Figure 1a to 1d).

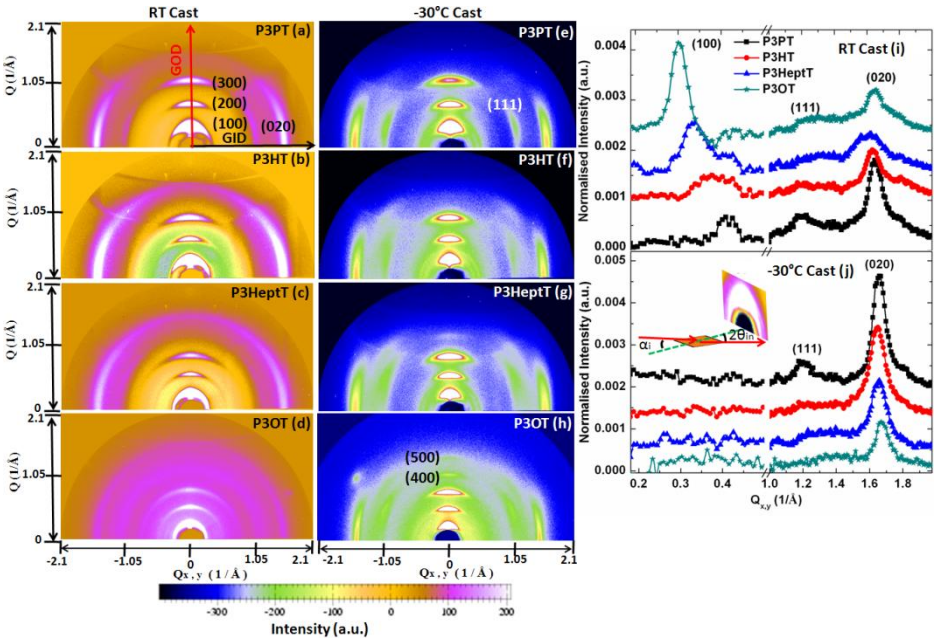


Figure 1: 2D X-ray diffraction pattern of RT (a till d), -30°C cast (e till h), and the corresponding line profiles (i and j).

We could enhance the edge-on oriented crystallites through low temperature casting but the in-plane stacking of P3AT crystallites are getting weaker as the side chain length increases due to the augment in steric hindrance between the alkyl side chains. It can be explained by the serious reduction in (020) scattered intensity and fading of (111) reflection (Figure 1i and 1j) as the side chain length increases. Increase of face-on oriented crystallites as increasing the side chain length while casting at RT might be due to the delay in initiation of nucleation at fixed growth parameters because of their enhanced solubility. So, it can increase the face-on oriented crystallites due to the reduction in growth time as the side chain length increases. The augment in in-plane stacking of P3AT crystallites as reducing the cast temperature as well as the side chain length enhances the field effect mobility and photoluminescence emission. These findings suggest that the highly in-plane stacked P3AT crystallites are mandatory for the fabrication of high throughput devices and it can be achieved by reducing the cast temperature together with the reduction of alkyl side chain length.

# Influence of Cr fraction on the graphite content in diamond tools

Andre Steffen[1], Manuel Ferreira[2], Michael Paulus[1], Wolfgang Tillmann[2], Metin Tolan[1]

[1] Fakultät Physik / DELTA, Technische Universität Dortmund, 44221 Dortmund
[2] Lehrstuhl für Werkstofftechnologie, Technische Universität Dortmund, 44221 Dortmund

The aim of this project is to solve the atomic structure of the interfacial area between diamond grains and metal matrices in sintered diamond metal composites [1-2].
This study deals with the influence of chromium on the graphite formation within diamond metal composites. Former results indicate that by adding chromium to the metal matrix the graphitization of diamond during sintering is reduced [1]. To analyze that dependency in detail 3 metal matrix systems (Co, Fe Ni) with varying chromium content (0 wt% to 0.5 wt%) were analyzed by X-ray diffraction (XRD).

The experiment was performed at beamline BL9 at DELTA using a photon energy of E = 27keV [3]. The diamonds were placed in a capillary (diameter 1mm) that was rotating during the experiment. A MAR345 image plate detector was used to collect the diffraction patterns.

The XRD patterns reveal that the influence of chromium on the graphite content is strongly dependent on the metal matrix. Focusing on the diamonds extracted from a Co/Cr matrix (see Fig 1) the graphite reflection at $2\theta = 7.8°$ can be clearly identified if the Cr fraction is small (Cr wt% < 0.1). By increasing the Cr content up to 0.5 wt% the graphite reflection is reduced. On the other hand none of the Fe matrix samples does show any amount of graphite, which is in contrast to former results. Furthermore it can be seen that all samples obtained from of Ni matrices show the presence of graphite, independent of the Cr content in the investigated regime (Cr wt% <= 0.5%).

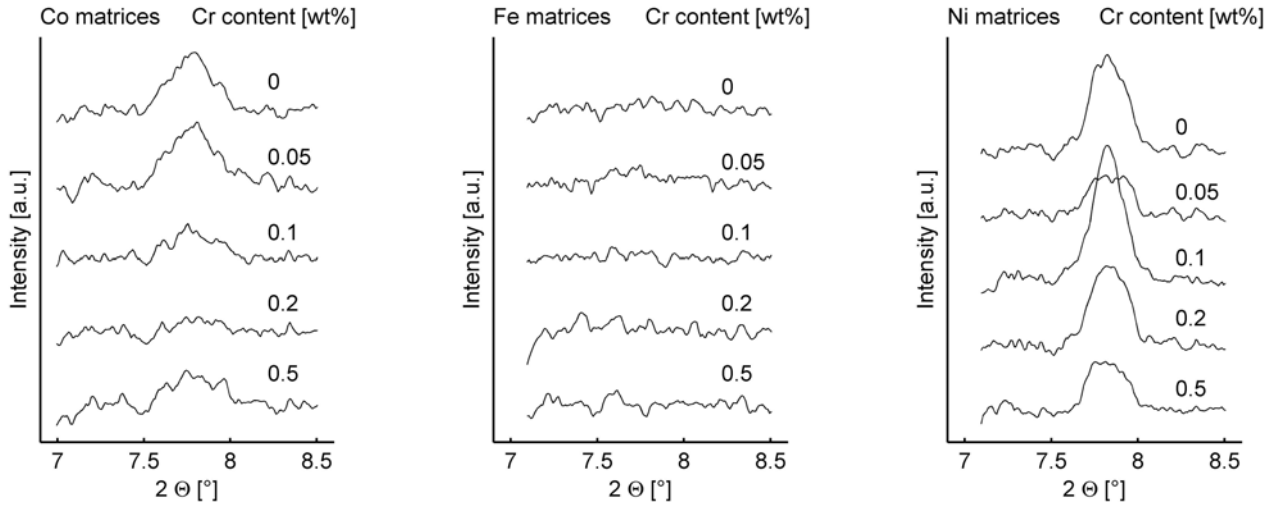


*Figure 1: XRD pattern of diamonds extracted out of sintered metal matrices.*

The NRW-Forschungsschule "Forschung mit Synchrotronstrahlung in den Nano- und Biowissenschaften" and the Deutsche Forschungsgemeinschaft (Grant No. TI 343/36-1) is gratefully acknowledged for financial support. Furthermore, the authors would like to acknowledge DELTA for providing the synchrotron radiation.
The performed experiment is part of a project funded by the Deutsche Forschungsgemeinschaft (Grant No. TI 343/36-1).

[1] A. Steffen, M. Ferreira, M. Paulus, W. Tillmann, M. Tolan, Conf. Proc. EuroPM, Basel, Vol.2 (2012)
[2] W. Tillmann, M. Ferreira, A. Steffen, S. Bieder, J. Möller, K. Rüster, M. Tolan, Conf. Proc. EuroPM, Basel, Vol.2 (2012)
[3] C. Krywka, C. Sternemann, M. Paulus, N. Javid, R. Winter, A. Al-Sawalmih, S. Yi, D. Raabe, and M. Tolan, J. Synchrotron Rad. 14, 244 (2007).

# In situ X-ray diffraction studies of diamond tool binder phase feedstock materials

Andre Steffen[1], Manuel Ferreira[2], Michael Paulus[1], Karin Rüster[1], Wolfgang Tillmann[2], Metin Tolan[1]

[1] Fakultät Physik / DELTA, Technische Universität Dortmund, 44221 Dortmund
[2] Lehrstuhl für Werkstofftechnologie, Technische Universität Dortmund, 44221 Dortmund

The field of natural stone and concrete machining has high demands concerning the fabrication and quality assurance of the grinding tools used. Because of the required high performance of the cutting material in contact with hard materials, diamond-metal composites are mainly used for such applications [1]. These grinding segments are manufactured powder metallurgically. The manufacturing processes include the premixing of diamond-metal compositions (diamond amount 5-10 vol-%), densification by mechanical uniaxial pressing, sintering in a vacuum furnace, and hotpressing [2]. The following experiments analyze the crystallographic behavior during the sintering process of commonly used metal-powders for diamond tool application. The investigations deliver useful information about the temperature induced structural changes in the metallic material and its influence on the mechanical characteristics of the metal matrix, as well as occuring changes of the carbon solubility after the allotropic phase transformation. In a former experiment the phase transition (hcp-fcc) of cobalt powder during heat treatment (10°C <= T <= 620°C) was already investigated in-situ at beamline BL9 at DELTA [3].

To analyse the phase compositions of iron, chromium and nickel powders X-ray diffraction (XRD) studies were performed at beamline BL9 at DELTA [4]. The photon energy was E = 27 keV. To achieve high temperatures up to T = 950°C a high temperature sample cell was used. To avoid oxidation of the metal powders the cell was flushed by inert gas during the experiment. The metal powders were placed in a capillary. In all studies the first image was taken at room temperature. While the samples were heated up to the maximum heating power (resulting in $T_{max} \approx 950°C$) and finally cooled down to room temperature the MAR345 image plate detector took an image every ~130s.

In Figure 1 the experimental data is plotted. At the beginning chromium powder only occurs in body entered cubic (bcc) phase. At high temperature a nearly complete (and irreversible during cooling) phase transition from cubic (bcc) to hexagonal closed packed (hcp) phase takes place. After the temperature cycle only little cubic phase but a significant amount of hexagonal chromium phase is present.
The crystal structure of the nickel powder does not change during the experiment. Only a shift of the scattering angle, that is caused by the lattice extension due to increasing temperature, and a change of the scattering intensity of the Bragg-reflection can be observed.
On the other hand the XRD patterns of the iron powder show a complete and reversible phase transition. At the beginning the iron powder occurs only in bcc phase. Within the first 10min of the experiment the full width at half maximum of the bcc [110] reflection decreases, indicating a growth of the average grain size. At maximum temperature a complete phase transition from bcc to fcc (face centered cubic) phase takes place. During cooling the reverse phase transition executes. As before the annealing process at the end only bcc phase is present, however with bigger grain size.

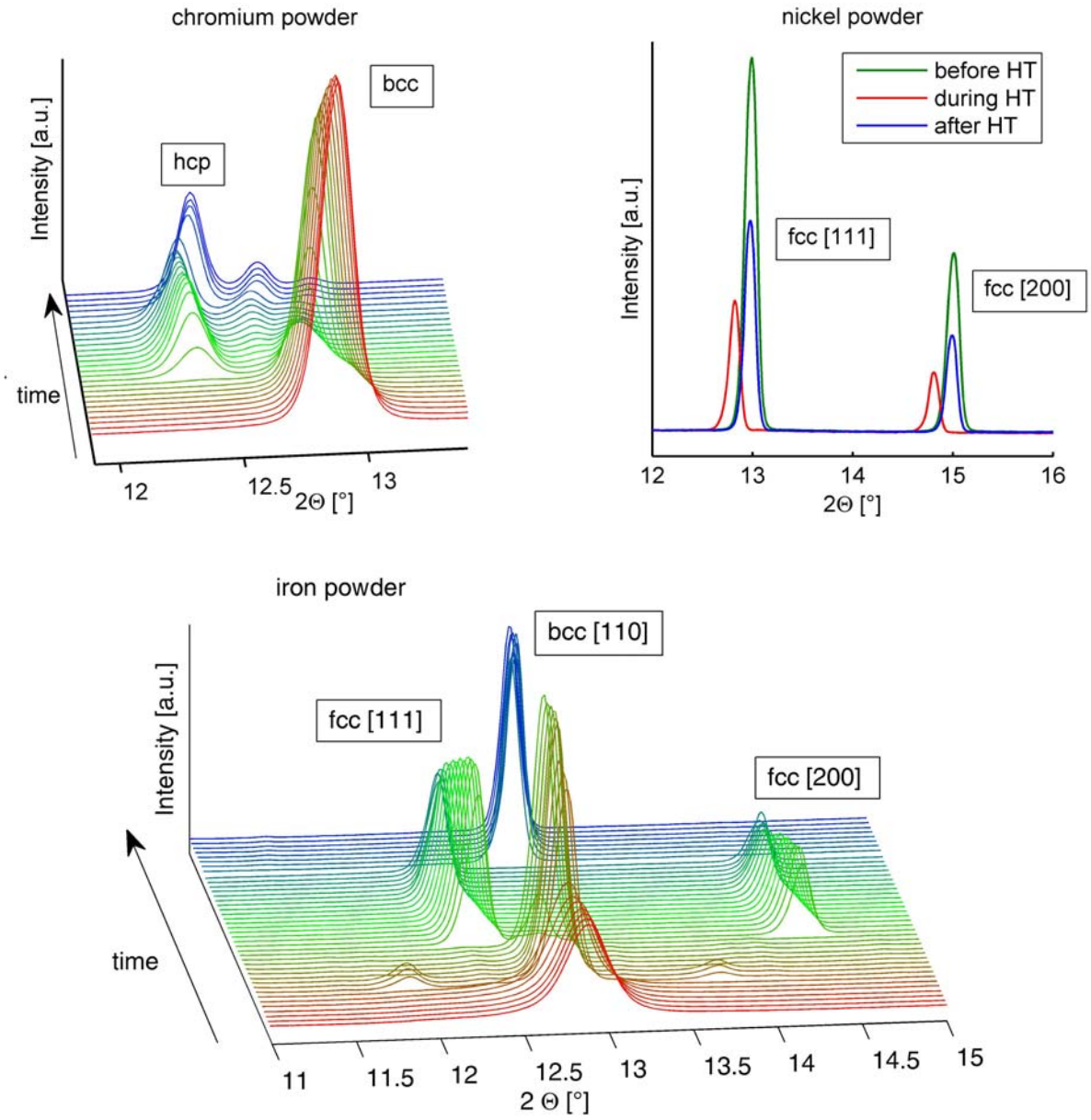


*Figure 1: Diffraction patterns of tempered chromium (top left), nickel (top right) and iron (bottom) powder.*

The NRW-Forschungsschule "Forschung mit Synchrotronstrahlung in den Nano- und Biowissenschaften" and the Deutsche Forschungsgemeinschaft (Grant No. TI 343/36-1) is gratefully acknowledged for financial support. Furthermore, the authors would like to acknowledge DELTA for providing the synchrotron radiation.

[1] W. Tillmann, M. Gathen, C. Kronholz, MaterialwissenschaftenundWerkstofftechnik, 38:112-115 (2007).
[2] A. Molinari, F. Marchetti, S. Gialanella, P. Scardi, A. Tiziani, Materials Science and Engineering A, 130:257-262 (1990).
[3] A. Steffen, M. Ferreira, C. Kronholz, M. Paulus, C.J. Sahle, W. Tillmann, M. Tolan, Conf. Proc. 1st ICSCM, Hannover, 145 (2011).
[4] C. Krywka, C. Sternemann, M. Paulus, N. Javid, R. Winter, A. Al-Sawalmih, S. Yi, D. Raabe, and M. Tolan, J. Synchrotron Rad. 14, 244 (2007).

# Diamond-metal interactions in vacuum sintered and hot-pressed diamond grinding tools

Manuel Ferreira, Wolfgang Tillmann, Sarah Thutewohl

Lehrstuhl für Werkstofftechnologie, Technische Universität Dortmund, D-44221 Dortmund

The field of natural stone and concrete machining has high demands concerning the fabrication and quality assurance of the grinding tools used. Because of the required high performance of the cutting material in contact with hard mineral materials, diamond-metal composites are mainly used for such applications [1]. These small grinding segments are manufactured powdermetallurgically. The manufacturing processes include the premixing of diamond-metal compositions (diamond amount 5-10 vol-%), densification by mechanical uniaxial pressing, sintering in a vacuum furnace, and hotpressing. The used elements for metal matrix were chromium, cobalt and iron.

The experiment shows the influence of different sintering techniques (hotpressing and vacuum sintering) on the crystalline structure on the interfacial area between the diamond and the metal. Furthermore the influence of the temperature and holding time on the presence and amount of formed phases.

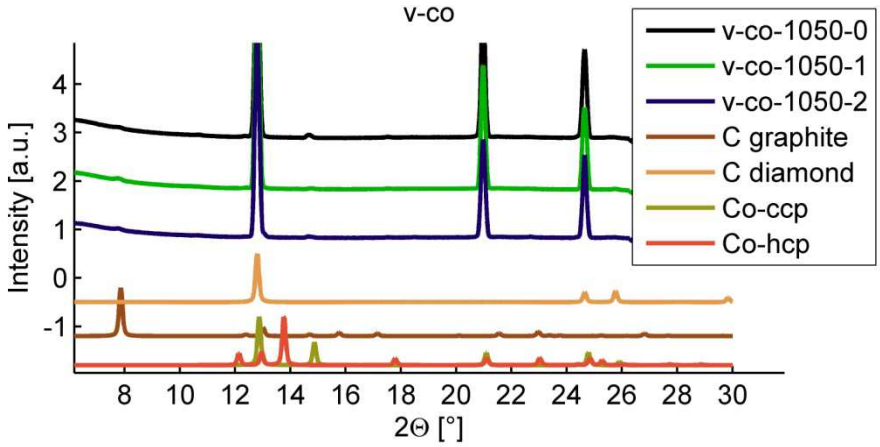


Fig. 1: Vacuum sintered cobalt at 1050°C

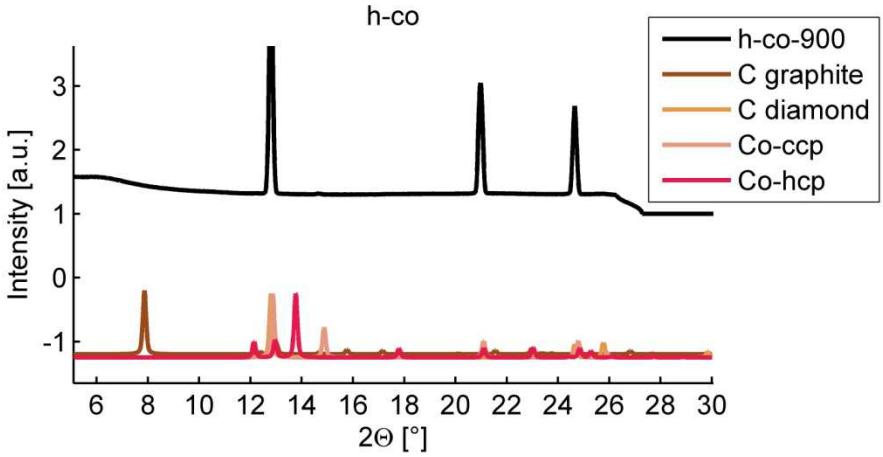


Fig. 2: Vacuum sintered cobalt at 900°C with 3 minutes holding time.

The xrd-spectrum of diamonds in vacuum sintered cobalt is shown in Figure 1, the temperatures while sintering were identical. In every sample the formation of graphite can be assumed. Moreover co-hcp and co-ccp cannot be exactly determined. The graphs are similar, that indicates the holding time has not too much influence on the transformation to graphite. The temperature and holding time at hot-pressed cobalt (Figure 2) are lower. In this case no graphite reflex at 7,8° can be detected. This indicates that the temperature must be higher than 900°C to enforce a graphite formation. Another reason for it could be the lower holding time.

In Figure 3 the vacuum sintered chromium is shown. The extracted diamonds sintered with one and two hours holding time are similar. Comparing these two spectra with the reference data, the formation of chromium-carbides seem to be possible at higher holding times. The hot-pressed samples are plotted in Figure 4 and distinct $Cr_3C_2$ reflexes (11,41° + 11,76°) can be identified at higher hot-pressing temperature of 1150 °C. Furthermore there are weak reflexes at the same angles in analysed diamonds, which were hot-pressed at 1000°C. This could indicate a carbide formation at lower temperatures.

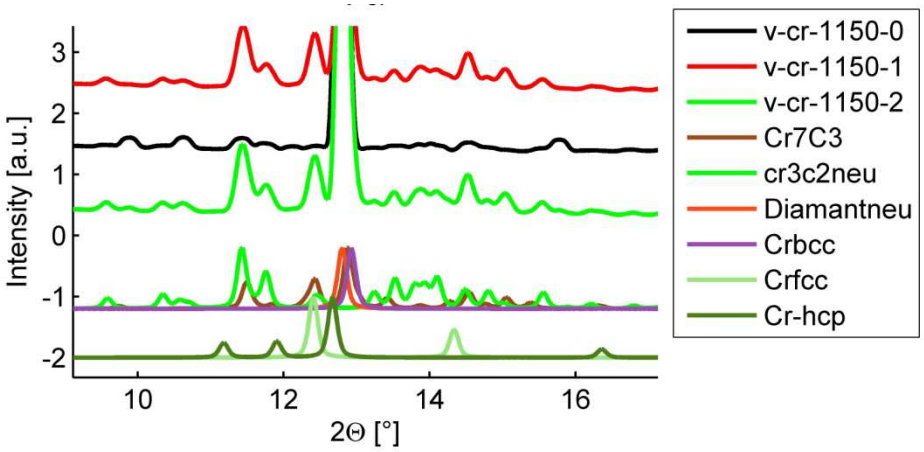


Fig. 3: Vacuum sintered chromium at 1150°C

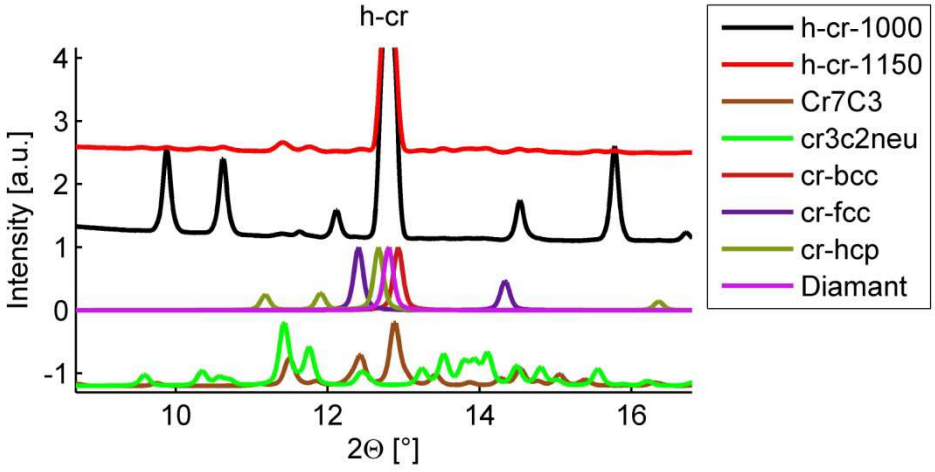


Fig. 4: Hotpressed chromium

[1] A. Steffen, M. Ferreira, M. Paulus, W. Tillmann, M. Tolan, Conf. Proc. EuroPM, Basel, Vol.2 (2012)

# Lattice expansion in optically excited InAs/GaAs quantum dots

Sebastian Tiemeyer*,[a], Michael Bombeck[b], Michael Paulus[a], Christian Sternemann[a], Julia Nase[a], Florian J. Wirkert[a], Manfred Bayer[b], and Metin Tolan[a]

[a] *Fakultät Physik/DELTA, Technische Universität Dortmund, 44221 Dortmund, Germany;*

[b] *Experimentelle Physik II, Technische Universität Dortmund, 44221 Dortmund, Germany.*

*email: sebastian.tiemeyer@tu-dortmund.de

Quantum dot (QD) heterostructures are a manifold research topic offering both the discovery of principal knowledge in terms of quantum information processing and the development of optoelectronic devices [1]. In this study, we have investigated the effect of polaronic states enclosed in excited InAs/GaAs QDs [2-4] on the crystal lattice. Therefore, we have conducted high-resolution x ray diffraction (XRD) measurements at the beamlines BL9 and P08 of the synchrotron radiation facilities DELTA (TU Dortmund) and PETRA III (HASYLAB), respectively.

The study was performed on an InAs/GaAs QD multilayer structure grown on a $5 \times 5$ mm$^2$, (001) oriented GaAs substrate. A 500 nm thick layer of GaAs was grown on the substrate in order to prepare a clean surface. Following, an InAs layer of 1.2 nm thickness was deposited at a growth temperature of $T = 566$ °C forming a wetting layer followed by the formation of the QDs. Subsequently, a 30 nm GaAs spacing layer was grown. This was repeated until 5 QD layers were fabricated, and the last QD layer was finally capped with 50 nm GaAs. The QD density was on the order of $10^{10}$ cm$^{-2}$, whereas the size of the QDs was approximately 8 nm and 30 nm in height and diameter, respectively. Furthermore, the thickness of the wetting layers was found lying below 1 nm. Serving as a reference, a (001) oriented bulk GaAs wafer of comparable size and mass was also investigated. In the case of both the QD and GaAs sample the GaAs crystal lattice was probed. For this reason, every mentioning of the QD sample's crystal lattice refers in the following to the GaAs lattice of the embedding matrix and substrate.

The set-up dedicated for the simultaneous optical excitation and probing by XRD of the QD sample is shown on the left hand side of Figure 1. Optical excitation was guaranteed by a diode-pumped Nd:YAG laser supplying laser radiation of 532 nm wavelength. Employing this wavelength, electron-hole pairs were generated within the GaAs matrix material, which relaxed subsequently into the InAs quantum dots. The maximum output power of the laser system was 1 W and tunable by a variable attenuator. The diameter of the laser spot on the sample surface was set to 5 mm in order to excite the whole sample. Furthermore, a laser shutter system was added to the set-up that was triggered by the respective beamline experimental control. This system permitted to record diffraction curves of the sample in the excited and non-excited state within a single XRD measurement by taking the data points twice each with opened and closed laser shutter. The sample was mounted onto a cold finger inside of a liquid helium continuous-flow cryostat. The optical activity of the sample was detected by a set of two infrared coated achromat lenses and analyzed by a USB spectrometer.

In a first step the thermal expansion behavior of the QD and GaAs sample was inspected. The thermal expansion behavior of both samples was yielded by determining the absolute lattice constant $a$ along the [001] crystal direction from the GaAs(002), GaAs(004), and GaAs(006) Bragg reflection in the temperature range of 300 K - 600 K. The measurements were carried out with a furnace installed in a laboratory diffractometer in $\theta - \theta$ geometry, which was equipped with a closed x ray tube emitting Cu $K_\alpha$ radiation of 8.048 keV photon energy. The relative change of the perpendicular lattice constant $\Delta a/a_\mathrm{s}$ was evaluated in respect to the lattice constant at $T = 300$ K and is shown in the inset of Figure 1. No difference in lattice expansion is found between the QD sample and the bulk GaAs wafer verifying that the crystal lattice of both samples exhibits identical thermal properties. Compared to the relative thermal expansion expected from the thermal expansion coefficient of GaAs (gray line), the observed thermal expansion behavior differs only slightly. Thus, the thermal lattice expansion of the QD sample complied to that of bulk GaAs and was unaffected by the embedded quantum dots.

Following, we have investigated the lattice expansion under laser irradiation for these samples along the [001] and [100] crystal direction as a function of the laser excitation power density $P$. Utilizing the cryostat set-up, this was realized by high-resolution XRD measurements of the GaAs(002) and GaAs(200)

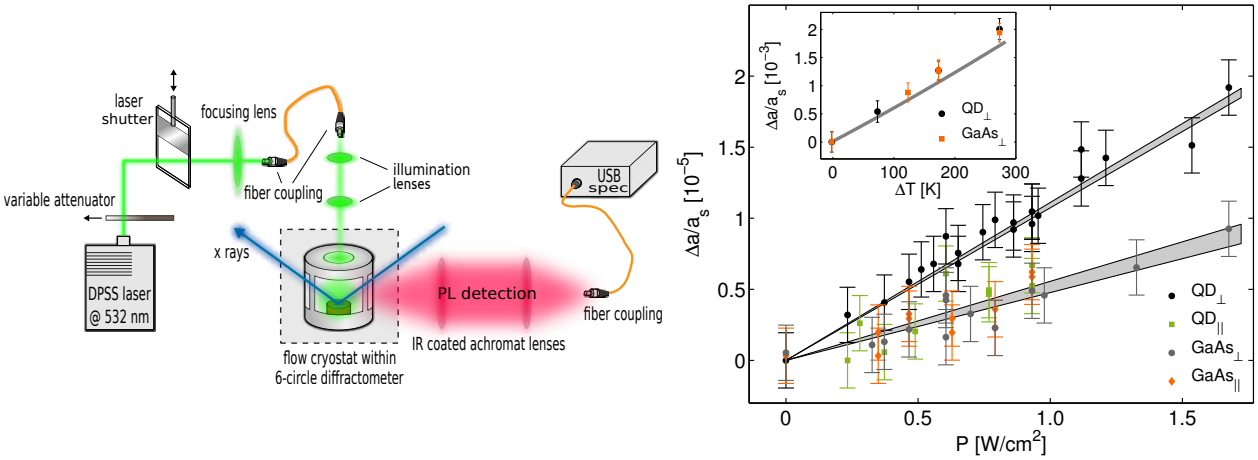


**Figure 1:** Left: Schematic drawing of the experimental set-up. Right: Dependence of the relative lattice expansion along [001] ($\perp$) and [100] ($||$) crystal directions on the laser excitation power density. The inset shows a comparison of the thermal expansion of the QD and GaAs reference sample.

Bragg reflection. The measurement of the GaAs(200) Bragg reflection was conducted under a grazing incidence angle of $\alpha_i = 0.5°$ corresponding to a scattering depth of $\Lambda \approx 70$ nm. The sample temperature was $T = 100$ K and the photon energy $E = 12.38$ keV. The relative change of the lattice constant was obtained from determining the laser-induced shift of the respective Bragg reflection for different excitation power densities yielding thereby $\Delta a/a_s(P)$ values. The corresponding results of these measurements are shown on the right hand side of Figure 1. Note that the excitation power densities are corrected for the reflectivity of GaAs.

Regarding the results of the GaAs sample, the same linear dependence of the relative lattice expansion on the laser excitation power density is found for both the [001] and [100] crystal direction. The lower gray shaded area denotes the $2\sigma$-range of the corresponding linear fit to the GaAs data for both the [001] and [100] direction. Hence, the laser irradiation of the GaAs reference sample caused an isotropic i. e. thermal lattice expansion. In contrast, the QD sample is characterized by a strong anisotropic lattice expansion. While the lattice expansion of the QD sample is significantly enhanced in the [001] direction, as shown by the gray shaded $2\sigma$-range of the linear fit to the corresponding data, it is similar to that of the GaAs reference in the [100] crystal direction. The latter fact suggests for the QD sample thermal lattice expansion in the plane of the [100] crystal direction. This is supported by taking into account the slightly different masses i. e. heat capacities of the QD and GaAs sample. Thereby, the lattice expansion in the [100] direction becomes identical for both samples. Thus, these facts strongly support the existence of thermal lattice expansion in the case of the QD sample that is of the same magnitude as for the bulk GaAs reference.

We attribute the observed anisotropic lattice expansion of the QD sample to an uniform thermal expansion that is superimposed by lattice strain originating from electron-hole pairs, i. e. generation of polaronic states in the InAs quantum dots. The strength of this tetragonal distortion of the crystal lattice in [001] direction amounted to $\Delta a/a_s(P) = (0.5 \pm 0.12) \cdot 10^{-5}\text{cm}^2/\text{W} \cdot P$. This effect was found in the whole crystal that was accessible by the x ray scattering volume extending thereby several $\mu$m into the GaAs lattice beneath the quantum dot layers.

**Acknowledgment.** The DELTA and HASYLAB staff is acknowledged for providing synchrotron radiation. S. T. and F.J. W. thank the NRW Forschungsschule 'Forschung mit Synchrotronstrahlung in den Nano- und Biowissenschaften' for financial support. J. M. thanks the BMBF (05K10PEC) for financial support.

## References

[1] F. Henneberger, O. Benson, Semiconductor Quantum Bits (World Scientific, Singapore, 2008). [2] P. Borri et al., *Phys. Rev. Lett.* **87**, 157401 (2001). [3] P. Borri et al., *Phys. Rev. Lett.* **91**, 267401 (2003). [4] A. Vagov et al., *Phys. Rev. B* **66**, 165312 (2002).

# Forming of intermetallic phases at the interface of steel –aluminium compounds

M. Windmann[1,*], A. Röttger[1], W. Theisen[1]
[1]Lehrstuhl Werkstofftechnik, Ruhr-Universität Bochum, Universitätsstraße 150, 44801 Bochum, Germany
*e-Mail: windmann@wtech.rub.de

To meet the requirements of lowering $CO_2$ emissions by reducing fuel consumption and a simultaneously high crash safety in the automotive industry, emphasis has been put on the development of new material concepts as well as new joining methods [1-2]. One promising strategy to fulfill the aforementioned aim is to use high-strength steel. However, the formability of these steels decreases as the material strength increases, promoting the appearance of material defects (cracks, corrugation, stretcher strain marks) during cold stamping. This problem can be avoided by the use of ultrahigh-strength steels, such as boron-alloyed steel (22MnB5), which can be processed by direct press-hardening. To prevent strong oxidation of the steel sheets during austenitization at temperatures of 880 to 950°C, a protective Al-base pre-coating is commonly deposited on the steel sheets by hot dipping [3]. The protective effect of this Al-base coating is attributed to the formation of a thin and dense $Al_2O_3$ layer [4]. During the hot dipping and austenitizing processes, diffusion processes occur at the interface between the steel substrate and the Al coating, resulting in the formation of intermetallic $Al_xFe_y$ phases at the interface. The formation of these $Al_xFe_y$ intermetallics is strongly influenced by the chemical composition of the Al bath, coating thickness, as well as by the dwell time and the austenitizing temperature prior to stamping. On this account, mechanical as well as physical properties of the respectively phases in the AS protection coating can be adjusted by the aforementioned parameters. Especially, the combination of low fracture toughness and high hardness of these Al-rich intermetallics promote the formation and propagation of cracks. Partially micro-delamination of the hard coating leads to a stronger wear of the press-hardening tool.

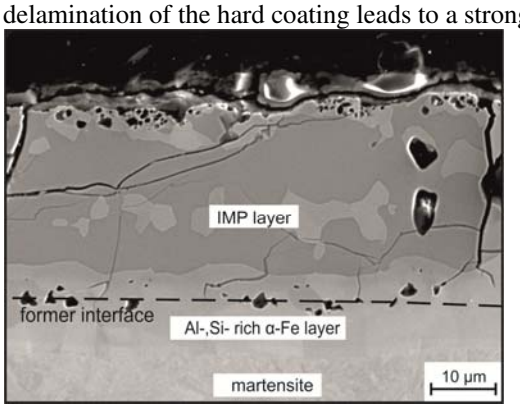


Fig.1: Microstructure of Fe-Al-compound in press hardened state

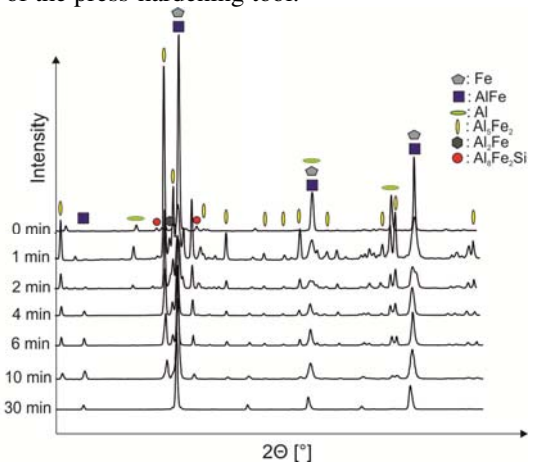


Fig. 2: Diffraction patterns of the Al-base coating in the initial state and in heat-treated condition.

To fulfill the requirements concerning a sufficient oxidation resistance and a simultaneously high durability of the deforming tools, an adapted phase composition in the AS-coating microstructure should be present. One strategy to reduce the crack density in the coating is stabilization of tougher and softer $Al_xFe_y$ intermetallics to avoid brittle and hard phases of type $Al_5Fe_2$ and $Al_2Fe$, which are often found in these Al-base coatings in the press-hardened state [5]. The AlFe and $AlFe_3$ phases should be mentioned at this point because they possess a lower hardness of 300 to 650 HV0.05 and a simultaneously higher fracture toughness up to 26 $MPam^{0.5}$ [6,7]. With respect to the stoichiometry of those phases, the tougher and softer $Al_xFe_y$ intermetallics have a higher Fe content; thus they can be stabilized by more distinct diffusion processes. The aforementioned phase formation and therefore beneficial mechanical properties of the $Al_xFe_y$ intermetallics can be influenced by the temperature and dwell time during austenitization as well as by the chemical composition of the Al bath. This work deals with the investigation of phase formation during austenitization of steel 22MnB5 (1.5528) hot-dipped with an AlSi10Fe3 (140 g/m³) coating. Phase formation was investigated by ex-situ diffraction measurements with synchrotron radiation ($\lambda$= 0.45919 Å) at Delta BL9. Sheets of steel 22MnB5 were coated with an AlSi10Fe3 layer, heat-treated for different dwell times and then water-quenched.

After hot dipping, three intermetallic phases, namely $Al_8Fe_2Si$, $Al_5Fe_2$, and $Al_2Fe_3Si_3$, were detected in a metal matrix of pure aluminum (***Figure 2)***. Identification of the $Al_8Fe_2Si$ and $Al_5Fe_2$ phases was carried out via synchrotron measurements, and the $Al_2Fe_3Si_3$ phase was verified by means of EBSD investigations.

Silicon exerts a major influence on phase formation in iron/aluminum couples by inhibiting the growth of the $Al_5Fe_2$ phase as a result of occupying vacancies in the $Al_5Fe_2$ lattice [8]. During heating up to austenitization temperature, intensive iron diffusion occurs from the steel substrate into the liquid Al-base layer, leading to the solidification of the $Al_8Fe_2Si$ phase at the steel/coating interface. Further diffusion of iron into the previously formed $Al_8Fe_2Si$ layer supports $Al_5Fe_2$ formation in the solid state.

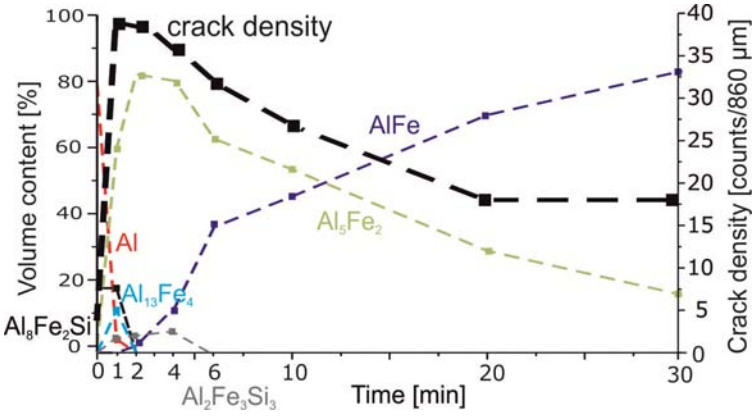


Fig. 3: Evolution of the volume fraction of $Al_xFe_y$ intermetallics and the crack density as a function of dwell time in the Al-base coating

After transformation of $Al_8Fe_2Si$ into $Al_5Fe_2$ due to intensive iron diffusion, $Al_2Fe_3Si_3$ precipitates were formed as a result of the low solubility silicon in $Al_5Fe_2$. The volume fraction of the phases in the AS-coating as a function of dwell is shown in ***Fig. 3***. These results were obtained based on knowledge of the phases in the coating microstructure previously determined by EBSD. The formation of $Al_xFe_y$ intermetallics within the first two minutes can be described schematically by:

$$Al + Al_8Fe_2Si \rightarrow Al_5Fe_2 + Al_2Fe_3Si_3$$

After two minutes, the specimens reached the target austenitization temperature of 920°C. The Al-base coating was completely transformed into binary or ternary intermetallic phases of type $Al_5Fe_2$ and $Al_2Fe_3Si_3$. At this point, solid-state diffusion of aluminum from the Al-base coating into the steel substrates becomes more active. This statement is corroborated by the work of I. Zerner and H. Bakker, who found a higher diffusion coefficient for aluminum in the $Al_xFe_y$ intermetallics compared to that of iron [6]. Between a dwell time of 2 and 6 min, previously formed phases of type $Al_5Fe_2$ and $Al_2Fe_3Si_3$ transformed into AlFe. The $Al_5Fe_2 \rightarrow$AlFe transformation is attributed to an enrichment of the iron concentration in the Al-base coating due to strong diffusion of aluminum into the steel substrate. Based on this behavior, the AlFe phase becomes more stable owing to more pronounced aluminum diffusion into the steel substrate. The $Al_2Fe_3Si_3$ phase, which is localized in the middle of the Al-base coating, also transformed into AlFe as a result of a high solubility of 16 at.-% for silicon in the phase of type AlFe [9]. In this respect, we quantified a silicon content of 12 at.-% in the AlFe phase by EDS investigations. After a dwell time of 6 min, the coating consisted of $Al_5Fe_2$ and AlFe phases. As the dwell time increased (t= 10, 20, 30 min), the intensity of the $Al_5Fe_2$ phase measured by means of synchrotron investigations continuously decreased. Microstructural investigations confirmed a continuous reduction of the volume fraction of the $Al_5Fe_2$ phase with a simultaneous increase in the volume fraction of the AlFe phase (***Figure 3***). The amount of AlFe increased due to iron diffusion in the coating and aluminum diffusion into the steel substrate. After a dwell time of 30 min, the coating mainly consisted of the AlFe phase (88 vol.-%) [10].

## References:


[1] W.S. Miller , L. Zhuang, J. Bottema, A.J. Wittebrood, P. De Smet, A. Haszler, A. Vieregge:, Material Science and Engineering A280 (2000), pp. 37-49

[2] S. Busse, M. Merklein, K. Roll, Michael Ruther, Michael Zürn, Inter J Mater Form (2010), Vol. 3, pp. 1059-1062

[3] T. Manzenreiter, M. Rosner, T. Kurz, G. Brugger, R. Kelsch, D. Hartmann, A. Sommer, BHM (2012), Vol. 157 (3), pp. 97-101

[4] Y. Kitajima. S. Hayashi,T. Nishimoto T. Narita, S. Ukai, Oxid Met (2010) 73, pp. 375–388

[5] H. Huh, S.-B. Kim, J.-H. Song, J.-H. Lim, International Journal of Mechanical Sciences 50 (2008), pp. 918-931

[6] I. Zerner, Prozessstabilisierung und Ergebnisse für das Laserstrahlfügen von Aluminium-Stahl-Verbindungen, BIAS-Verlag Bremen (2002)

[7] A. Kubošová, M. Karlík, P. Haušild, J. Prahl, Materials Science Forum Vols. 567-568 (2008), pp. 349-352

[8] G.Eggeler, W. Auer, H. Kaesche, Journal of Materials Science 21 (1986), pp. 3348-3350

[9] T. Maitra, S.P. Gupta, Materials Characterization 49 (2003), pp. 293-311

[10] M. Windmann, A. Röttger, W. Theisen, submitted for publication in Surface & Coatings Technology (2012)

# Structure and ice content of clathrate hydrates

F. J. Wirkert*, H. Nelson, C. Sternemann, M. Paulus, K. Mende, J. Möller, J. Nase, R. Böhmer, M. Tolan

*Fakultät Physik / DELTA, Technische Universität Dortmund, 44221 Dortmund, Germany*

*email: florian.wirkert@tu-dortmund.de

Clathrate hydrates are ice like compounds composed of water and guest molecules, which form at low temperatures and high pressures. They occur, e.g., as methane reservoirs in deep sea regions or in gas pipelines. Clathrate hydrates are studied by means of nuclear magnetic resonance (NMR) to measure the strength of hydrogen bonds and guest-host-interactions [1]. For a better understanding of the results of these measurements, the structure as well as the ice content of the NMR samples should be determined using X-ray powder diffraction.

In the past, tetrahydrofuran clathrate was examined using inelastic X-ray scattering techniques [2]. The intention of a second experiment was to check the existence of temperature dependent structural changes by performing X-ray powder diffraction measurements.

X-ray diffraction (XRD) is a powerful technique to determine the crystal structure of a certain substance [3-6]. In a powder diffraction experiment the incoming beam hits the sample and in an ideal crystalline powder, Bragg's law is fulfilled for any possible Bragg reflection. Thus, by measuring the intensity of the scattered X-rays with a 2D image plate detector, so called Debye rings are observed. The important dependence between the intensity of the scattered beam and the scattering angle $2\Theta$ is obtained by azimuthally integrating the intensity on a 2D image. The resulting diffraction pattern is specific for any substance. For our first experiment, the aim was to determine the ice content in samples that were previously investigated in NMR experiments. Therefore they were placed in a copper sample holder during the measurements, which was mounted at the bottom of a polyoxymethylene trough filled with liquid nitrogen. In order to obtain better results, the whole sample system was rotated. In that way the sample is closer to an ideal powder. In figure 1 the experimental setup at beamline BL9 [7] is shown. A MAR345 image plate detector was used, the energy of the incoming beam was set to 27 keV. Measurements were performed with the hydrate samples containing certain guest molecules as well as with the pure guest substances and with ice.

(a) Whole setup mounted at the six circle diffractometer.

(b) Closer look at the sample cell.

**Figure 1:** Experimental setup to investigate different NMR samples.

The second experiment was performed using a setup for temperature control, as shown in figure 2. Tetrahydrofuran (THF) hydrate powder was produced using mortar and pestle at low temperature in a liquid nitrogen bath. The powder sample was filled in a copper made sample cell with kapton windows, which then was placed into the temperature controled sample cell. Diffraction measurements were performed in a temperature range from 260 K to 278 K.

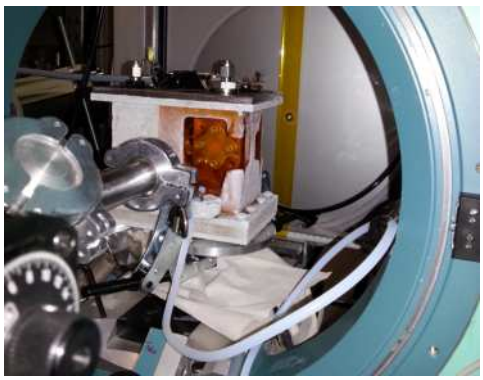

**Figure 2:** Experimental setup for temperature controled measurements.

The diffraction patterns were analysed using the programs *GSAS* [8, 9] and *POUDRIX* [10] after background subtraction. Comparison with theoretical values [11] shows the existence of structure SII hydrate and structure Ih ice in every sample, see figure 3(a). Those samples containing dioxane and tetrahydropyran also show peaks proving the existence of crystalline guest substance. With the detailed information on THF hydrate structure [11] the ice content in the THF containing sample could be determined to 13±3 wt%. The analysis is still in progress, in order to determine the ice content in the other samples.

During the second experiment, no temperature induced structural changes, except ice melting, were observed, see figure 3(b). The different peak shapes are caused by the existence of rather big crystallites in the sample, inducing unregularities in the Debye rings. To examine whether there are temperature induced structural changes or not, the temperature range has to be increased and the sample preparation needs to be improved.

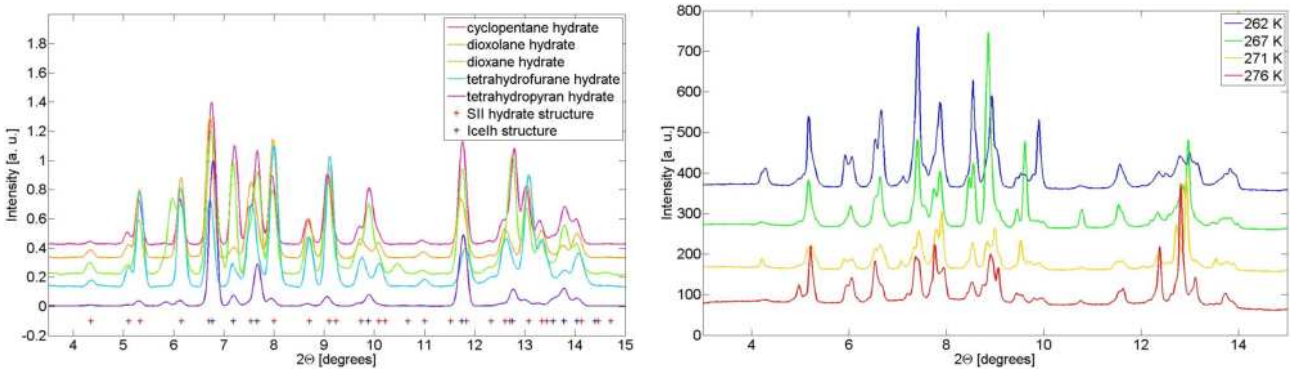


(a) Different guest molecules.

(b) THF hydrate at different temperatures.

**Figure 3:** Diffraction patterns of both experiments.

The authors acknowledge the DELTA machine group for providing synchrotron radiation and technical support. FJW likes to thank NRW Forschungsschule for financial support. HN is grateful to the DFG (BO 1301/7) for financial support. KM and JM thank BMBF (05K10PEC) for financial support.

## References

[1] H. Nelson et al., *Deuteron nuclear magnetic resonance and dielectric study of host and guest dynamics in KOH doped tetrahydrofuran clathrate hydrate*, Phys. Rev. B **81** (224206/1-10), 2010

[2] F. Lehmkühler et al., *Temperature-Induced Structural Changes of Tetrahydrofuran Clathrate and of the Liquid Water/Tetrahydrofuran Mixture*, J. Phys. Chem. C **115** (21009-21015), 2011

[3] W. H. Bragg, W. L. Bragg, *The Reflection of X-rays by Crystals*, Proc. R. Soc. Lond. A **88** (428-438), 1913

[4] P. Debye, P. Scherrer, *Interferenzen an regellos orientierten Teilchen im Röntgenlicht*, Nachr. Ges. Wiss. Göttingen, Mathematisch-Physikalische Klasse (1-26), 1916

[5] R. Allmann, *Röntgenpulverdiffraktometrie*, Springer, 2003

[6] H. Krischner, B. Koppelhuber-Bitschnau, *Röntgenstrukturanalyse und Rietveldmethode*, Vieweg, 1994

[7] C. Krywka et al., *The small-angle and wide-angle X-ray scattering set-up at beamline BL9 of DELTA*, J. Synchrotron Rad. **14** (244-251), 2007

[8] A. C. Larson, R. B. von Dreele, *General Structure Analysis System (GSAS)*, Los Alamos National Laboratory Report LAUR **86-748**, 2004

[9] B. H. Toby, *EXPGUI, a graphical user interface for GSAS*, J. Appl. Cryst. **34** (210-213), 2001

[10] *http://www.ccp14.ac.uk/tutorial/lmgp/poudrix.htm*

[11] C. Y. Jones et al., *Structure and Thermal Expansivity of Tetrahydrofuran Deuterate Determined by Neutron Powder Diffraction*, J. Phys. Chem. B **107** (6026-6031), 2003

# In-situ monitoring the phase transitions and formations in Li-air batteries

Swapna Ganapathy[1], Ralph Wagner[2], Dirk Lutzenkirchen-Hecht[2], Brian Adams[3], Linda Nazar[3] and Marnix Wagemaker[1]

[1] Delft University of Technology, The Netherlands

[2]Wuppertal University, Germany

[3]Waterloo University, Canada

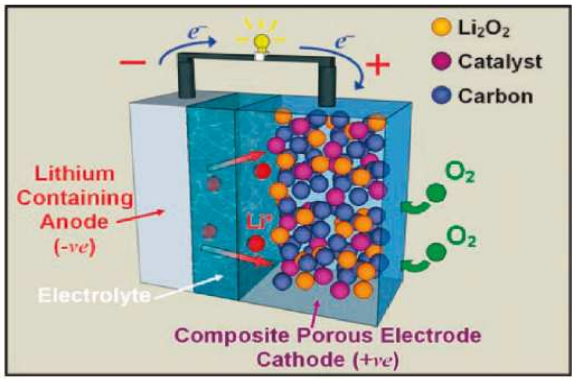


Figure 1: Schematic of a Li-$O_2$ battery. (A. Debart Angew Chem Int Ed 2008)

Though fundamental research into Li-air or Li-$O_2$ batteries is still in its infancy, it's the lure of its potential applicability in electric vehicles that has led to frenzied interest in this field. A Li-$O_2$ cell consists of a Li or a Li-containing anode, a gas diffusion cathode made of a porous carbon and catalyst composite allowing an inflow of $O_2$ gas and a Li-salt containing electrolyte. The cell reactions can be broadly classifies as the oxygen reduction reaction (ORR) which takes place on discharge leading to the formation of $Li_2O_2$ on the surface of the carbon composite cathode. On charge the so called oxygen evolution reaction (OER) takes place wherein the $Li_2O_2$ decomposes into its constituent Li and $O_2$ gas. There are several issues that impede the performance and functioning of this cell which include electrolyte decomposition by oxygen radical species leading to the

formation of $CO_2$ gas in addition to $Li_2CO_3$ on the cathode surface, the large overpotentional that arises during charge due to cathode resistance to name a few.

Recently it was found that use of carbon in combination with selected catalysts lead to the formation of $Li_2O_2$ on cell discharge with a toroidal morphology whose coverage on the carbon cathode is non-uniform. More interesting is that these toroids breakdown very early on in the charge half of the battery cycle. We are looking for subtle changes in lattice parameters of $Li_2O_2$ on charge which breaks down via a superoxide intermediate with bond length changes in the order of 0.2 Å. This is the main purpose of these experiments. Our measurements in October allowed us to visualize the formation of $Li_2O_2$ *in situ* during discharge, in addition to side products of LiOH and $Li_2CO_3$ formed. These preliminary experiments were performed on a cell with oxygen and a carbon only cathode, a Li-metal anode and an ether based electrolyte in a home-built transmission cell. The idea was to be able to estimate if we would be able to see lithium peroxide as it formed during discharge. The experiment was successful allowing us to visualize *in situ* for the first tine the formation of $Li_2O_2$ during discharge in a Li-$O_2$ cell as shown in Figure 2.

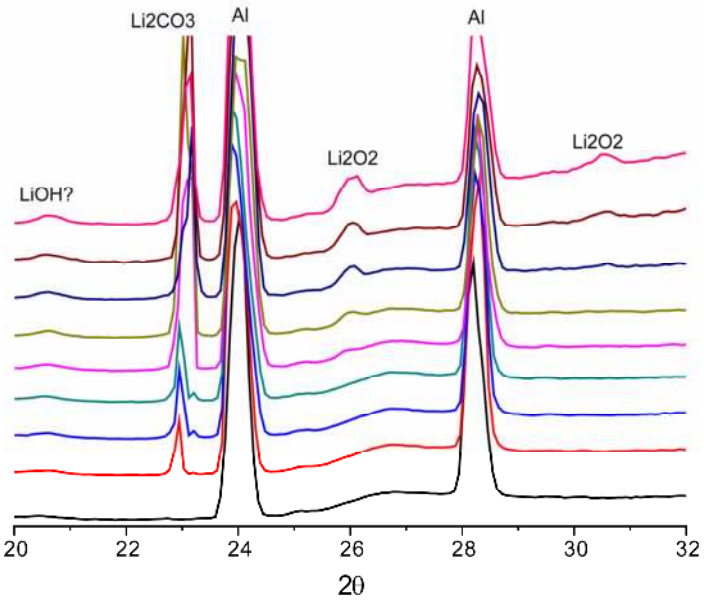


Figure 2: Integrated diffraction patterns recorded intermittently *in situ* during discharge of a Li-$O_2$ cell.

# Structural characterization of polygermane networks

I. Brinkmann[1], C. Sternemann[1], M. Paulus[1], P. Degen[2], K. Mende[1], A. Nyrow[1], S. Balk[3], H. Rehage[2], and M. Tolan[1]

[1]Fakultät Physik / DELTA, Technische Universität Dortmund, D-44221 Dortmund, Germany

[2]Fakultät Chemie, Technische Universität Dortmund, D-44221 Dortmund, Germany

[3]Fachbereich C – Abteilung Physik, Bergische Universität Wuppertal, D-42097 Wuppertal, Germany

Networks build of silicon oxides are promising candidates to form nanocapsules for application in nanotechnology and medicine, e.g. drug transport [1-4]. Here, we study the capabilities of polygermanates ($C_6H_5GeO_{1.5}$) to form two-dimensional networks. Therefore, two different routes to synthesize such polygermanates (POGs) were used: i) bulk samples: Phenyltrichlorogerman ($C_6H_5GeOCl_3$) was mixed with isooctan and small amounts of water. Then the mixture was stirred until precipitation of 3D-polymerized POG. ii) 2D samples: Polymerization of POG at the air/water interface was achieved by spreading of PTG solved in $CHCl_3$. For polymerization at the oil/water interfaces the water phase was covered by p-xylene containing the PTG. Samples were transfered from the interface (by LB technique), filtered, washed and finally dried to extract POG powders. To characterize the polymerized POG samples and to distinguish 2D and 3D polymerization x-ray diffraction and x-ray absorption spectroscopy was used.

X-ray absorption spectra were measured in fluorescence detection at beamline BL8 [5] using the Si 111 double crystal monochromator for energy scans at the Ge K-edge both in the XANES (x-ray absorption near edge structure) and in the EXAFS (extended x-ray absorption fine structure) region. The XANES spectra are shown in Figure 1 a) in comparison to a germanium dioxide reference spectrum. No significant differences between bulk and 2D samples are observed which indicates also 3D polymerization when prepared at the liquid/air interface. Distinct oscillations in the XANES favor a crystalline structure of both sample types. For a detailed analysis the EXAFS spectra were analyzed and the weighted Fourier transform is presented in Figure 1 b). There are strong features (marked by dots) not only due to the first coordination shell (Ge-O distance) which confirms a well defined second order coordination pointing towards long range order also for 2D samples. The synthesis route seems to have only weak impact on the structure of the POG. The analysis is still in progress to search for adequate structural models of polymerized POG.

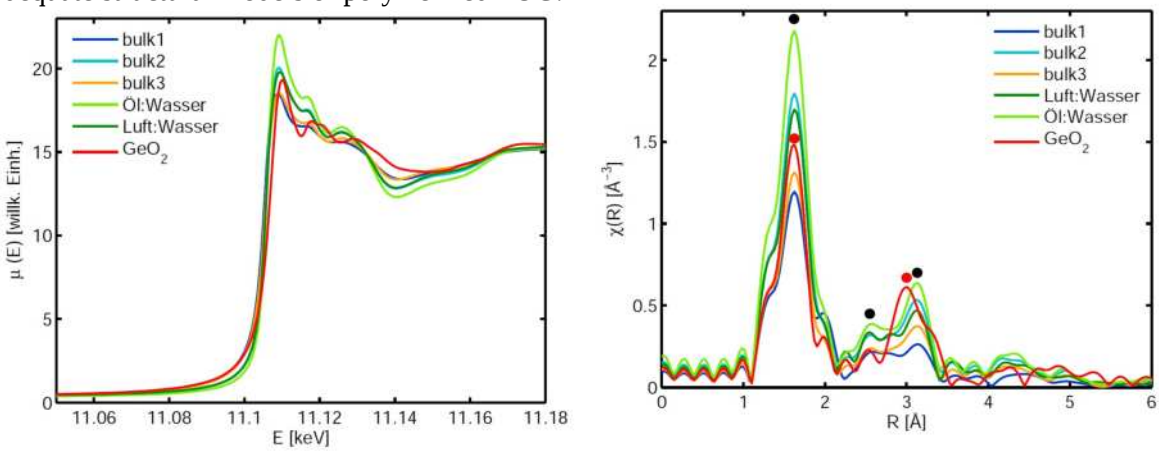


*Figure 1: a) left: XANES spectra of polymerized POG 2D (green) and bulk samples (blue/orange) compared with a germanium dioxide reference (red). b) right: Fourier transform of the weighted EXAFS function of bulk and 2D samples showing clear peaks for first and higher coordination shells.*

X-ray diffraction experiments to analyze the amorphous or crystalline 3D/2D structure of POG samples were performed at beamline BL9 [6] of DELTA employing a Pilatus 100K detector at an incident x-ray energy of 15.2 keV. The corresponding diffraction patterns are presented in Figure 2.

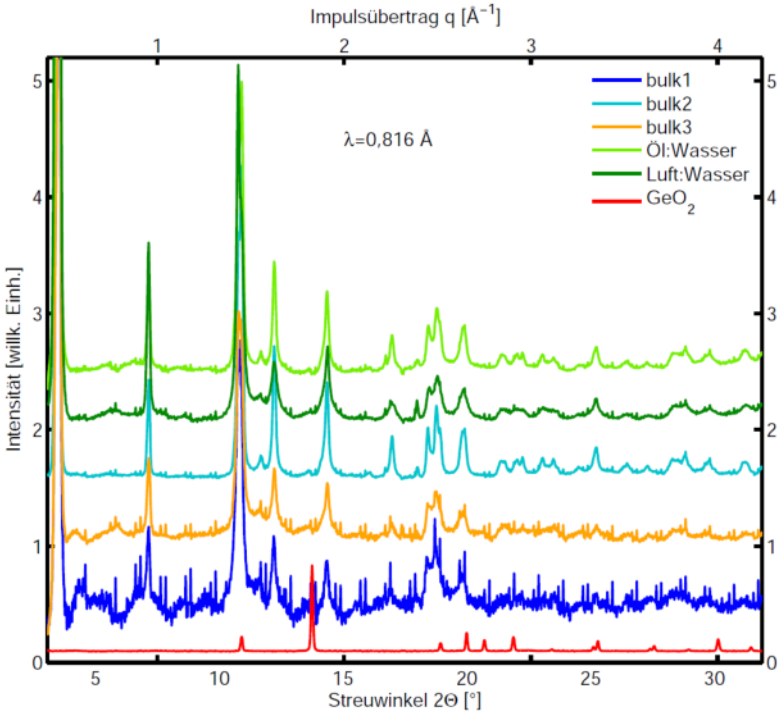


*Figure 2: X-ray diffraction patterns of bulk and 2D POG samples. Germanium dioxide is shown as a reference. Crystalline order can be observed for both synthesis routes, i.e. for bulk and 2D samples.*

In contrast to polysilane (POS) samples, which show only one distinct correlation peak indicating a typical Si-O-Si-O distance in favor of building up 2D networks and POS nanocapsules, the POG samples show crystalline order, also when synthesized at the liquid/air interface.

Due to the shorter hydrocarbon chains of POG compared to POS crystallization takes place independently on the route of synthesis. This makes it difficult to produce POG nanocapsulses or 2D networks using interface polymerization at conditions investigated in this work, which hinders the application of POGs for nanocapsule production as long as only short chain POGs are available.

## Acknowledgement

We would like to thank DELTA for providing synchrotron radiation. KM and AN are supported by BMBF 05K10PEC.

## References

[1] T. K. Jain, M. A. Morales, S. K. Sahoo, D. L. Leslie-Pelecky and V. Labhasetwar, Mol. Pharm. **3**, 194 (2005).
[2] C. C. Berry, J. Phys. D: Appl. Phys. **42**, 224003 (2009).
[3] X.-H. Peng, X. Qian, H. Mao, A. Y. Wang, Z. Chen, S. Nie and D. M. Shin, Int. J. Nanomed. **3**, 311 (2008).
[4] A.V. Jovanovic, J.A. Flint, M. Varshney, T.E. Morey, D.M. Dennis, and R.S. Duran, Biomacromolecules **7**, 945 (2006).
[5] D. Lützenkirchen-Hecht, R. Wagner, U. Haake, A. Watenphul, and R. Frahm, J. Synchrotron Rad. **16**, 264 (2009).
[6] C. Krywka, M. Paulus, C. Sternemann, M. Volmer, A. Remhof, G. Nowak, A. Nefedov, B. Pöter, M. Spiegel, and M. Tolan, J. Synchrotron Rad. **13**, 8 (2006).

# EXAFS investigations on the temperature dependent structural properties of gold nanoparticles

K. Blech[1], U. Simon[1], D. Lützenkirchen-Hecht[2], R. Wagner[2], R. R. Frahm[2]

[1]RWTH Aachen University, Institute of Inorganic Chemistry, 52056 Aachen, Germany
[2]Universtiy of Wuppertal, Dep. of Physics-Condensed Matter, 42097 Wuppertal, Germany

The charge transport of gold nanoparticles (AuNP) with a diameter of 4.1 ± 0.5 nm has been investigated by impedance spectroscopy [1]. In the temperature range 230-290 K an atypical charge transport behavior was found expressed by a sharp peak in the Arrhenius plot. Additionally temperature dependent transport measurements on single AuNP exhibited a similar transport behavior. For further analysis of this unexpected finding we performed DSC measurements which showed an endothermal process in the same temperature range as the peak in the Arrhenius plot occurred. High-resolution TEM analysis showed facetted, crystalline particles which are multiply-twinned. Temperature dependent XRD measurements resulted in a broadening of the (200) reflex and a shift of the (111) reflex to higher 2Θ values. Due to these results a possible explanation might be that the AuNP undergo a morphological transition (decahedral to icosahedral) with temperature. This could effect a reorganization of the ligand shell and therefore causing a distinct step in conductivity. Such a transition has already been predicted theoretically and a phase map of AuNP has been created based on relativistic *ab initio* thermodynamics published by *Barnard et al.* [2]. This modified phase map is presented in Fig. 1.

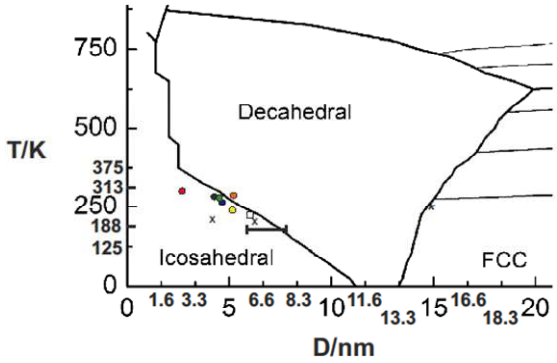


| symbol in phase map | Partide size in nm | Ligand | Transition Temp. in K | Reference |
|---|---|---|---|---|
| ● | 2.6 | FcC3 | 310 | |
| x | 4.0 | MSA | 206 | Sreekumaran et al. PCCP 2009 |
| ● | 4.1 | BP3 | 280 | |
| ● | 4.3 | C8 | 290 | |
| ● | 4.5 | C12 | 260 | |
| ○ | 5.1 | C12 | 240 | |
| ● | 5.2 | C18 | 290 | |
| □ | 6.0 | C9-dithiol | 218-230 | Brust et al. Langmuir 1998 |
| ⟷ | 6.0-8.0 | C5-dithiol | 181 | Fishelson et al. Langmuir 2001 |
| x | 6.2 | MSA | 200 | Sreekumaran et al. PCCP 2009 |
| ★ | 15.0 | Cysteamin | 250 | Koplin Dissertation 2006 |

**Fig. 1:** Modified phase map from Lit. [**Fehler! Textmarke nicht definiert.**], in which the temperature ranges corresponding to the atypical behavior our nanoparticle-ligand-systems and systems known from literature are inserted.

This hypothesis is supported by appearance of the same atypical feature in the charge transport behavior of all our investigated nanoparticle-ligand-systems independently from the type of the stabilizing ligand molecules. Additionally Fig. 1 contains data of electrical characterizations measured by other groups known from literature which denote the temperature of the atypical temperature dependent properties and which hence support our hypothesis. By performing temperature dependent EXAFS experiments inter-atomic distances and local atomic reorganizations in AuNP will be accessible in order to verify or falsify our hypothesis of structural transition.

EXAFS measurements were performed on BL 8 in transmission at 11-13 keV (Au-$L_3$-edge). The samples were cooled with liquid nitrogen and in the temperature range 100-300 K EXAFS scans were carried out. The challenge during these experiments was the adjustment of the temperature. While performing the EXAFS scans the temperature increased due to the evaporating nitrogen. The Fourier-transformed EXAFS spectra are shown in Fig. 2.

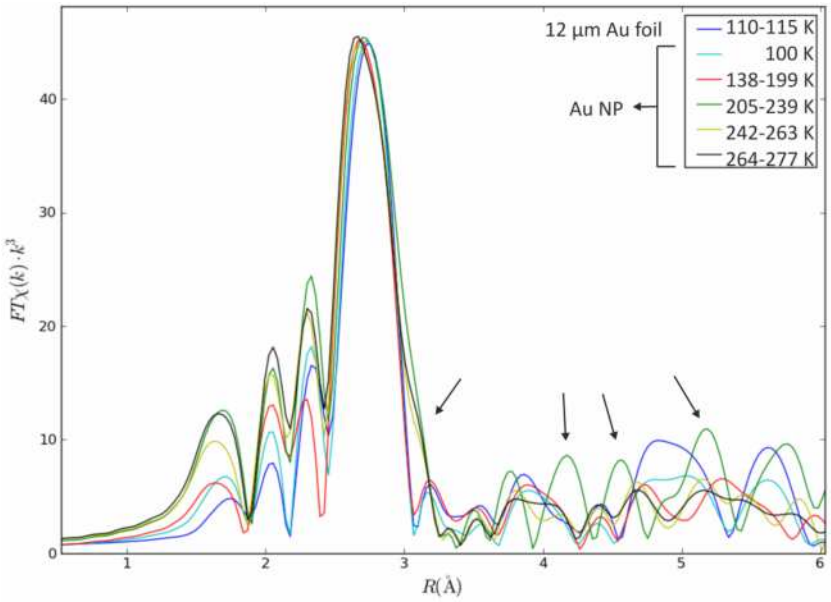


**Fig. 2:** Fourier-transformed EXAFS spectra of the reference (12µm Au foil) and the AuNP at different temperatures. The arrows point at the change in the structural features of AuNP at 205 K at inter-atomic distances of R ≈ 3Å and R ≈ 4-6Å.

At 100 K the spectra of the Au foil and the AuNP (deep blue and light blue curve) are nearly identical in the inter-atomic distances *R*. At 205 K the curve progression suddenly changes which is highlighted with arrows at inter-atomic distances $R \approx 3$Å and $R \approx$ 4-6Å. These results indicate that a structural change in the AuNP with respect to the inter-atomic distances at a characteristic temperature is evident are consistent with our hypothesis of a morphological transition. A detailed analysis is still ongoing to clarify the observed differences in the EXAFS spectra dependent on the temperature. A further step is the calculation of the EXAFS data for icosahedral/decahedral particles and the comparison with the obtained data.

Based on the results from the detailed analysis a repetition of these experiments is essential with a cooling system allowing a stable adjustment of the temperature. Thereby a more precisely analysis of the atomic structure and the coordination shell of the AuNP is possible.

We thank the BL 8 crew and the DELTA machine group for providing synchrotron radiation and for technical support.

**References:**

[1] M. Manheller, S. Karthäuser, R. Waser, K. Blech, U. Simon, *J. Phys. Chem. C.*, **2012**, *116*, 20657-20665.

[2] A.S. Barnard, N.P. Young, A.I. Kirkland, M.A. van Huis, H. Xu, ACSNano **2009**, *3*(6), 1431-1436.

# Extended X-ray absorption fine structure (EXAFS) Investigation of iron incorporation during $Kr^+$ ion beam sputtering on Si (100)

**B. Khanbabaee[1], M. Engler [2], R. Wagner[3] , D. Lützenkirchen-Hecht[3], and U. Pietsch[1]**

[1] Solid State Physics, Siegen University, 57068 Siegen, Germany

[2]II. Physikalisches Institut, Universität zu Köln, Zülpicher Straße77,D-50937 Cologne, Germany

[3] Fachbereich C Physik, Bergische Universität Wuppertal, GaußStr. 20,42097 Wuppertal

The bombardment of solid surfaces with energetic ions can be used for the fabrication of self-organized structures on surfaces [1]. It was shown that different types of patterns on the nanoscale, i.e. dots, ripples and relief pattern can be generated by varying the experimental parameters such as ion energy, fluence, ion incidence angle and the use of different ion species (Ar+, Kr+, Xe+) [2]. A number of experimental studies have shown that the simultaneous co-deposition of foreign atoms, in particular metal atoms like Fe and Mo, during ion beam erosion has tremendous influence on self-organized nano-pattern formation. Recent studies have shown that for normal and near normal ion incidence, pattern formation appears only if metal impurities like Fe or Cr are incorporated on the surface during the sputtering process [3-6]. At present, many aspects of the influence of co-deposited metal atoms are not fully understood. However one of the key points for further structural understanding is the investigation of the layer just below the surface in which the influence of incorporated Fe atoms dominates further the patterning process.

We investigate the influence of iron incorporation while 2 keV $Kr^+$ ion beam erosion of Si surfaces under normal ion incidence with two different density of $n_{Fe} = (15.1\pm1.1)\times10^{19}\ m^{-2}$ for sample 1 and $n_{Fe} = (4.67\pm0.14)\times10^{19} m^{-2}$ for sample 2. AFM images of the samples show that by increasing the Fe concentration the morphology of the surface transfers from ripples for sample 2 to smooth surface for the sample 1. Considering the low penetration depth of ions we have used extended X-ray absorption fine structure (EXAFS) under grazing-incidence in order to determine the depth profile and phase composition of incorporated iron atoms straight below the surface.

The EXAFS spectra of sample 1 with smooth surface and sample 2 with ripple surface is presented in Fig.1 (a-b), respectively, taken in vicinity of the Fe-K edge at Fe (7112 eV) under grazing incidence angle of X-ray varying from 0.1° to 1°. While the XANES spectra (inset of Fig.1a) of sample 1 are modulated by decreasing the incidence angle of X-ray, no pronounced difference is visible for XANES spectra (inset of Fig.1b) of sample 2. The measured XANES spectra are compared with standard spectra taken for various silicide compounds such as $FeSi_2$ and $Fe_3Si$ [Fig. 4(c)]. A shift toward lower photon energies in the region $\alpha_i << \theta_c = 0.23°$(critical angle of Si) for the sample 1 can be attribute to dominated Fe-rich silicide ($Fe_3Si$) or enrichment of Fe atoms on top surface.

Fig 1.d shows the comparison of XAS spectra of the sample 1 and 2 at X-ray incidence angle of 1° with standard spectra. It can be seen that the XAS spectrum of sample 1 is in good agreement with spectra of Fe or Fe-rich silicide while the XAS spectrum of sample 2 follows the spectrum of FeSi2. This means by increasing the Fe concentration, the Fe-rich silicide formation is dominated at sub-surface area leading to smoothing the surface.

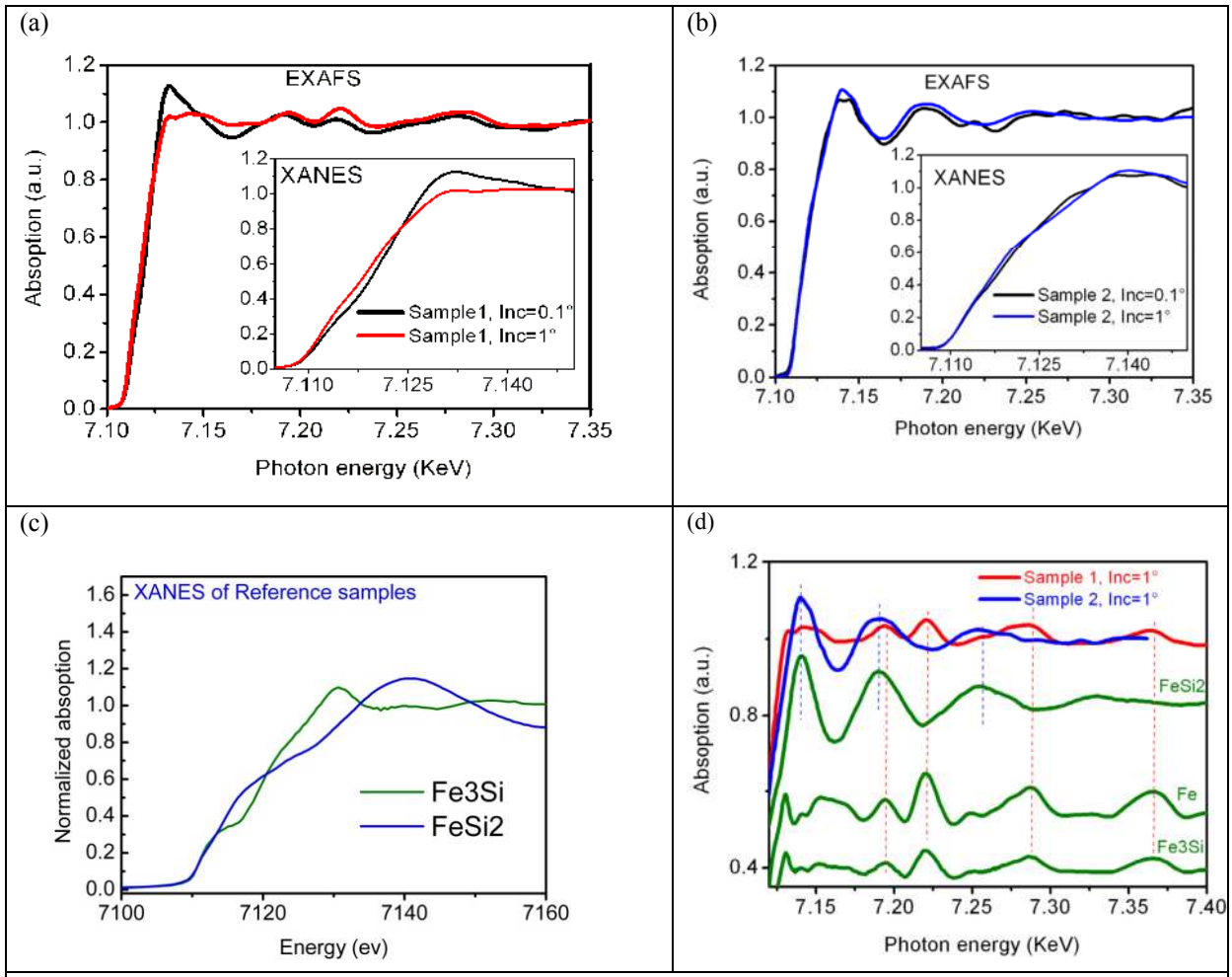


**Figure 4** (a) Normalized XAS spectra of sample 1 at different X-ray incidence angles of 0.1° (black) , 1° (red ). The inset shows the XANES part of spectra. (b) ) Normalized XAS spectra of sample 2 at different X-ray incidence angles of 0.1° (black) , 1° (blue ). The inset shows the XANES part of spectra. (c) Comparison of the normalized XANES spectra at Fe K edge of known reference powder samples.(d) Comparison of the normalized XAS spectra of sample 1 (red) and sample 2 (blue) at x-ray incidence angle of 1 ° with known reference powder samples .

**References** :


[1] W. L. Chan and E. Chason, Journal of Applied Physics 101, 121301 (2007).

[2] B. Ziberi, F. Frost, T. Höche and B. Rauschenbach, Physical Review B 72 (23), 235310 (2005).

[3] G. Ozaydin, K. F. Ludwig Jr, H. Zhou and R. L. Headrick, Journal of Vacuum Science & Technology B: Microelectronics and Nanometer Structures 26, 551 (2008).

[4] S. Macko, F. Frost, B. Ziberi. D. F. Förster, and T. Michely, Nanotechnology **21**, 085301 (2010).

[5] J. Sánchez-García, L. Vázquez, R. Gago, A. Redondo-Cubero, J. Albella and Z. Czigány, Nanotechnology 19, 355306 (2008).

[6] S. Macko, J. Grenzer, F. Frost, M. Engler, D. Hirsch, M. Fritzsche, A. Mücklich and T. Michely, New Journal of Physics 14 (7), 073003 (2012).

# XAS Analysis of ultrasmall gold nanoparticles

**C. Helmbrecht[1], W. Frank[1], D. Lützenkirchen-Hecht[2], R. Wagner[2], R. Frahm[2]**

[1] Anorganische Chemie Strukturforschung, Heinrich Heine Universität Düsseldorf

[2] Fachbereich C – Physik Fachgruppe Materialwissenschaften, Bergische Universität Wuppertal

## 1) Introduction to AuNP

Bulk gold is known as yellow noble metal, but with decreasing size (particles) optical properties change immediately. In the past decades gold nanoparticles with the size of 2 to 100 nm have been well-studied[1-3], especially regarding their plasmon resonance. This occurs in the visible part of the spectrum in contrast to other metals. When the particle size approaches *de Broglie's wavelength* of an electron at the *Fermi energy* optical, electronic and chemical properties are dramatically different from the two size regimes above. These subnanometer-sized gold clusters which consists only of a few atoms show molecular-like behavior, having discrete electronic states and size-dependent fluorescence.[4]

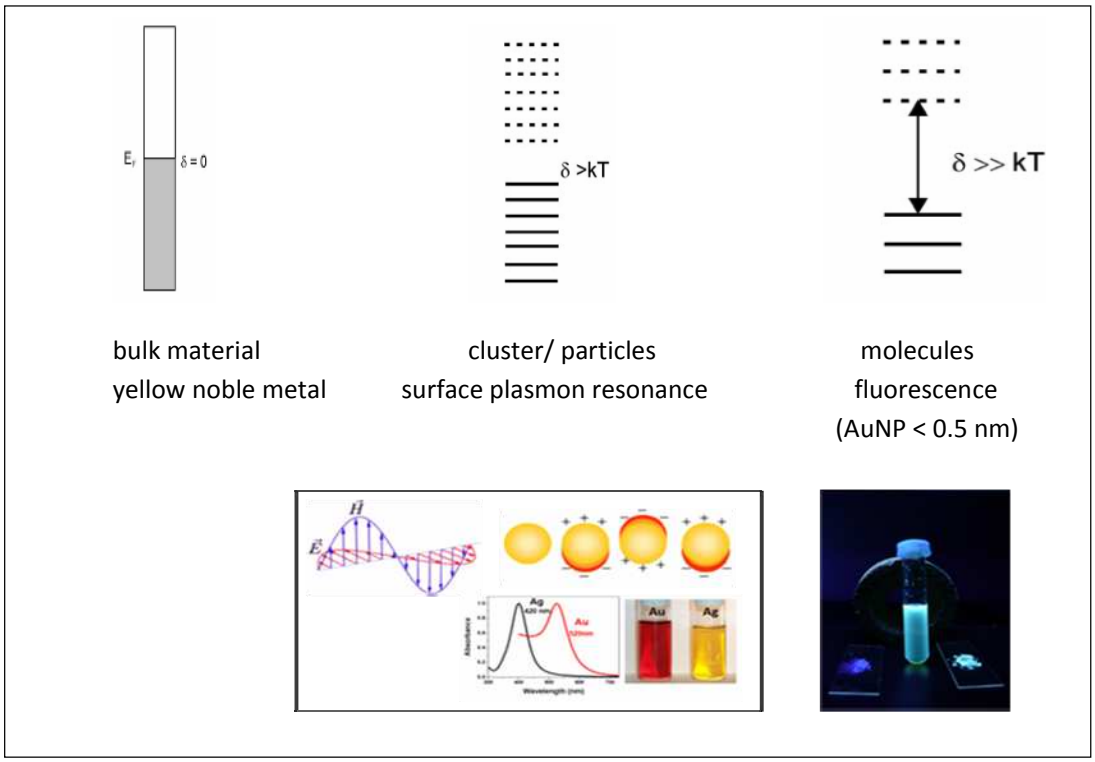


The dependence of emission energy on the number of atoms in each gold nanocluster can be well fit in approximation with the following energy scaling law:

$$\lambda_{Em} = \frac{\varepsilon_F}{\sqrt[1]{N^3}}$$

$\lambda_{Em}$ emission wavelength
$\varepsilon_F$ fermi energy
$N$ number of free electrons

2) Present state of knowledge

We investigate ultrasmall gold nanoparticles (AuNP) with different capping systems like thiols, amines and phosphines. Up to now no exact stoichiometric ratio and no crystal structure were available.

Other analytical methods fail because of low concentration, particle size at the lower measurement limit or the unknown structure. XAS is used to clarify the oxidation state (in literature Au(0) is maintained), furthermore the coordination geometry and the environmental chemistry, especially the nature of the Au-L-bonding.

3) Results of XAS

The following references were measured because theoretical calculations for comparison purposes are nearly impossible due to scarce previous knowledge:

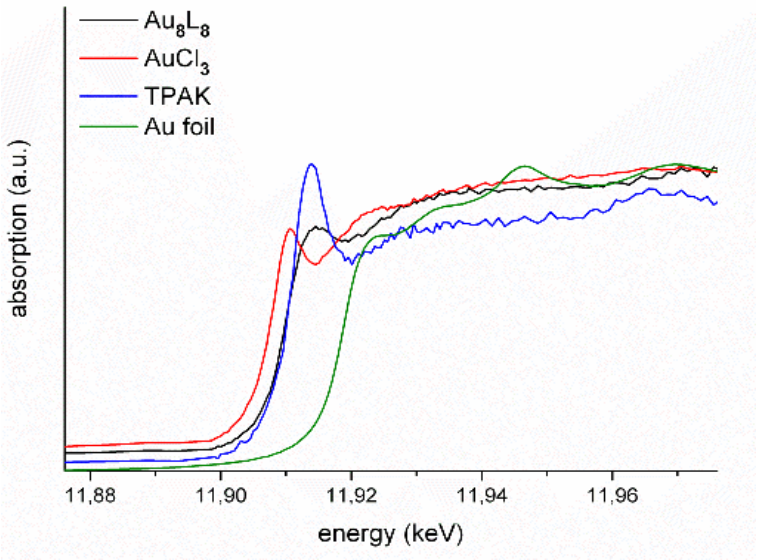


XAS references
Au foil
$AuCl_3$
$Au_8(PPh_3)_8(NO_3)_2 \equiv [Au_8L_8]$

Sample TPAK
AuNP with TPA-ligands with unknown stoichiometric ratio

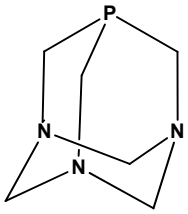


**1,3,5-Triaza-7-phosphaadamantane**

Au $L_3$ edge – XANES spectra for AuNP and different reference compounds

During the measurement no Au(0) was detected instead it points to the existence of mixed-valence species. Furthermore in the 40 eV past the edge the sample and for this reason its structure is similar to the sample of $Au_8L_8$. Additional measurements are indispensable to verify these conclusions and state some predictions about the coordination sphere around the gold core.
For better comparison purposes AuNP with L=$PPh_3$ were synthesized but not measurable. Due to the low concentration of gold in the sample only a very noisy signal in the fluorescence mode was obtained. Possibly a concentration of c(AuNP) ≈ 10 ppm represents the resolution limit.

[1] G. Schmid, B. Corain, *Eur. J. Inorg. Chem.* **2003**, 3081.
[2] M.-C. Daniel, D. Astruc, *Chem. Rev.* **2004**, *104,* 293.
[3] A. Schwartzberg, J. Z. Zhang, *J. Phys. Chem. C*, **2008**, *112*, 10323.
[4] E. Roduner, *Chem. Soc. Rev*. **2006**, *35*, 583.

# Local atomic and electronic structure of Ag clusters deposited in a silica aerogel matrix

S. Hoffmann[a], D. Engemann*, [a], S. Duffe[a], C. Sternemann[a], Stefan Balk[b], R. Wagner[b], H. Hövel[a]

[a] *Experimentelle Physik I / DELTA, Technische Universität Dortmund, 44221 Dortmund, Germany*

[b] *Fachbereich C – Fachgruppe Physik-Materialwissenschaften, Bergische Universität Wuppertal, 42097 Wuppertal, Germany*

∗ email: david.engemann@tu-dortmund.de

In modern material science nanoparticles become more and more important. The properties of this particles can differ widely from that of the corresponding bulk material [1, 2, 3]. So a wide range of new properties like plasmon resonances can be observed when decreasing the size of the condensed matter system. One field of research is cluster science. Here nanoparticles, so called clusters, consisting of only one kind of atoms, in this case silver atoms, are investigated.

For practical applications it is necessary to bring the clusters into contact with surfaces, liquids or matrices like silica aerogel [4]. The clusters can change their properties due to coalesce and chemical interaction with this environment. For example optical properties of noble metal clusters and nanostructures such as their UV-VIS absorption band alter significantly with size, shape and interparticle spacing as well as with the properties of the local environment.

X-ray absorption near edge structure (XANES) spectroscopy yields unique structural and chemical information on supported and embedded Ag clusters. It is well suited to investigate the chemical environment of the Ag clusters and allows the study of changes of the unoccupied density of states (uDOS).

In this report we describe the results of our x-ray absorption near edge structure (XANES) spectroscopy measurements (at BL8, DELTA, using the Si(111) monochromator) at the Ag $L_3$ absorption edge of Ag clusters. The cluster consist of about 250 atoms with a mean diameter of 2R≈2nm and were deposited in silica aerogel. The cluster spectra were compared to a Ag film reference.

The clusters were produced in a supersonic nozzle expansion ($1.5 \cdot 10^3$ $ms^{-1}$) using THECLA, a Thermal CLuster Apparatus [5, 6, 7]. After this the clusters were embedded in silica aerogel, a highly porous network (up to 99% empty space) of $SiO_2$. Embedding clusters in the interparticle space between the $SiO_2$ particles prevents them from coalescence so that a higher amount of clusters could be deposited. A high amount of deposited clusters enables a good signal to noise ratio in XANES measurements of the Ag $L_3$ edges.

Additionally the nano porous structure of the silica aerogel enables multiple collisions of clusters with the $SiO_2$ particles at the deposition so that they can lower their energy step by step. This soft-landing saves the nearly spherical cluster from deformation.

In Figure 1 the results of our XANES measurements on the Ag $L_3$ absorption edge of Ag clusters in silica aerogel are shown.

One cluster monolayer (ML) corresponds to a hexagonally closed packed layer of clusters and has an effective height of

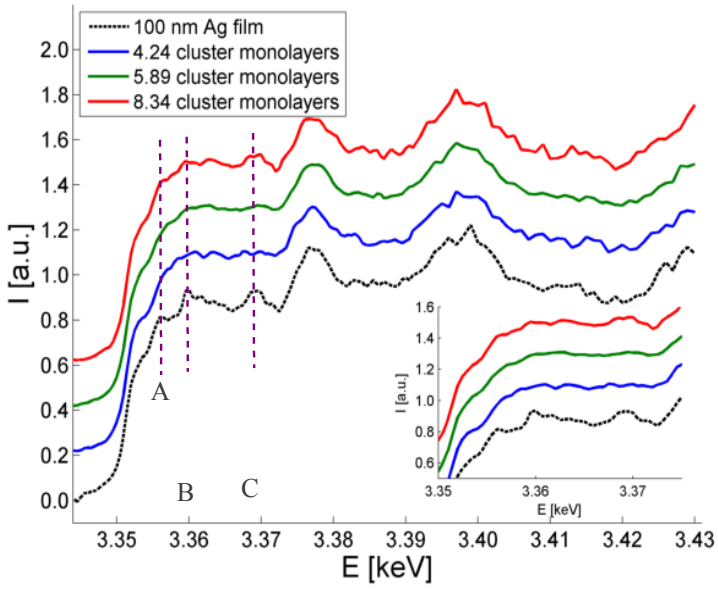


**Figure 1: XANES signal of the Ag $L_3$ edge of Ag clusters deposited with different coverage densities in silica aerogel.**

about $h_{eff}$=1.21R≈1.2nm [8] ($h_{eff}=V_{cluster}/A_{cluster}$ , where $V_{cluster}$ is the volume of a spherical cluster and $A_{cluster}$ the surface per cluster in a hexagonally closed packing) .
There are similarities between the XANES measurements of the deposited clusters and the Ag reference film which is due to coalescence of the clusters to bigger particles. Especially the red line which shows the signal corresponding to the largest coverage density looks quite similar to the signal of the reference film (black dashed line).
But differences between the blue curve (4.24 cluster ML) or the green curve (5.89 cluster ML) and the dashed black curve (reference film) lead to the assumption that there is still no dominant bulk like structure up to coverages of 5.89ML. This is indicated with the three perpendicular lines labelled A,B and C.
There are no visible shifts of the onset of the absorption edges. The adsorption of atoms or molecules with overlapping orbitals would change the uDOS. This would exhibit a different shape, e.g. a “white line”, in the onset of the Ag adsorption edge. This indicates that the oxidation state is close to bulk silver [9].

On these results we started experiments in which we deposited Ag clusters in cleaved silica aerogel. For cleaved aerogel damages of the aerogel surface can be mostly excluded. These samples will be investigated during a XANES beamtime in November 2012 at the ESRF. We expect a beginning of coalescence for even higher coverage densities.

The authors would like to acknowledge the BL8 crew and the DELTA machine group for providing synchrotron radiation and technical support. We thank for the help of D. Müller and E. Kirstein during the experiments.

[1] R.E. Palmer, S. Pratontep, and H.-G. Boyen, Nature Materials **2**, 443 (2003).
[2] Z.Y. Li, N.P. Young, M. Di Vece, S. Palomba, R.E. Palmer, A.L. Bleloch, B.C. Curley, R.L. Johnston, J. Jiang, and J. Yuan, Nature **451**, 46 (2008).
[3] S. Duffe, N. Grönhagen, L. Patryarcha, B. Sieben, C. Yin, B. von Issendorff, M. Moseler, H. Hövel, Nature Nanotechnol. **5**, 335 (2010).
[4] see: Journal of Non-Crystalline Solids, Vol. **145**, (1991).
[5] U. Kreibig, M. Gartz, A. Hilger, and Heinz Hövel, *In: Advances in Metal and Semiconductor Clusters* Vol. **4**, (ed. M.A. Duncan), JAI press Inc., 345 (1998).
[6] O. F. Hagena, Z. Phys. D **20**, 425 (1991)
[7] H. Hövel, S. Fritz, A. Hilger, M. Vollmer, and U. Kreibig, Phys. Rev. B **48**, 18178 (1993)
[8] H. Hövel, A. Hilger, I. Nusch and U. Kreibig, Z. Phys. D **42**, 403 (1997)
[9] P. Behrens, S. Aßmann, U. Bilow, C. Linke and M. Jansen, Z. anorg. allg. Chem. **625**, (1999)

**Investigation of polydisperse Ni/Ti nanoparticles using X-ray Standing Waves**

M. Brücher[1], A. von Bohlen[1], M.Chakif[2], E.Gurevich[2], R. Hergenröder[1]

[1]Leibniz-Institut für Analytische Wissenschaften – ISAS – e.V., Bunsen-Kirchhoff-Str. 11, 44139 Dortmund

[2]Ruhr-University Bochum, Department of Applied Laser Technologies , Universitätsstr. 150, 44801 Bochum

For Ni/Ti nanoparticles, interesting size-dependent ferromagnetic properties are supposed, which should be investigated using X-ray Standing Waves. In a first step, the size distribution of polydisperse particles was characterized.

Polydisperse Ni/Ti nanoparticles from an acetone suspension were pipetted on Si wafers. For the measurement of the size distribution, an X-ray Standing Waves field was generated using hard X-rays (E = 15.5 keV) under grazing incidence. Reflection and interference of the incoming rediation generates the XSW field, which excites the fluorescence of the particles. Variation of the incident angle induces a vertical movement of the intensity maxima. For diameters up to ca. 100 nm, each particle size corresponds to a spacific angular distribution of fluorescence intensity. A silicon drift detector detector mounted perpendicular to the surface collects the fluorescence photons emitted by all irradiated particles.

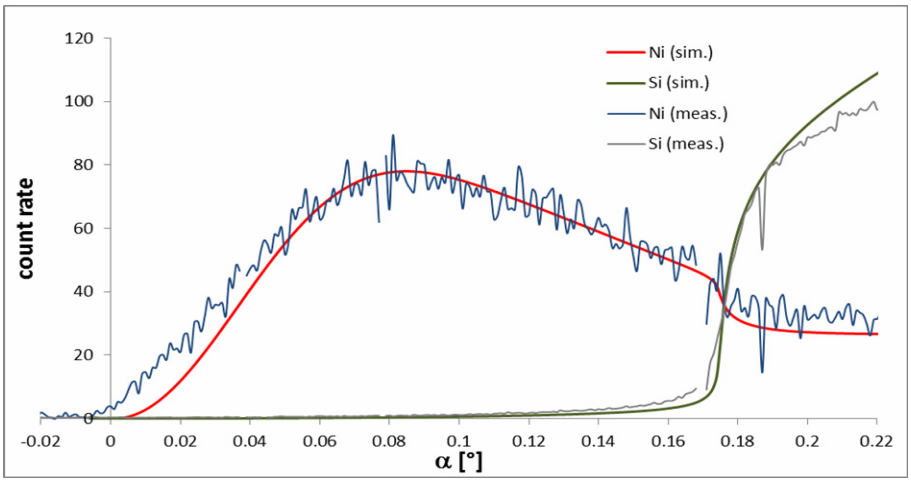


**Fig.1:** Fluorescence signal of Ni/Ti nanoparticles on a Si substrate excited by a 15.5 keV XSW field.

For the evaluation of the measured intensity curves, the XSW-excited fluorescence signals of speres of different diameters (in the range of 5 to 60 nm) was calculated. From these curves, a sum signal

$I_{total}(\alpha)$ was calculated and fitted to the measured data:

$$I_{total}(\alpha) = a \cdot I_{5\,nm}(\alpha) + b \cdot I_{10\,nm}(\alpha) + \ldots$$

The values for the factors a,b,… leading to the optimal fit of the simulated sum signal give the fraction of particles of the respective diameter in the analyzed sample. In total, the composition of 12

particle mixtures was analyzed, the maximum of the size distribution was found at 20 nm diameter. The experiments were performed at beamline 8, using radiation of 10 and 15.5 keV. The fluorescence photons were collected by an Amptek X100-SDD detector.

In a next step, the distribution of diameters should be measured before and after theexposure to a magnetic field in order to identify and characterize a possible size-dependence of ferromagnetic particle properties.

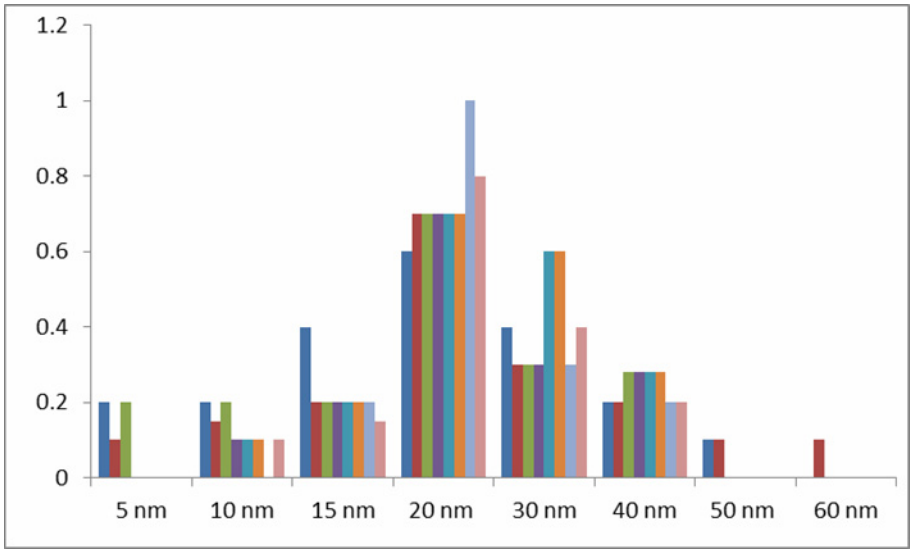


**Fig.2:** Distribution of diameters measured in 7 different particle mixtures.

# XANES investigation of $TiO_2$-$ZrO_2$ composite materials

Stefanie Pfleiderer, Dirk Lützenkirchen-Hecht, Ronald Frahm

Fachbereich C – Physik, Bergische Universität Wuppertal, Gauß-Straße 20, 42097 Wuppertal

Titanium dioxide nanostructures are very interesting for a large number of applications like catalysis, Li-ion batteries, sensor techniques etc. For many of these applications, the structural characteristics of the material are very important for the effectiveness of the materials. For some applications, like catalysts and Li-ion batteries, anatase is the desired polymorph, while other possible phases like brookite or rutile are unwanted. Next to this, small particle sizes and a high degree of crystallinity are required in many catalytic applications [1]. To prepare materials with tailored characteristics, the sol-gel method is very popular. Nevertheless, it is difficult to combine and control different desired materials characteristics. For example, the nanostructures derived in sol-gel processes are usually amorphous without further attendances by calcination or hydrothermal treatment. For any heat treatment, extended calcination times or high temperatures are required to get materials with a high degree of crystallinity. However, using such a treatment also the crystallite size increases, usually up to values higher than the required / desired ones. Due to the growth of the crystallites, there is an additional, often undesired decrease in the specific surface area. An additional disadvantage is that the particle size of nanostructures is an important parameter for the stability of crystalline polymorphs. In case of $TiO_2$, anatase to rutile phase transformations become more probable with increasing crystallite size. Thus, it is desirable to have a possibility to stabilize especially the particle size during the calcination treatment. There is indeed a known possibility to achieve this stabilization. The addition of other metal oxides, like $SiO_2$, $MoO_3$ or $ZrO_2$, stabilizes the crystallite size and increases the temperature of the anatase to rutile phase transition [2].

In our work, $TiO_2$-$ZrO_2$ composite nanopowders are prepared next to pure $TiO_2$ powders to investigate the influences of the $ZrO_2$ addition and the chemical reaction parameters on the materials structure. We prepared samples with different $TiO_2$:$ZrO_2$ ratios between 1:2 and 25:1 and pure $TiO_2$ and $ZrO_2$ powders for comparison. The samples are investigated by linear combination fits of the XANES region in the x-ray absorption spectrum (XAS) [3]. For a calcination temperature of T=500°C applied for four hours, a powder with an oxide ratio of $TiO_2$:$ZrO_2$=4:1 was the first in which a small amount of anatase has been build. The amount of anatase increases with decreasing zirconia concentration in the samples. The zirconium fractions in the samples remained amorphous for all oxide ratios. A $TiO_2$:$ZrO_2$ ratio of 20:1 was found to be able to stabilize the crystallite size and allows large amounts of the samples to crystallize.

The influence of the chemical preparation parameters has been investigated by the synthesis and characterization of pure $TiO_2$ and composite sample with $TiO_2$:$ZrO_2$=20:1 with Alkoxide:$H_2O$ ratios of 1:2, 1:4 and 1:20, dilution of alkoxides in 5, 15 and 25 ml n-propanol and by preparation of samples in 1 M hydrochloric acid (HCl), 1 M sodium hydroxide (NaOH) and 1 M potassium hydroxide (KOH). In all composite samples, the crystallite size stays nearly constant with increasing annealing temperature. The determination of the development of the anatase concentration in the samples with increasing calcination temperature does not lead to a general trend in dependence on the chemical reaction parameters. To get qualitative information of the development of the $TiO_2$ cluster size in dependence on the chemical reaction parameters, the pre-edge regions of the XANES spectra are deconvoluted with Gaussian peak profiles. In Fig. 1 a), the XANES spectra of three pure $TiO_2$ samples prepared with TTIP:HCl=1:2, 1:4 and 1:8 are presented. The powders have not been heat treated before the measurements. As can be seen, the shape of the XANES changes

with increasing HCl amount. In comparison with the reference spectra presented in part b), it can be seen that the XANES edge shape look more like the anatase reference for a high HCl amount. The deconvolution of the XANES spectrum of the sample with TTIP:HCl=1:8 is presented in part c). An important point in the deconvolution of the pre-edge region is the intensity ratio of the A3 and the A2 peak (comp. part a)). In the literature, the A2 peak is assigned to the absorption of five-fold coordinated Ti absorbers, while the A3 peak is assigned to six-fold coordinated Ti absorbers. The size of the clusters determine the intensity ratios because in the particle bulk, the absorbers are six-fold coordinated while the coordination is reduced at the particle surface, which increases relative to the bulk for decreasing particle size. Indeed, an increase in the A3:A2 peak intensity ratio is observed for the three presented samples with increasing amount of added HCl.

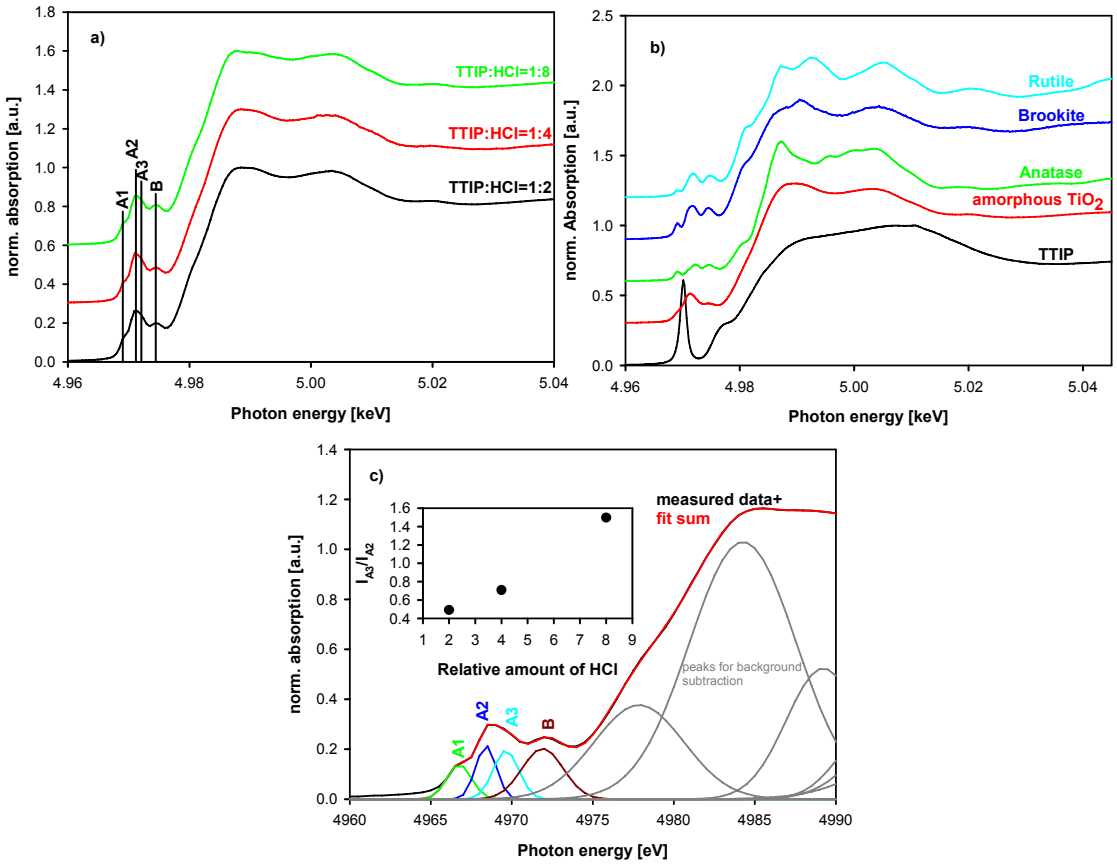


**Fig. 1** XANES spectra of pure TiO2 samples prepared with different amounts of added 1 M HCl solution in part a). Part b) presents reference spectra of TiO2 polymorphs, amorphous TiO2 and the TTIP precursor. An example of a pre-edge deconvolution and the peak intensity ratio in dependence of the amount of added HCl (embedded graph) are shown in part c).

## References


[1] R. Rossmanith, C. K. Weiss, J. Geserick, N. Hüsing, U. Hörmann, U. Kaiser, K. Landfester, Chem. Mater. 20, 5768-5780, 2008.

[2] K. Maver, U. Lavrenčič Štangar, U. Černigoj, S. Gross, R. Cerc Korošec, Photochem. Photobiol. Sci., 8, 657-662, 2009.

[3] S. Pfleiderer, D. Lützenkirchen-Hecht, R. Frahm, J. Sol-Gel Sci. Technol., 64, 27-35, 2012.

# 5 years of Education with Synchrotron Radiation at DELTA – a short review of past activities and a look into the future

Dirk Lützenkirchen-Hecht & Ronald Frahm
Fachbereich C – Physik, Bergische Universität Wuppertal

Since the time that the Materials Science Beamline BL8 [1] was inaugurated in 2007, several students from Wuppertal were taught in different kinds of experiments with synchrotron radiation using especially the hard X-rays provided by the superconducting Wiggler at DELTA, including radiation protection issues also. The local access of students to a large scale accelerator facility is unique, and the practical training and education at DELTA is integrated in the curriculum of the physics bachelor and master courses in Wuppertal. Here we want to review some of the past activities, and give an outlook into the future.

As important examples to be mentioned, some of the first X-ray standing wave experiments at BL8 were performed with a student from Wuppertal University [2] as a practical exercise. In Fig. 1, an exemplary result of these measurements is presented. The sample was a sulphur-doped polymer on a Si wafer for a potential use as organic light emitting diodes, and the measurements were performed in order to trace the Sulfur distribution within the polymer. For this purpose, the Si and S X-ray fluorescence of the sample (see inset of Fig. 1) is measured as a function of the incidence angle for a fixed photon energy (10 keV in the present case). A detailed fit of the measured data then provides the sulphur distribution within the polymer film.

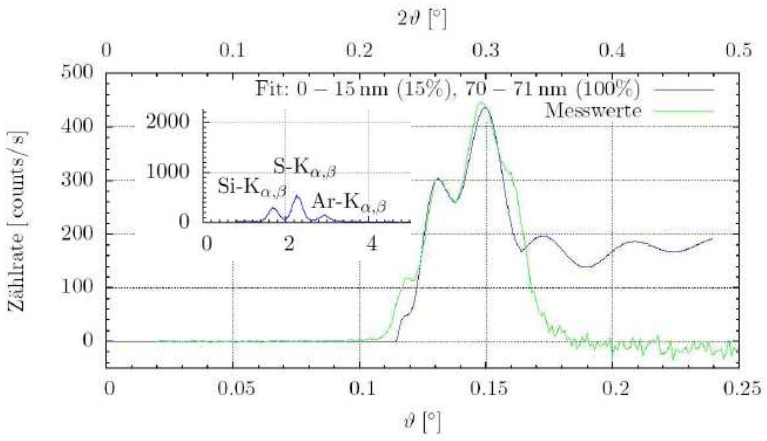


**Fig. 1:** XSW experiment of a sulphur-containing polymer film on a silicon substrate. The standing wave field is excited by 10 keV X-rays, and the angular dependence of the Si and S $K_\alpha$ radiation is measured using a Si pin-diode as shown in the inset. The fit of the data to a model consisting of a 15 nm top layer with a S concentration of 15% and an additional buried 1 nm thick pure sulphur layer in a depth of 70 nm is also shown.

In order to verify the feasibility of surface sensitive EXAFS investigations of liquids, another important practical exercise was performed by students of Wuppertal university. The basic idea was to use the upper mirror element of the double mirror device which is originally designed for the harmonic rejection of low energy beams [1] to deflect the incidence beam on the horizontally aligned liquid sample. These mirrors are located in the experimental hutch about 1 m upstream of the diffractometer. However, the beam is usually reflected upwards on the first mirror of this device during conventional operation, and the apertures of the Be-window which separates the beamline vacuum against the laboratory air, the vacuum valve and all the other beamline components downstream the mirrors are designed for such an optical path (see Fig. 2). Therefore the students have evaluated the accessible angular range and the intensities at the sample position for different energies, and also investigated model samples in both the conventional Θ-2Θ geometry without using the double mirror device, and using the newly proposed Θ-Θ-geometry. [3]. Furthermore, it must be kept in mind that a

change of the incidence angle Θ always requires a height adjustment of the sample – and the students have also verified the possibilities of an automatic correction and alignment of the sample in the beam. It should be mentioned here that successful EXAFS experiments on Langmuir films have been conducted in the meantime [4, 5].

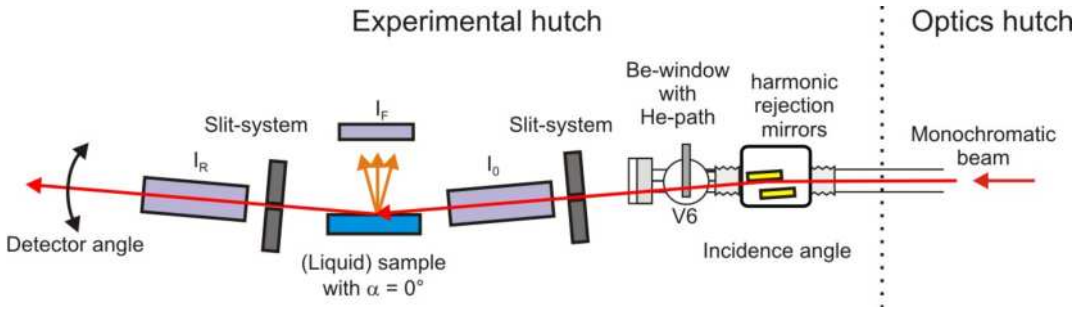


**Fig. 2:** Setup for the X-ray reflectivity experiments of liquid sample surfaces at BL8 in a Θ-Θ-geometry. The monochromatic beam from the Si(111) double crystal monochromator is reflected downwards by the upper mirror of the double mirror device. The incidence angle on the sample is limited to about 0.3° (5 mrad) by the maximum negative tilt angle of the mirror system and the apertures of the beamline equipment downstream the double mirror device.

Materials Science is one of the main research objectives in the Condensed Matter Physics department of Wuppertal University, and thus, several related studies have been conducted by students at BL8. As examples, the X-ray analysis of oils used for lubrication in vehicle engines and the preparation of complex materials for a use as electrode material in Li-ion batteries should briefly be considered here.

Modern motor oils are actually an extremely good example for a high-tech product. More than 20% of the oil are additives for different puposes: Dispersants (ca. 5%) bind contaminations, detergents (ca. 2-3%) prevent deposits on the metal surfaces inside the motor, anti-wear agents (ca. 1%) form a protective coating on metal surfaces, friction modifiers (ca. 1%) reduce friction under high temperatures and high load conditions, antioxidants and anti-foam additives help to slow the oxidation of the oil and the formation of air-bubbles in the oil, rust and corrosion inhibitors protect the metals, and viscosity additives (up to 10%) improve the viscosity index of the oil, so that the oil base amounts to only about 78% of the lubricant. The original goal of this project was to prove the presence of abraised metals from the motor in the oil by means of X-ray fluorescence and to identify the binding state of those metals by X-ray absorption spectroscopy. However, the most prominent peaks in XRF of the fresh (unused) and the waste (used) oil were those of Zn, and only small amounts of Fe was detectable in the waste oil [6]. The strong Zn peaks could be explained by the presence of Zn-diethyl-dithio-phosphate (Zn-DDTP), a compound that is frequently used in oils as anti-wear reagent and friction modifier, and accordingly, weak signals of sulphur were also detected in the XRF [6].

In Fig. 3, the Fourier-transformed EXAFS signals of some selected fresh and waste oil samples are compared to the FT of ZnO and a pure Zn-DDTP reference. As can be seen, the Zn-S coordination of the fresh oil and the Zn-DDTP reference agree quite well in intensity and peak position, and thus, this additive can be clearly identified. In contrast, the peak position of the first detectable peak in the FT of the used oil significantly shifts to lower energies, and the peak could not be fitted with an Zn-S coordination – the resulting bond distance is much too small. However, compared to the FT of crystalline ZnO, the peak intensity and bond distance fit well, suggesting that the Zn-DDTP complex is oxidized to ZnO during the life of the oil. Accordingly, the wear and friction reducing properties of the oil decrease during its use in the motor, and an oil exchange is mandatory.

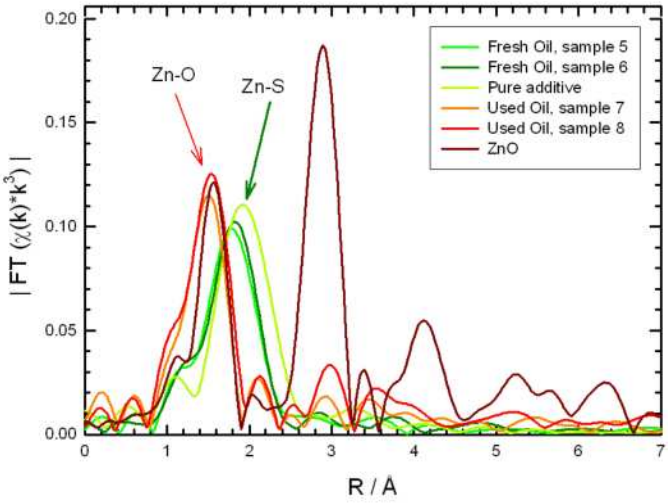


**Fig. 3:** Results of the Zn K-edge EXAFS experiments of some fresh oil samples, waste oil and reference compounds ZnO and the pure additive. Obviously, the Zn-S bond breaks during the use of the oil, and some oxidation towards ZnO occurs [6].

$LiFePO_4$ olivine is an interesting material for a use as cathode material in rechargeable Li-ion batteries [7], and thus many efforts have been spent on the preparation of high capacity materials with a good cyclability. Here the olivine was synthesized by means of a sol-gel technique: Lithium hydroxide monohydrate ($LiOH*H_2O$) was mixed with iron oxalate dihydrate ($FeC_2O_4 * 2H_2O$) in nitric acid ($HNO_3$). Dropwise addition of ammonium di-hydrogen phosphate ($(NH_4)H_2PO_4$) and citric acid ($C_6H_8O_7$) leads to the final solution, which was slowly heated to about 75°C, to remove the excess water and form the gel within about 60-90 minutes. A first calcination occurs at 100°C in a simple furnace in air for 2-5 h, while a second heat treatment at 750-850°C for 10 h was performed in a clean Ar atmosphere in order to prevent any Fe-oxide formation [8]. EXAFS and X-ray diffraction analysis of samples prepared in different gaseous environment during the calcinations show the necessity of a clean noble gas atmosphere during the second heat treatment [8]. In Fig. 4, the Fe K-edge EXAFS fit results of a properly treated $LiFePO_4$ sample are presented in R- and k-space representation. The fit was performed on an ab-initio basis using calculated phases and amplitude functions using the first 9 coordination shells, i.e. 6 Fe-O bonds in a radial distance from 2.05-2.45 Å, 5 Fe-P coordinations between 2.87 and 3.8 Å, and a single Fe-Fe bond at 3.87 Å. The structural parameters derived this way agree quantitatively with literature values.

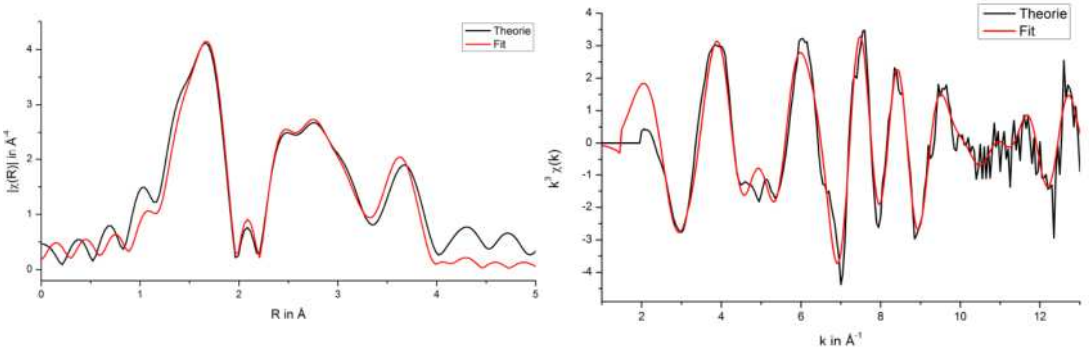


**Fig. 4:** Fit results of the Fe K-edge EXAFS experiments of a sol-gel derived $LiFePO_4$ sample. The fit was performed on an ab-initio basis using calculated phases and amplitudes for the first 9 coordination shells [8].

Closely related to the analysis of functional materials, new X-ray-related techniques and their experimental possibilities are investigated in the Experimental Condensed Matter Physics department. Here, especially the equipment for fast time resolved X-ray absorption experiments is considered: If an absorption spectrum with typically more than 1000 data

points is measured within some milliseconds only, the time for an individual absorption measurement is in the order of some microseconds only, and thus the X-ray detectors must be fast enough (see e.g. [9]). For conventional transmission mode EXAFS studies, parallel plate ionization chambers are used. However, as can be seen in Fig. 5, the step response function of such a detector is typically in the order of several hundred µs: Both the electrons and the created ions contribute to the current signal, and because of the slow ions with their low drift velocities, the response function is strongly stretched in time [10]. Using a gridded ionization chamber with the additional grid powered at a sufficiently negative potential of about -300 V, the ions might be hindered in reaching the counter electrode of the ionization chamber. The current response thus depends only to the fast electrons, and the result is a significantly improved response time of about 5.5 µs only as can be seen in Fig. 6. Recent improvements of the used current amplifier electronics have further reduced the rise time of the entire detection chain to less than 1 µs [11, 12].

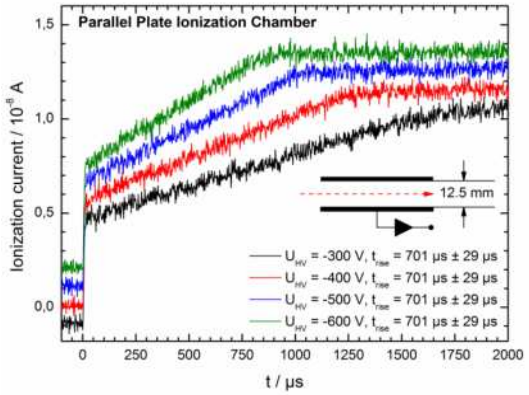


**Fig. 5**: Step response of the parallel plate ionization chamber measured with different applied voltages. The curves are shifted vertically for better visualization.

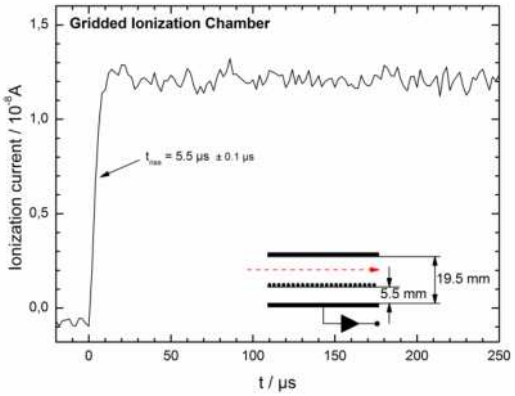


**Fig. 6**: Step response of the gridded ionization chamber.

In conclusion, the first five years of practical education with Synchrotron Radiation at DELTA have shown that meaningful research can be performed with students, and that this type of doing research at a large-scale facility like DELTA is also well accepted and appreciated by the students.

We gratefully acknowledge the DELTA machine group for providing the excellent working condition at the storage ring, and the manifold technical support of our work!

**References**

[1] D. Lützenkirchen-Hecht, R. Wagner, U. Haake, et al., J. Synchrotron Rad. 16 (2009) 264
[2] H. Wilhelm, Oberflächenstrukturuntersuchung mit stehenden Röntgenwellen. Universität Wuppertal (2008)
[3] D. Lützenkirchen-Hecht, T. Heim, S. Rutkowski, R. Wagner, R. Frahm. DELTA annual report (2009) 14
[4] S. Bieder, Diploma Thesis TU Dortmund (2010)
[5] D. Lützenkirchen-Hecht, R. Wagner, S. Bieder, R. Frahm, J. Phys.: Conf. Proc. (2012), in print.
[6] L. Müller. Bachelor Thesis, Universität Wuppertal (2011)
[7] A. K. Padhi, K. S. Nanjundaswamy, J. B. Goodenough, J. Electrochem. Soc.144 (1997) 1188
[8] L. Hoffmann. Bachelor Thesis, Universität Wuppertal (2011)
[9] J. Stötzel, D. Lützenkirchen-Hecht, R. Frahm, J. Synchrotron Rad. 18 (2011) 165
[10] O. Müller, Diploma Thesis, Universität Wuppertal (2010)
[11] P. Becker, Bachelor Thesis, Universität Wuppertal (2012)
[12] O. von Polheim, Bachelor Thesis, Universität Wuppertal (2012)

# Notes

# Notes